Super-enantiospecific Autocatalytic Decomposition of Tartaric Acid and Aspartic Acid on Cu Surfaces

Submitted in partial fulfillment of the requirements for

the degree of

Doctor of Philosophy

in

Chemical Engineering

Bharat Suresh Mhatre

B.E., Chemical Engineering, University of Mumbai, India

Carnegie Mellon University
Pittsburgh, PA

April, 2013

..... to my parents, Sudha and Suresh Mhatre

Acknowledgements

I take this opportunity to express my sincere appreciation to all those who have contributed to this thesis and supported me in one way or the other along this long but fulfilling journey. It has been a great pleasure to spend several years in the Department of Chemical Engineering at Carnegie Mellon University, and its members will always remain dear to me.

First and foremost, I would like to express my gratitude to my advisor Prof. Andrew Gellman for his unyielding support and guidance, educational and otherwise, over the course of my doctorate degree. I feel privileged to have been able to work with him.

I would like to thank my thesis committee members including Prof. James Miller, Prof. Paul Sides and Prof. Lisa Porter for their time, insight and directions.

Very special thanks to Janet Latini, Cindy Vicker, Toni McIltrot, Julie Tilton, Justin Dawber, Larry Hayhurst and Shannon Young for all their help and cooperation from time to time.

My sincere gratitude goes to all members of the Gellman research group. I would specially like to thank Xu Feng for his patience and guidance during my early days in the group. Dr. Peter Kondratyuk and Dr. Esteban Broitman were always available with their experience and knowledge to provide assistance time and again, in fixing various issues with my experimental setup and design. Special thanks to Dr. William Michalak and Dr. Deepika Priyadarshani for their help on several occasions. I have used models developed Dr. Brian Holsclaw for fitting some of my experimental data. I have also used some data from Dr. Vladimir

Pushkarev's dissertation in this thesis. Yongju Yun and I worked on closely related projects and it was wonderful to have him around for exchanging notes and discussing different ideas.

I would not have contemplated this journey had it not been for the love and encouragement of my family and friends in India. I cannot find words to express my gratitude to my parents, Sudha and Suresh, to whom I dedicate this thesis. Loving thanks to my brother, Nihar, who truly encouraged me to pursue graduate studies, and to my cousins, Kanchan and Dinesh, for their unconditional support all my life. I would also like to express my appreciation to my parents-in-law, Prita and Gokulakrishnan, for always having taken a keen interest in my work and keeping me in their prayers. Ultimately, I would like to acknowledge the most special person in my life – my wife, Sneha for her personal support, sacrifice and patience at all times.

This work has been supported by the US Department of Energy (grant no. DE-FG02-12ER16330) and National Science Foundation (grant no. CHE-1012358).

Abstract

Autocatalytic reaction mechanisms are observed in a range of important chemical processes including catalysis, radical-mediated explosions, and biosynthesis. Because of their complexity, the microscopic details of autocatalytic reaction mechanisms have been difficult to study on surfaces and heterogeneous catalysts. Autocatalytic decomposition reactions of tartaric acid (TA) enantiomers adsorbed on Cu(110) offer molecular-level insight into these processes, which until now, were largely a matter of speculation. The decomposition of TA/Cu(110) is initiated by a slow, irreversible process that forms vacancies in the adsorbed TA layer, followed by a vacancy-mediated, explosive decomposition process that yields CO_2 and small hydrocarbon products. Initiation of the explosive decomposition of TA/Cu(110) was studied by measurement of the reaction kinetics, time-resolved low energy electron diffraction (LEED), and time-resolved scanning tunneling microscopy (STM). Initiation results in a decrease in the local coverage of TA and a concomitant increase in the areal vacancy concentration. Once the vacancy concentration reaches a critical value, the explosive, autocatalytic decomposition step dominates the subsequent TA decomposition rate.

Aspartic acid is an excellent probe molecule for investigating the surface chemistry of autocatalytic reactions . Because a wide range of isotopically labeled varieties of aspartic acid are commercially available, we have been able to conduct a detailed investigation of its autocatalytic reaction mechanism. Experimental data obtained for variable initial coverage, variable heating rate and

isothermal TPRS experiments, while monitoring CO_2 desorption is in excellent agreement with a rate law which explicitly accounts for an initiation step and an explosion step which is second order in vacancy concentration.

Autocatalytic surface explosion mechanisms can be exploited to attain extremely high enantiospecificities in the case of TA decomposition on naturally chiral Cu(hkl)$^{R\&S}$ surfaces. Interaction energies of chiral molecules with naturally chiral surfaces are small and typically lead to modest enantioselectivities. However, the highly non-linear kinetics of autocatalytic reaction mechanism amplifies these small differences to result in high enantiospecificities. The observed phenomenon has the characteristics of autocatalytic processes that have been postulated to lead to biomolecular homochirality in life on Earth; processes with relatively small differences in reaction energetics that, nonetheless, lead to extremely high enantioselectivity.

Table of Contents

List of Tables

List of Figures

acids with a D-glyceraldehyde molecule, the –(COH) group corresponds to the –(NH_2), –(CH_2OH) group corresponds to –(COOH) and –(OH) group corresponds to the side chain. Thus for L-alanine, when –(NH_2) group points upwards with –(COOH) group facing away from you, the –(CH_3) group is on your left (from the Latin word *laevus* meaning left) and for D-alanine the –(CH_3) group will be on your left.

Figure 1.5 The CIP nomenclature identifies the handedness of chiral carbon atoms as S- or R-, based on the priority and arrangement of the four substituent groups around the chiral center. If the molecule is oriented such that the ligand with lowest priority i.e. 4 is pointed away from the viewer and if the ligand 1 to 3 are ordered such that the movement from ligand 1 to 3 passing through 2 (i.e. sequence 1→2→ 3) is in the clockwise direction the chiral center is designated as R. Vice versa if the ligands 1 to 3 are ordered such that the movement from ligand 1 to 3 passing through 2 (i.e. sequence 1→2→ 3) is in anti-clockwise direction the configuration movement in the anti-clockwise direction the chiral center is designated as S. **10**

Figure 1.6 R- and S- enantiomers of thalidomide. While R-thalidomide functions in a therapeutic manner, its counterpart S-thalidomide act as a teratogen and resulting in birth defects in babies. Appreciation of differences in the manner in which these two enantiomers of thalidomide react with the human body could have averted the most disastrous medical tragedies of all times – 'the thalidomide tragedy'. **13**

Figure 1.7 Asymmetric hydrogenation of a) methyl acetoacetate on Ni templated with tartaric acid and b) methyl pyruvate on cinchonidine are the most widely studied examples of enantioselective reactions catalyzed by chirally templated surfaces. **17**

Figure 1.8 Crystals of quartz having opposite handedness. The figure illustrates the left- and right-handed crystal forms of natural quartz. Quartz has an inherently chiral bulk crystalline structure formed by helical arrangement of corner-sharing SiO4 tetrahedra. Every crystallographic face exposed by quartz is intrinscically chiral and chiral surfaces can be obtained by exposing surfaces of such naturally chiral bulk crystalline solids like quartz. The chirality of the exposed surface is dictated by the chirality of the bulk. **18**

Kinks are the features on the surface that impart it with its characteristic chirality. The direction from the most close-packed (111) plane to the (100) plane to the least close-packed (110) plane dictates the handedness of the surface: counterclockwise rotation is denoted as S and clockwise rotation is denoted as R.

Figure 5.2 TPD spectra of R-3-MCHO on Cu(643)$^{R\&S}$ shows three characteristic peaks at 225 K, 340 K and 385 K, corresponding to the desorption of R-3-MCHO from terraces, steps and kinks, respectively. The inset shows R-3-MCHO desorption from the kinks on Cu(643)$^{R\&S}$ surfaces. The enantiospecific difference in the peak desorption temperature from the kinks on these two surfaces is ΔT_p = 3.5 ± 0.8 K. The resolution factor between the two spectra is $RF^{RS} = \Delta T_p^{RS}/\Delta T_{FWHM} = 0.14$ while the enantiospecificity in the rate at 385 K is $ES_{385\,K}^{RS} = r_R^D/r_S^D = 1.08$. **151**

Figure 5.3 TPR spectra of D-TA on the Cu(643)^{R} surface at varying initial coverage of TA on the surface i.e. varying θ_0^{TA}. As the initial coverage increases, the peak decomposition temperature increases and the width of the spectra decreases. At saturation coverage i.e. θ_0^{TA} = 1, the TPR spectra has a peak desorption temperature of T_p = 496 K and a FWHM of only ΔT_{FWHM} = 3.5 K. The spectral shifts and extraordinarily narrow peak at saturation are characteristic indicators of surface explosion. **153**

Figure 5.4 TPR spectra of D-TA on the Cu(643)^{S} surface at varying initial coverage of D-TA on the surface i.e. varying θ_0^{TA}. As the initial coverage increases, the peak decomposition temperature increases and the width of the spectra decreases. At saturation coverage i.e. θ_0^{TA} = 1, the TPR spectra has a peak desorption temperature of T_p = 486 K and a FWHM of only ΔT_{FWHM} = 3.5 K. The spectral shifts and extraordinarily narrow peak at saturation are characteristic indicators of surface explosion. **154**

Figure 5.5 The figure illustrates the TPR spectra of D-TA on Cu(643)$^{R\&S}$ surfaces at saturation coverage, θ_0^{TA} = 1. The two peaks are separated by ΔT_p = 10 K and have a narrow width of ΔT_{FWHM} = 3.5 K. These spectra reveal highly enantiospecific kinetics with a resolution factor of around $RF^{RS} = \Delta T_p^{RS}/\Delta T_{FWHM} = 2.8$ and a rate enantiospecificity of around $ES_{486\,K}^{RS} = r_R^D/r_S^D = 47$. **155**

no observable desorption of CO_2. Slow nucleation of vacancies reduces θ^{TA} until the autocatalytic decomposition begins to dominate and rapid acceleration of the reaction depletes the adsorbed TA. Enantiospecificity is manifested by the dependence of the reaction time, t_p, on the relative chirality of the L-TA and D-TA and the Cu(651)^S surface. TA/Cu(651)^S experiments were performed by Holsclaw and this figure is adopted from his thesis [1].

Figure 5.10 Comparison between the plot of peak times t_p at various isothermal temperatures T_{iso} for D- and L-TA on Cu(651)^S surfaces from experimental data and the t_p estimated by the model fits using the rate expression in eq. 5.1 and parameters i.e. A_i, A_e, ΔE_i and ΔE_e, in the Table 5.1. It is evident that the experimental and the simulated values are in close agreement. The figure directly illustrates the enantiospecific variation between the peak temperature times for D- and L-TA on Cu(651)$^{R\&S}$ as a function of T_{iso}. **168**

Figure 5.11 Plot of $ln(t_p)$ versus T_{iso}^{-1}, where t_p is the peak time corresponding to isothermal temperature T_{iso} and $t_p^{-1} = k_{eff} = \sqrt{k_n k_e}$. The slope yields the effective barriers for D- and L-TA decomposition on Cu(651)^S surface $\Delta E_{eff} = (\Delta E_i + \Delta E_e)/2$, derived from the two rate constants k_i and k_e. The enantiospecific difference between the effective barriers $\Delta\Delta E_{eff} = \Delta E_{eff}^{D/S} - \Delta E_{eff}^{L/S}$ is not significantly different from zero. **169**

Chapter 1

Introduction and Overview

1.1 Molecular Chirality

'Chirality' is a spatial geometric property possessed by an object on account of which it cannot be superposed on its mirror image [3, 4]. Thus, a chiral object or a system differs from its mirror image. A non-chiral object/system can be superposed on its mirror image is called achiral or amphichiral. Human hands are the most commonly recognized examples of chirality as a result of which, chirality is sometimes referred to as 'handedness'. In fact, the term *chirality* is derived from the Greek 'χειρ *(kheir)'* which means hand [5, 6].

In the case of molecules, a pair of chiral molecules are referred to as enantiomers of one another and the branch of chemistry involving the study of enantiomers is called stereochemistry. Two enantiomers have identical atomic composition and atomic connectivity (i.e. bond length and absolute bond angles), however, they differ in the geometric orientation of this atomic connectivity [7]. In the case of organic molecules, more often than not, the presence of an asymmetric carbon atom renders chirality to the molecule [8].

Consider the example of an alanine molecule which is an α-amino acid. It consists of a carboxylic group (-COOH), an amine group (-NH2), a hydrogen atom (-H) and a methyl (-CH3) group tetrahedrally coordinated to the α-carbon atom. With a three dimensional arrangement of four different substituents around the central carbon atom, such an asymmetric molecule is non-superposed on its

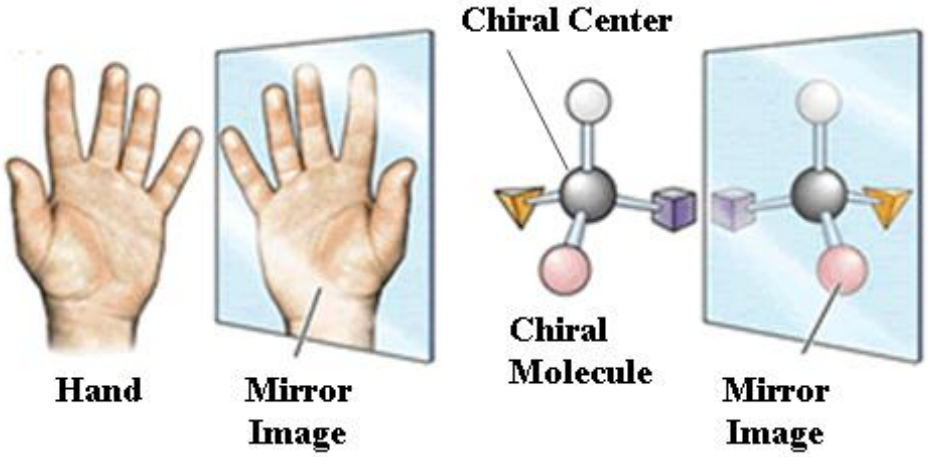

Figure 1.1 Demonstration of chirality in human hands and molecules. (Right) Human hands are the most commonly recognized examples of chirality, as a result of which, chirality is sometimes referred to as 'handedness'. (Left) In the case of molecules, a pair of chiral molecules are referred as enantiomers. Two enantiomers have identical atomic composition and atomic connectivity, however, they differ in the geometric orientation of this atomic connectivity. Typically, a three dimensional arrangement of four different substituents around a central atom, renders chirality to the molecule. Image adopted from http://www.biochemden.in.

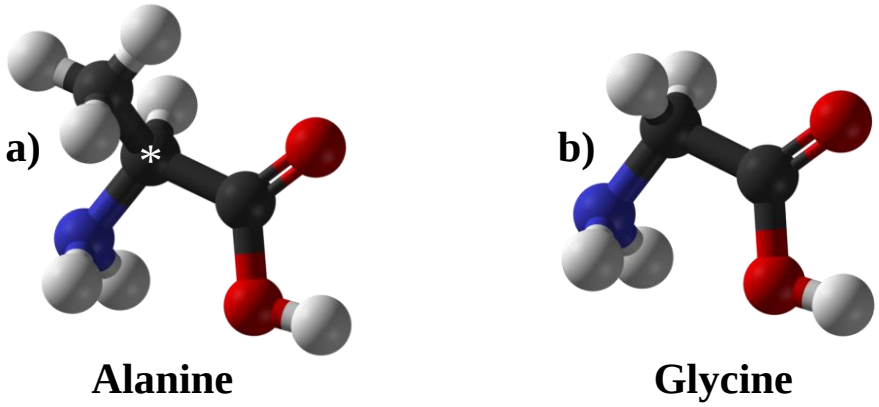

Figure 1.2 Ball and stick models of two α-amino acid molecules – alanine and glycine. a) Alanine consists of a carboxylic group (-COOH), an amine group ($-NH_2$), a hydrogen atom (-H) and a methyl ($-CH_3$) group tetrahedrally coordinated to the α-carbon atom. With a three dimensional arrangement of four different substituents around the central carbon atom, alanine is non-superposed on its mirror image and hence chiral (the molecule in the figure is in fact a representation of L-alanine). The α-carbon atom acts as a chiral center. b) Glycine consists of a carboxylic group (-COOH), an amine group ($-NH_2$), and two hydrogen atoms (-H) tetrahedrally coordinated to the α-carbon atom. With two equivalent substituents around the central carbon atom, glycine can be superposed on its mirror image and hence it is achiral.

mirror image and hence chiral. In fact, all α-amino acids with an exception of glycine are chiral. In glycine the methyl group in alanine is replaced with another hydrogen atom.

Enantiomers have identical physical properties such as melting point, boiling point, vapour pressure etc. and they exhibit identical behavior in achiral environments. However, it is their interaction with chiral environments that is of interest because these enantiospecific interactions somehow led to the evolution of 'homochiral' life on Earth [9, 10]. In stereochemistry, homochirality is a term used to refer to a class of molecules that possess the same sense of chirality and it is a characteristic of life on Earth. Bio-molecules such as sugars, enzymes, amino acids, proteins, and nucleic acids are chiral and only appear in one enantiomeric form in nature [11, 12]. Consequently, the human body acts as a chiral environment and chiral compounds produced for human consumption must be enantiomerically pure.

1.2 Nomenclature

Among several different nomenclature conventions found in the literature on stereochemistry, the three most commonly used systems are based on [13]:

1. Optical activity
2. Analogy with reference to a glyceraldehyde molecule
3. Cahn-Ingold-Prolog (CIP) priority rules

Systems based on actual molecular configuration

1.2.1 Optical activity based nomenclature system

Optical activity is a unique physical property of chiral compounds/enantiomers; they rotate the plane of plane-polarized light and therefore enantiomers are also referred as optical isomers. Quantitatively two enantiomers have identical ability to rotate this plane of polarization, but they rotate it in opposite senses. A compound that rotates the plane of polarization in a clockwise direction is denoted (+)- or *d*- which stands for *dextrorotation* and the compound is called dextrorotatory. Similarly, a compound that rotates the direction in the anti-clockwise direction is denoted (-)- or *l*- which stands for levorotation and the compound is called levorotatory [13].

1.2.2 Fischer-Rosanoff nomenclature system

Currently, nomenclature conventions based on the actual geometric configuration of each enantiomer are more commonly used. The Fischer-Rosanoff nomenclature system is one such system in which the dextrorotary glyceraldehyde i.e. (+)-glyceraldehyde molecule is considered a reference standard, and enantiomers of other molecules are named based on the orientation of atomic groups with reference to those on (+)-glyceraldehyde [13].

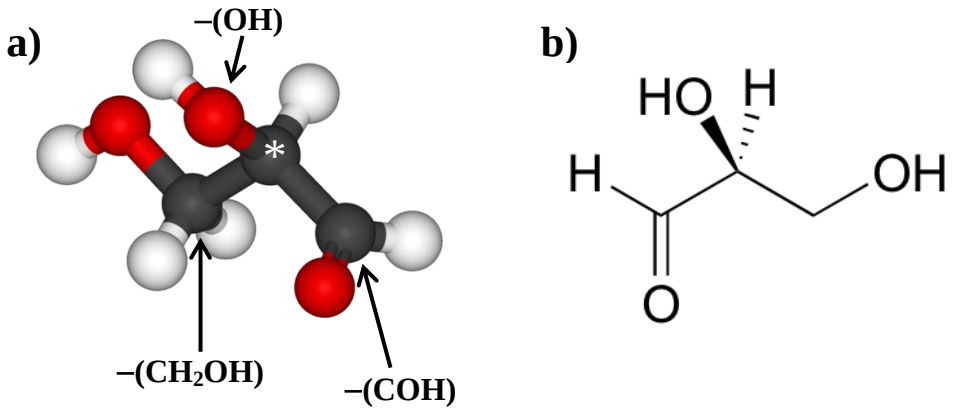

Figure 1.3 a) Ball and stick model and b) skeletal sketch, of a D-glyceraldehyde molecule. This enantiomer of glyceraldehyde is used as a reference standard in the Fischer-Rosanoff nomenclature system, in which, enantiomers of other molecules are named based on the orientation of atomic groups with reference to those on a D-glyceraldehyde molecule. The compounds which can be correlated without inverting the chiral center are named D- and those which can only be correlated by inverting the chiral center are named L-. When a glyceraldehyde molecule is oriented such that –(COH) points upwards with the –(CH_2OH) group facing away from you and if the –(OH) group will lies on your right side, the enantiomer is D-glyceraldehyde (Representation 'D-' stems from the Latin word *dexter* meaning right).

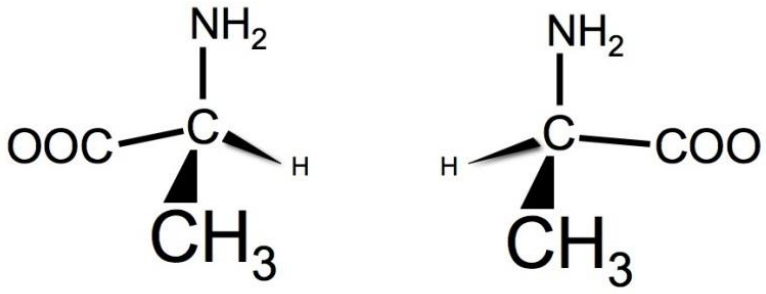

L-alanine **D-alanine**

Figure 1.4 Enantiomers of alanine, L-alanine and D-alanine. Following the Fischer-Rosanoff nomenclature system, while correlating α-amino acids with a D-glyceraldehyde molecule, the –(COH) group corresponds to the –(NH_2), –(CH_2OH) group corresponds to –(COOH) and –(OH) group corresponds to the side chain. Thus for L-alanine, when –(NH_2) group points upwards with –(COOH) group facing away from you, the –(CH_3) group is on your left (from the Latin word *laevus* meaning left) and for D-alanine the –(CH_3) group will be on your left.

The compounds which can be correlated without inverting the chiral center are named D- and those which can only be correlated by inverting the chiral center are named L-. If a D-glyceraldehyde molecule is oriented such that –(COH) points upwards with the –(CH_2OH) group facing away from you, the –(OH) group will be on your right side (from the Latin word *dexter* meaning right). While extending this analogy to amino acids, the –(COH) group corresponds to the –(NH_2),the –(CH_2OH) group corresponds to –(COOH) and the –(OH) group corresponds to the side chain. Thus for L-alanine, when –(NH_2) group points upwards with –(COOH) group facing away from you, the –(CH_3) group is on your left (from the Latin word *laevus* meaning left).

This nomenclature system can easily be confused with d- / l- optical activity based system and is therefore strongly discouraged by the IUPAC. For example, D-fructose as per D-/L- nomenclature system is also referred to as levulose, because, as per optical activity based nomenclature it is a levorotatory compound i.e. l-fructose.

1.2.3 Cahn-Ingold-Prelog (CIP) nomenclature system

The Cahn-Ingold-Prelog (CIP) nomenclature system, which is also based on molecular configuration of an enantiomer, is an absolute system since it does not depend on any reference molecule such as glyceraldehyde [13, 14]. The four ligands or substituent groups around the chiral center are assigned numbers from 1 to 4 in the order of decreasing priority, according to the Cahn-Ingold-Prelog (CIP) priority rules which are typically based on atomic numbers [14]. Now if the molecule is oriented such that the ligand with lowest priority i.e. 4 is pointed

away from the viewer and if ligands 1 to 3 are ordered such that the movement from ligand 1 to 3 passing through 2 (i.e. sequence 1→2→ 3) is in the clockwise direction, the chiral center is designated as R (*rectus* for right handed in Latin). If the ligands 1 to 3 are ordered such that the movement from ligand 1 to 3 passing through 2 (i.e. sequence 1→2→ 3) is in the counter-clockwise direction the chiral center is designated as S (*sinister* for left handed in Latin) [15].

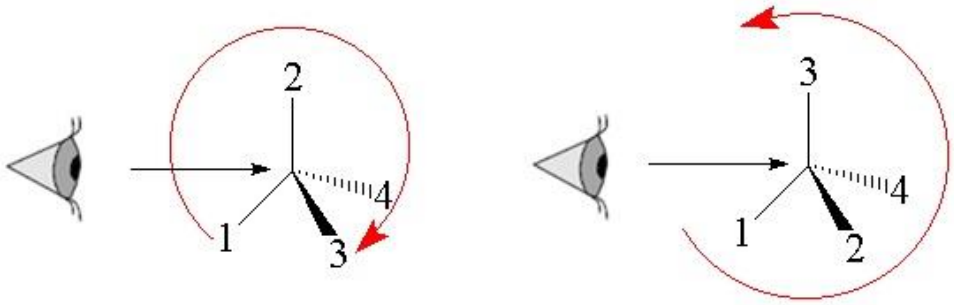

Clockwise
'R' configuration

Counterclockwise
'S' configuration

Figure 1.5 The CIP nomenclature identifies the handedness of chiral carbon atoms as S- or R-, based on the priority and arrangement of the four substituent groups around the chiral center. If the molecule is oriented such that the ligand with lowest priority i.e. 4 is pointed away from the viewer and if the ligand 1 to 3 are ordered such that the movement from ligand 1 to 3 passing through 2 (i.e. sequence 1→2→ 3) is in the clockwise direction the chiral center is designated as R. Vice versa if the ligands 1 to 3 are ordered such that the movement from ligand 1 to 3 passing through 2 (i.e. sequence 1→2→ 3) is in anti-clockwise direction the configuration movement in the anti-clockwise direction the chiral center is designated as S.

1.3 Significance of molecular chirality

In the absence of a chiral influence, a chemical reaction that results in a chiral product produces an equimolar mixture of two enantiomers of opposite handedness and such a mixture is called a ‘racemic mixture’ [16]. Since the differences between the two molecules comprising a racemic mixture are only manifested in chiral environments, separation of these molecules can be extremely complex and cost intensive. The process of separating two enantiomers from a racemic mixture is called ‘chiral resolution’. Development of efficient and cost-effective chiral resolution or enantioselective processing technologies is one of the primary objectives in the field of stereochemistry.

The human body is a chiral environment. The majority of pharmaceutical molecules are chiral and the two enantiomers can have completely different physiological impacts when ingested, i.e. while one of them is therapeutic the other can be toxic. Ignorance of this fact led to one of the most disastrous medical tragedies of all time, the ‘thalidomide tragedy’ [17, 18]. Thalidomide was a drug prescribed to help pregnant women with the effects of morning sickness. While R-thalidomide functioned in a therapeutic manner, its counterpart S-thalidomide acted as a teratogen and resulted in many forms of birth defects. The negative effects of thalidomide led to the development of more structured drug regulations and control over drug use and development [19]. Similarly, S-penicillamine is used as a form of immunosuppressant to treat rheumatoid arthritis while R-penicillamine is highly toxic [20]. R-prilocaine is an injectable local anesthetic commonly used owing to its low cardiac toxicity, but its mirror image molecule

S-prilocaine induces methemoglobinemia, which is characterized by reduction in the amount of hemoglobin which is essential for oxygen transport in human body [21]. The potential technological impact of enantioselective chemical processing can be realized from the fact that chiral pharmaceutical industry is a nearly a trillion dollar industry with an annual growth rate of ~10% [22].

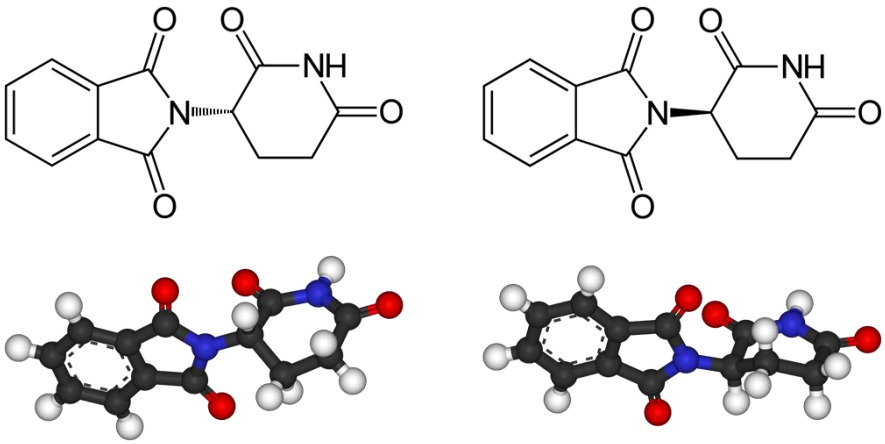

R-thalidomide **S-thalidomide**

Figure 1.6 R- and S- enantiomers of thalidomide. While R-thalidomide functions in a therapeutic manner, its counterpart S-thalidomide act as a teratogen and resulting in birth defects in babies. Appreciation of differences in the manner in which these two enantiomers of thalidomide react with the human body could have averted the most disastrous medical tragedies of all times – 'the thalidomide tragedy'.

1.4 Asymmetric heterogeneous catalysis

In the previous section we discussed the significance of enantioselective processing of chiral compounds. In the field of catalysis, application of chiral catalysts for such enantioselective processes is classified as 'asymmetric catalysis'. Over the past few decades, significant developments in this area of catalysis have expanded the scope of catalytic reactions with high enantioselectivity and efficiency. Despite this, however, most chiral chemicals are still produced using naturally occurring chiral molecules as initial reactants or through resolution of racemic mixtures [23]. Further, as far as commercial production of pure enantiomers employing asymmetric catalysis is concerned, the majority of the methods are based on homogeneous catalysis. While the advantages of homogenous asymmetric catalytic processes include high enantioselectivity and high activity, the major drawback of these processes include difficulty of separation and reusability. Heterogeneous asymmetric catalysis, on the other hand, involving chiral surfaces as catalysts for enantioselective reactions, is an extremely appealing route owing to its potential economic advantages and has attracted a great deal of interest over the last decade [23].

The fundamental basis of heterogeneous asymmetric catalysis is utilization of chiral surfaces as a media for facilitating enantioselective processes [23]. These surfaces can be obtained in various ways including – modification of a substrate surface using chiral modifiers or templates, cleavage of crystals having

chiral bulk structures and exposing high Miller index surfaces of achiral crystalline materials such that the exposed surface is chiral [24].

1.4.1 Chiral surfaces obtained using 'modifier'

One way to obtain chiral surfaces is to attach or immobilize a chiral homogenous catalyst to a support so as to combine the advantages of homogenous chiral catalysts with those of heterogeneous catalysts, wherein the catalyst can be separated from the reaction mixture to be used multiple times. Examples of catalyst immobilization include stationary phases used for chromatographic separations [24-27].

Another common and versatile approach to preparing chiral surfaces is to adsorb an enantiomerically pure chiral compound onto the surface of otherwise achiral substrate. As long as the adsorbed molecules retain their chirality, the surface interaction with other chiral molecules will be enantiospecific [28-31]. In some cases, upon adsorption of a modifier molecule, the surface atoms of the metal substrate assemble in specific patterns which lack mirror symmetry thereby imparting chirality to the surface. This phenomenon is called 'surface reconstruction' and it is observed in case of alanine, glycine and lysine adsorption on Cu(110) [32-34].

The most widely studied examples of chirally modified enantioselective catalysts include: Ni templated with tartaric acid and used for β-ketoester hydrogenation, and Pt templated with cinchonidine and used for α-ketoester hydrogenation [31, 34-43]. In addition to tartaric acid, α-amino acids have been used as modifiers for Ni [44]. The superiority of tartaric acid is believed to

originate from its ability to stereospecifically orient the β-ketoester molecules on the surface via hydrogen bonding [45]. Amino acids have also been identified as modifiers for other catalyst surfaces [46]. Alanine and glycine are chiral and upon adsorption on achiral Cu(110) , these acids form well-ordered arrays, the structure of which is believed to be driven by hydrogen bonding, thereby imparting chirality to the surface [47-51].

1.4.2 Surfaces obtained from bulk chiral materials

Apart from chirally 'modified' surfaces, naturally chiral surfaces can be derived from intrinsically chiral bulk crystalline structures. For example, quartz is a common chiral material whose bulk is formed by a chiral helical arrangement of corner-sharing SiO_4 tetrahedra. Chiral surfaces can be obtained by exposing surfaces of such naturally chiral bulk crystalline solids. The chirality of the exposed surface is dictated by the chirality of the bulk. Crystallization of enantiomerically pure sample of an organic compound produces crystals which are chiral. Surfaces exposed from such crystals must be chiral and should possess enantiospecific properties.

1.4.3 Naturally chiral surfaces

Although it sounds counterintuitive, it is also possible for achiral crystalline materials to expose surfaces that are naturally chiral [52]. The work in this thesis focuses on achiral low Miller index and high Miller index naturally chiral Cu surfaces. Cu is a metal with a face-centered cubic (FCC) crystal structure. Figure 1.9 shows the low Miller-index crystal surfaces of an FCC metal. Chiral surfaces can be obtained by exposing low symmetry high Miller index

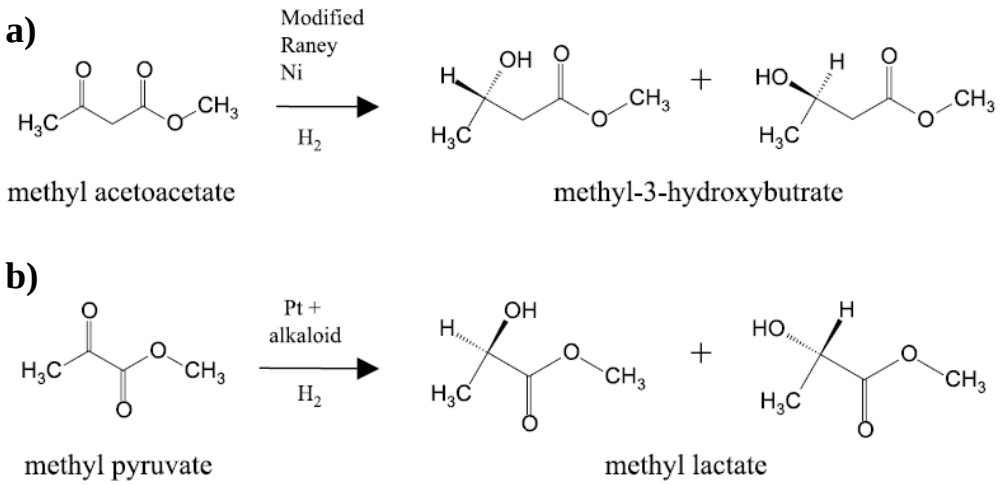

Figure 1.7 Asymmetric hydrogenation of a) methyl acetoacetate on Ni templated with tartaric acid and b) methyl pyruvate on cinchonidine are the most widely studied examples of enantioselective reactions catalyzed by chirally templated surfaces.

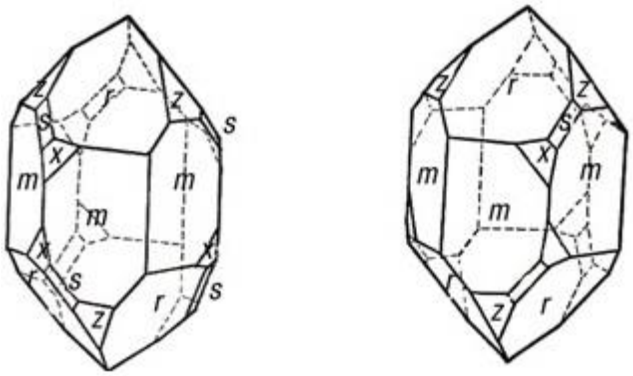

Left-handed quartz **Right-handed quartz**

Figure 1.8 Crystals of quartz having opposite handedness. The figure illustrates the left- and right-handed crystal forms of natural quartz. Quartz has an inherently chiral bulk crystalline structure formed by helical arrangement of corner-sharing SiO4 tetrahedra. Every crystallographic face exposed by quartz is intrinscically chiral and chiral surfaces can be obtained by exposing surfaces of such naturally chiral bulk crystalline solids like quartz. The chirality of the exposed surface is dictated by the chirality of the bulk.

planes (*hkl*) from crystalline materials with achiral bulk structures, like Cu, such that $h \neq k \neq l \neq h$ and $h \cdot k \cdot l \neq 0$. In general, such surfaces have characteristic structures composed of terraces, steps and kinks. It is the orientation of the exposed kinks that imparts chirality to the surface. Each kink is formed by the intersection of three low Miller index micro-facets ({111}, {100}, and {110}) and the chirality of the surface is identified from the sense of rotational progression among these three micro-facets. An example Cu(643)$^{R\&S}$ surfaces is shown in Figure 1.10. Such naturally chiral high Miller index surfaces can serve as a media for enantioselective processing [30].

1.4.3.1 R-3-methylcyclohexanone on Cu(643)$^{R\&S}$

For over two and half decades Gellman and coworkers have consistently focused on studing the enantiospecific surface chemistry of chiral molecules such as R-3-methylcyclohexanone [24, 53-55], R-2-bromobutane [56], S-1-bromo-2-methylbutane [57], R- and S-propylene oxides [56, 58] on Cu(*hkl*)$^{R\&S}$ surfaces. Let us consider the example of R-3-methylcyclohexanone on Cu(643)$^{R\&S}$, which is the most extensively studied system in our group. An investigation involving a technique called temperature programmed desorption (TPD) revealed an enantiospecific difference of 3.5 K between desorption peak temperature between the Cu(643)^{R} and Cu(643)^{S} surfaces, as shown in Figure 1.11 [24, 59]. Details about the TPD technique are provided in chapter 2 of this thesis. By comparing with TPD features on achiral surfaces including Cu(111), Cu(533) and Cu(221), it was demonstrated that this enantiospecific desorption results from the kinks on the chiral surfaces [24, 59]. From the same study of R-3-methylcyclohexanone

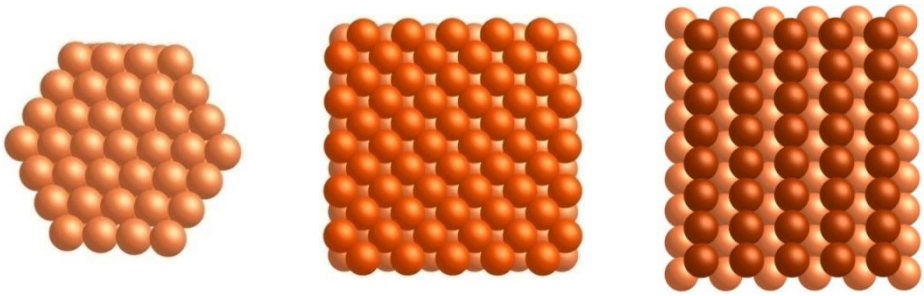

Figure 1.9 Low Miller index surfaces of materials having face-centered cubic (FCC) crystalline structure. The (111) surface is the most densely-packed with triangular or hexagonal packing. The (100) surface is square grid-like. The (110) surface is the least densely-packed and it consists of rows of atoms separated by troughs. Cu is a metal with a face-centered cubic (FCC) crystal structure.

Cu(643)^{S} **Cu(643)^{R}**

S-kink **R-kink**

over Cu(643)$^{R\&S}$ surfaces we can note that, in spite of a significant 3.5 K shift in the temperature of the desorption peaks, the two peaks cannot be well-resolved because the full width at half maximum (FWHM) of the peaks is 25 K. The ratio of the enantiospecific peak shift, ΔT_p^{RS}, to the FWHM, ΔT_{FWHM}, which can be defined as the resolution factor R^{RS}, is very small in this case; $R^{RS} = \Delta T_p^{RS} / \Delta T_{FWHM} = 0.14$. Similar observations pertaining to low resolution of TPR spectra were made in the case of other above-mentioned probe molecules studied on Cu(643)$^{R\&S}$ surfaces. To obtain greater enantioselectivity we must achieve either a larger ΔT_p^{RS}, reduce ΔT_{FWHM} i.e. narrow peaks in TPR spectra, or both. In each case one would be aiming to achieve a high value of the resolution factor R^{RS}, which is an indication of the resolution between the two peaks and consequently an indication of greater enantiospecificity. These kind of narrow peaks are a characteristic of a surface phenomenon called ‘surface explosion’.

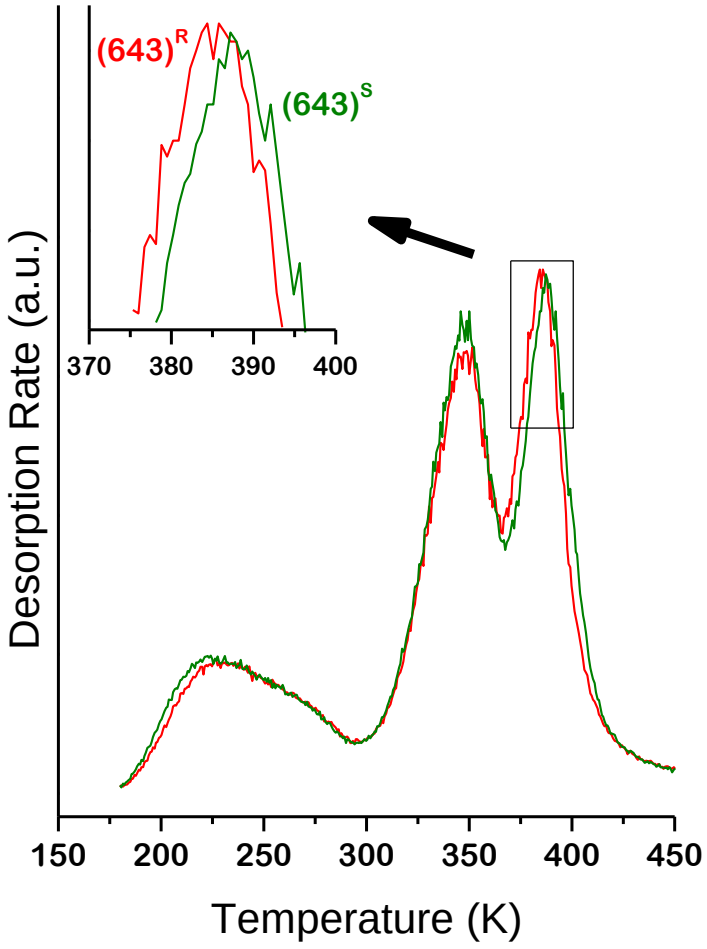

Figure 1.11 TPD spectra of R-3-methylcyclohexanone on the Cu(643)$^{R\&S}$ surfaces. A 3.5 K shift of desorption peak temperature was observed from the Cu(643)^{R} surface to the Cu(643)^{S} surface. The full width at half maximum (FWHM) of the peaks is 25 K. The ratio of the enantiospecific peak shift, ΔT_p^{RS}, to the FWHM, ΔT_{FWHM}, which can be defined as the resolution factor R^{RS}, is very small in this case; $R^{RS} = \Delta T_p^{RS} / \Delta T_{FWHM} = 0.14$.

1.5 Surface explosion

1.5.1 Autocatalytic reaction mechanisms

Autocatalytic reaction mechanisms are observed in a variety of important chemical processes including catalysis, radical-mediated explosions and biosynthesis. In asymmetric heterogenous catalysis, surface reactions that proceed by autocatalytic mechanisms, in many instances, are referred to as surface explosions [60-69]. Surface explosion can be defined as an autocatalytic increase in the reaction rate with increasing extent of reaction. A characteristic of these processes is that even under isothermal conditions the rate of the reaction accelerates with the extent of the reaction. The surface explosion reaction mechanism is similar to that of the classical radical chain explosion mechanism. In a chain reaction a radical intermediate formed in one step generates a radical intermediate in a subsequent step, which in turn generates another intermediate, and so on. These intermediates are referred as chain carriers. In radical chain reactions, radicals (i.e. species with unpaired electrons) act as chain carriers. During radical chain explosion reactions there is a branching step in which reaction of one radical species produces two radicals, $\bullet \rightarrow 2\ \bullet$. In absence of radical quenching reactions, the branching steps result in an exponential increase in the radical concentration with time.

1.5.2 Explosive surface decomposition

In the case of a surface reaction, a similar condition can arise if the adsorbate decomposition reaction requires the presence of an empty site or

vacancy. For example, consider decomposition of A_2 followed by rapid desorption of the reaction product A_g in the gas phase,

$$A_2 \bullet + \bullet \rightarrow 2\ A\bullet \rightarrow 2\ A_g + 2\bullet$$

where $\bullet$ represents an adsorption site. Thus, A_2 adsorbed on a surface utilizes an empty site $\bullet$ on a surface to undergo decomposition and once it has undergone decomposition, two empty sites become available on the surface which can be used by two other molecules for undergoing decomposition, so on and so forth, resulting in an exponential growth in vacancy concentration with time, leading to surface explosion.

Surface explosions were first reported in the work of Falconer and Madix on the decomposition of formic acid on Ni(110) surfaces [60-62]. Since then, the reaction mechanism has been observed in the decomposition of formic acid and acetic acid on several metal surfaces [67, 70-77]. Mixed overlayers of NO + CO on Pd and Pt surfaces, and NO + H_2 on Pt surfaces, also exhibit explosive reaction kinetics [63, 64, 78-80]. Another example is the autocatalytic dissociative adsorption of water on Ni and Cu surfaces [65, 81-83]. In this case the dissociation probability of water molecules on the surface depends on the coverage of adsorbed species. While most of these studies have been performed on low Miller index single crystal metal surfaces under ultra-high vacuum conditions, surface explosions have also been observed for acetate decomposition on nanoparticulate Rh catalysts operating at atmospheric pressures [67, 84].

The majority of these studies have relied on temperature programmed reaction spectroscopy (TPRS) as the primary method for studying explosive

kinetics. In temperature programmed reaction spectroscopy (TPRS), the reactants are first adsorbed on the surface of interest, typically kept at low temperature. The substrate is then heated in a specific programmed manner, i.e. at constant heating rate or isothermally, to induce the surface reaction and the rate of desorption of product(s) is monitored using a mass spectrometer. A typical temperature programmed reaction spectrum is a plot of product desorption rate as a function of time or temperature.

There are two key characteristics of explosive surface reaction kinetics exhibited in a TPRS experiment. First is the observation of product TPR spectrum having unusually narrow width (ΔT_p = 1- 5 K) i.e. reaction occurring over very narrow temperature ranges that cannot be accounted for by standard zero-, first- or second-order reaction kinetics. The second characteristic is the observation of an increase in the rate of reaction as a function of time during isothermal heating. Ultimately, of course, the surface reaction rates decline as the adsorbed reactant gets depleted and the reaction approaches completion. These two characteristic phenomena of surface explosions can only be understood in terms of rate laws or kinetics that describe autocatalytic processes.

1.5.3 Rate laws describing explosive kinetics found in literature

The most common model explaining explosive surface kinetics, assumes that the rate law of these autocatalytic processes is a function of both the coverage of adsorbate and the number of vacant sites on the surface. As a result, the model assumes the rate law of the form,

$$r = k \cdot \theta \cdot (1 - \theta) \qquad \ldots\ldots (1.1)$$

where θ represents a fractional coverage of the adsorbate relative to its saturation coverage on the surface [66, 67, 69, 85, 86] and the $(1-\theta)$ term represents the areal vacancy concentration. The unrealistic feature of this model is that at saturation coverage i.e. when θ = 1, there are no vacant sites available on the surface to initiate the reaction and as per the above rate law the adsorbate should be stable indefinitely and to infinite temperatures, which cannot be the case. Some models describing this process use a mean field approach such as eq. 1 in which the adsorbates and vacancies are assumed to be diffusing rapidly on the surface [66]. Others assume that the vacancies form empty patches, i.e. islands on the surfaces and that decomposition only occurs along the edges of these growing vacancy islands. This leads to rate laws of the form

$$r = k \cdot \theta \cdot (1-\theta)^{1/2} \qquad \ldots\ldots (1.2)$$

where the $1/2$-order power of the vacancy concentration term is arises from the relationship between the perimeter and the area of the vacancy islands [77, 87].

1.5.4 Autocatalytic reaction initiation

One of the most poorly understood steps in surface explosions is the initiation process. This is perhaps the most important step as far as the autocatalytic process is concerned since, an important question arises that, when the surface is saturated, i.e. initial adsorbate coverage is θ = 1, how is process initiated ? Many of the attempts to explain this phenomenon while modeling the TPR spectra of explosion processes have invoked rate laws of the form

$$r = k \cdot \theta \cdot (1-\theta+f) \qquad \ldots\ldots (1.3)$$

where f represents the concentration of initiation sites [62, 76, 88]. Vacancies or initiation sites in adsorbate overlayers could be imagined to be formed by thermal fluctuations in local density or some irreversible process such as adsorbate desorption. In several cases these initiation sites have been associated with the defects on the surface; although there is no direct evidence that this is the case.

1.6 Thesis objectives and overview

Application of naturally chiral metal surfaces is a novel and an interesting approach to illustrate a mechanism by which catalysts can impart enantioselectivity. They also serve as a nice model system for understanding the origins of enantioselectivity. Gellman and co-workers have previously demonstrated that these surfaces are capable of chiral recognition at molecular level [1, 2]. Study of the fundamental aspects of autocatalytic surface explosions and further exploiting this phenomenon to demonstrate extremely high enantiospecificity on naturally chiral metal surfaces is the primary objective of the work presented in this thesis. The two main systems employed in this study include chiral tartaric acid and chiral aspartic acid on well-defined Cu single crystal surfaces.

Chapter 2 covers the details of various experimental procedures and surface science techniques used in this research. The work presented in this thesis is based on three surface sensitive ultra-high vacuum techniques including, temperature programmed reaction spectroscopy (TPRS), x-ray photo-electron spectroscopy (XPS), and low energy electron diffraction (LEED).

Chapter 3 is based on our findings pertaining to explosive decomposition of tartaric acid on Cu(110), with focus on initiation of the reaction. By performing TPRS, LEED and STM (Sykes group) experiments under isothermal conditions, we have been able to successfully investigate the initiation of surface explosions. Based on our findings, we have been able to propose rate laws and model these reactions more accurately than any previous studies described in the literature.

Chapter 4 focusses on investigating the autocatalytic decomposition chemistry of aspartic acid on Cu(110) by employing various aspartic acid isotopomers having specifically labeled atoms. By performing TPRS experiments, we were able to identify various products formed over the course of the reaction and also correlate the atoms in specific products to their position on the decomposing molecule. Using XPS we were able to identify the state of the molecule before the reaction initiates and different chemical species / groups on the surface during the decomposition process.

Chapter 5 focusses on decomposition of tartaric acid on Cu(*hkl*)$^{R\&S}$ surfaces. We have been able to successfully demonstrate extremely high enantiospecificity in the case of tartaric acid on Cu(643)$^{R\&S}$ surfaces. Other group members have also shown that high enantiospecificity can be attained in similar manner on other Cu surfaces including Cu(17,5,1)$^{R\&S}$, Cu(531)$^{R\&S}$ and Cu(651)$^{R\&S}$ [1, 2]. These are extremely important results which offer first-hand demonstration of super-enantiospecificity attained using naturally chiral surfaces. By comparing the explosive TA decomposition kinetics on Cu(110) and the stepped, kinked Cu(651) surface, we provide evidence that static structural defects in the surface are not the sites of explosion initiation.

In chapter 6, the conclusions of the thesis are presented with a short discussion of various avenues for future work based on the findings of this research.

Chapter 2

Experimental Techniques and Procedures

2.1 Ultra-high vacuum (UHV) systems

All the experiments detailed in this thesis were performed in stainless steel ultra-high vacuum (UHV) systems, typically referred to as UHV chambers. Ultra-high vacuum is a vacuum level characterized by pressures lower than 10^{-9} Torr [89]. UHV conditions are required for most surface science experiments for two principle reasons:

1) To maintain atomically clean surfaces for the duration of the experiment (for ~30 min long experiment to be performed at a contamination level of ~ 1%, a base pressure of $<10^{-9}$ needs to be achieved and maintained over the course of the experiment) [89].
2) To prevent undue interference from gas phase scattering during low energy electron and ion-based experimental techniques [90].

In all, three different chambers were used depending upon the scope of the study: Chamber I (Figure 2.1) was used for TA/Cu(110), TA/Cu(643)$^{R\&S}$ and Asp/Cu(110) study. Primary experiments performed on this system include x-ray photoelectron spectroscopy i.e. XPS for coverage determination (using a ThermoVG Scientific XR3HP X-ray source and Omnicron EA125 analyzer), low energy electron diffraction i.e. LEED (using SPECS Er LEED 1000-A optics) and temperature programmed reaction spectroscopy i.e. TPRS (using AMETEK MA 200 MF mass spectrometer).

Chamber II (Figure 2.2) was used for TA/Cu(110) study. Primary experiments performed on this system include LEED (using OCI Vacuum Microengineering LEED optics with 77˚ solid angle view and a 75 mm diameter dual microchannel-plate for image intensification) and TPRS (using AMETEK MA 200 MF mass spectrometer).

Chamber III i.e. Thetaprobe was used for Asp/Cu(110) study. This system was primarily used for XPS experiments (using a Thermoscientific MXR1 monochromatic X-ray source and a 'Theta' Spectrometer) to identify the chemical states of different atoms i.e. chemical groups present on the surface.

More details on the experimental techniques are included in the following sections of this chapter, whereas the subsequent chapters discuss the actual results and findings. For all the systems, ultra-high vacuum conditions were attained using a series of pumps operated in a sequential manner. These pumps can be characterized depending upon the level of vacuum they can attain, namely, low-vacuum pumps, high-vacuum pumps and ultra-high vacuum pumps. For all the three chambers, low vacuum conditions ($>10^{-3}$ Torr) were attained using an oil filled dual stage rotary vane pump (Varian DS 202), while the high-vacuum conditions ($10^{-3} – 10^{-8}$ Torr) were attained using a turbo-molecular pump (Pfeiffer Vacuum TMU 260 PMP02135) backed by a rotary vane pump. Low vacuum pressure measurements were performed using a Varian thermocouple (TC) gauge while the high-vacuum and UHV pressure measurements were performed using a hot filament ionization gauge (Varian L8350301). For attaining UHV conditions, different pumps were used for each of the three different chambers. Chamber I

(Figure 2.1) was equipped with a Low Profile 400 ion pump by Physical Electronics, chamber II (Figure 2.2) was equipped with a Cryo-Torr 8 two-stage cryo pump by CTI-Cryogenics, and chamber III i.e. the Thetaprobe was equipped with a 240 L/s turbo-molecular pump and a titanium sublimation pump (TSP). The pumping system allowed attainment of pressure conditions of $<10^{-8}$ Torr within 4 hours of continuous pumping. The quality of vacuum was further enhanced by performing an overnight bakeout i.e. heating the system to 400 K, after which the background pressure drops to $<10^{-9}$ Torr.

Figure 2.4 depicts the schematic representation of a typical UHV chamber in our lab. The chamber consists of the following components:

1) Main chamber body
2) LEED optics
3) Hot cathode ionization pressure guage
4) Gate valve between the UHV pump and the chamber enclosure
5) UHV pump (ion pump in case of chamber I and Cryo-pump in case of chamber II)
6) Sputter ion gun
7) Substrate / single crystal sample
8) Hemispherical energy (photoelectron) analyzer
9) Doser
10) X-ray source
11) Sample position manipulator
12) Viewport

13) Mass spectrometer (not shown)

14) Precision leak valve (not shown) for introducing gases

15) Secondary gate-valve (not shown) for connecting the turbo pump and the mechanical pump.

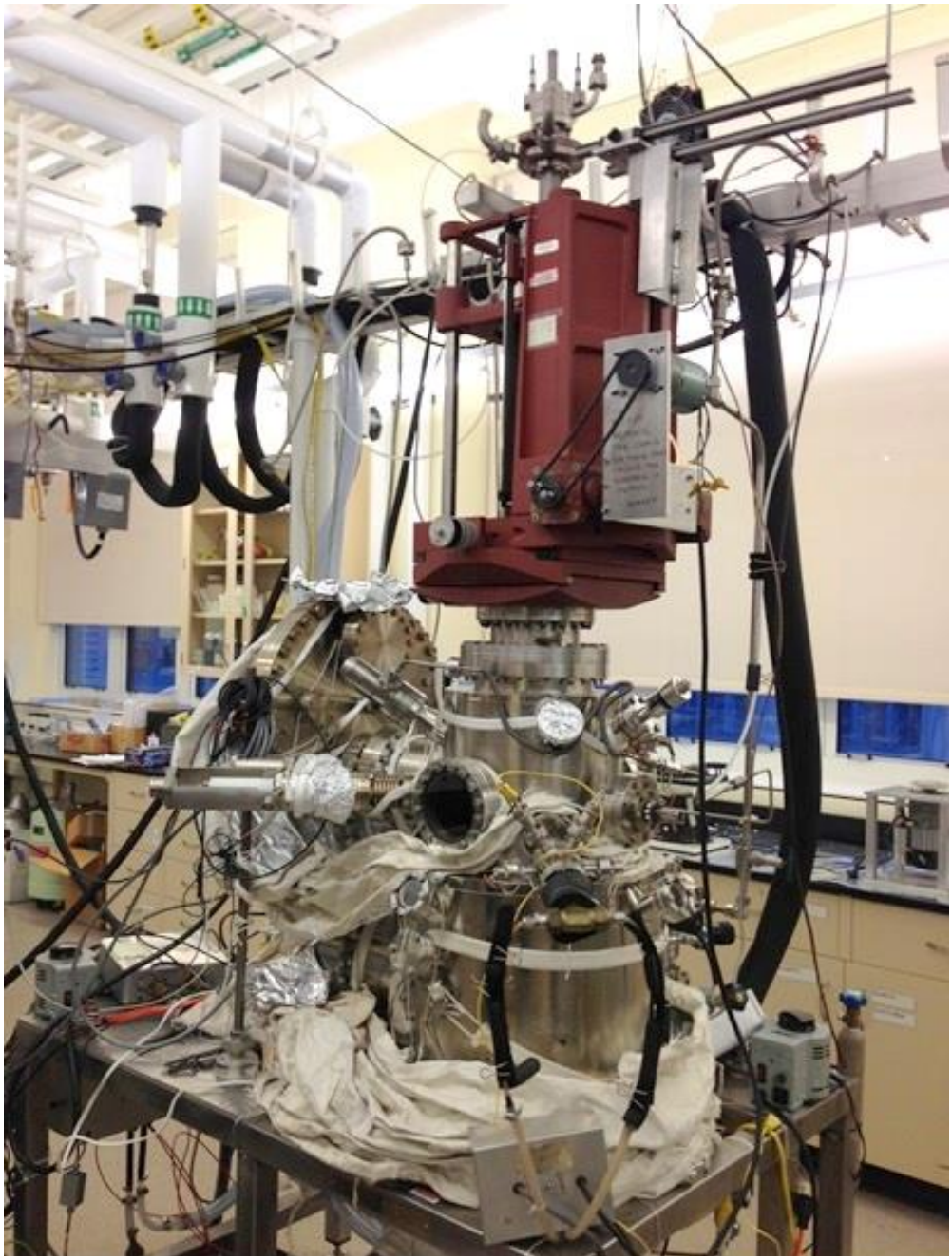

Figure 2.1 Chamber I was used for TA/Cu(110), TA/Cu(643)$^{R\&S}$ and Asp/Cu(110) studies. Primary experiments performed on this system include: XPS for coverage determination, LEED and TPRS.

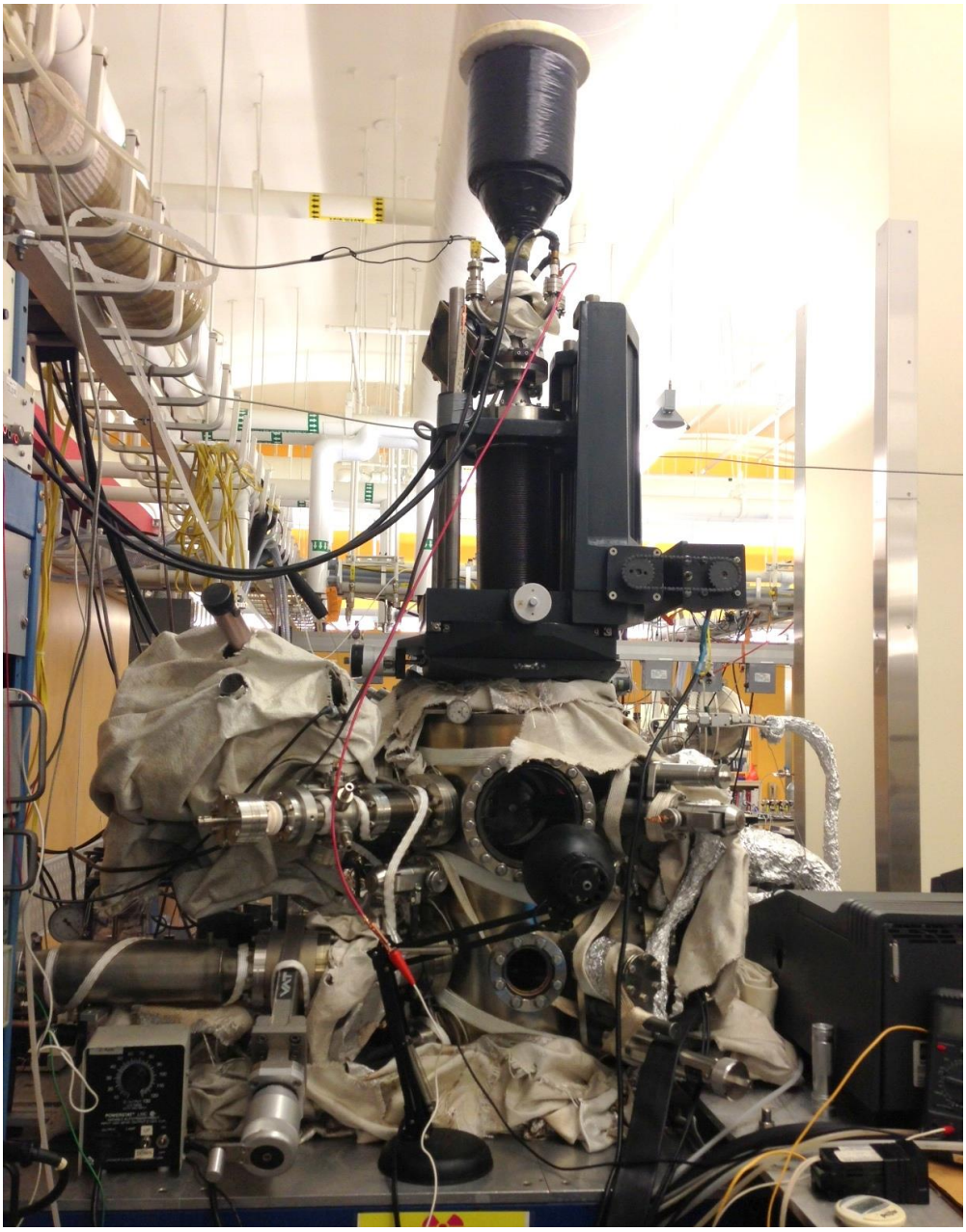

Figure 2.2 Chamber II was used for TA/Cu(110) study. Primary experiments performed on this system include LEED and TPRS.

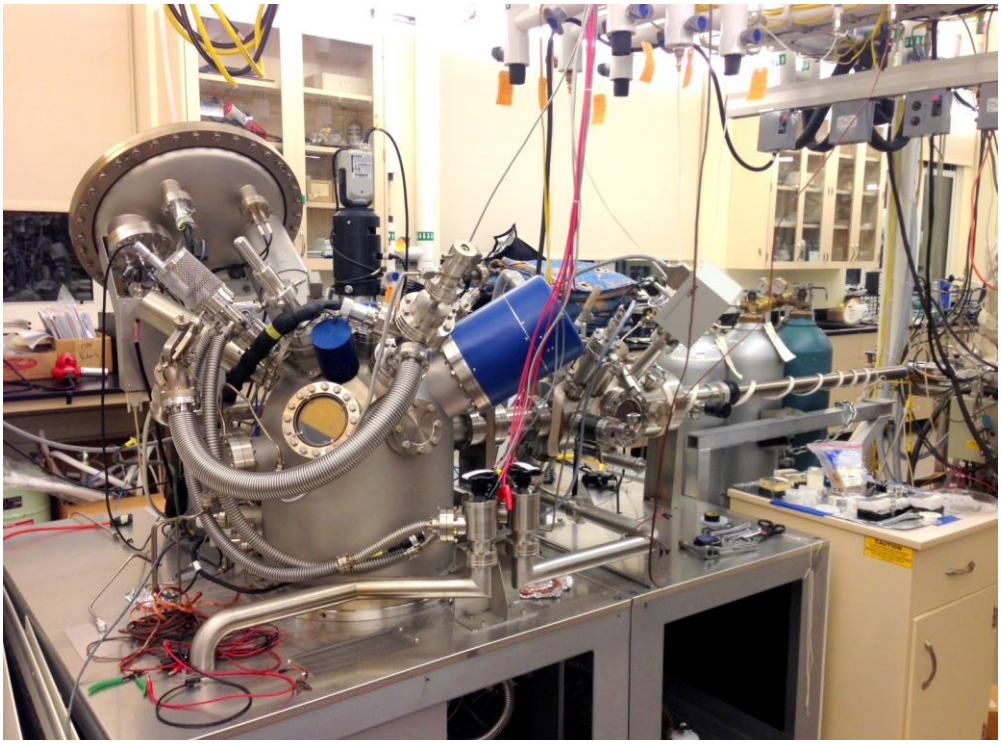

Figure 2.3 Chamber III i.e. Thetaprobe was used for Asp/Cu(110) study. This system was primarily used for XPS experiments to identify the chemical states of different atoms i.e. chemical groups present on the surface.

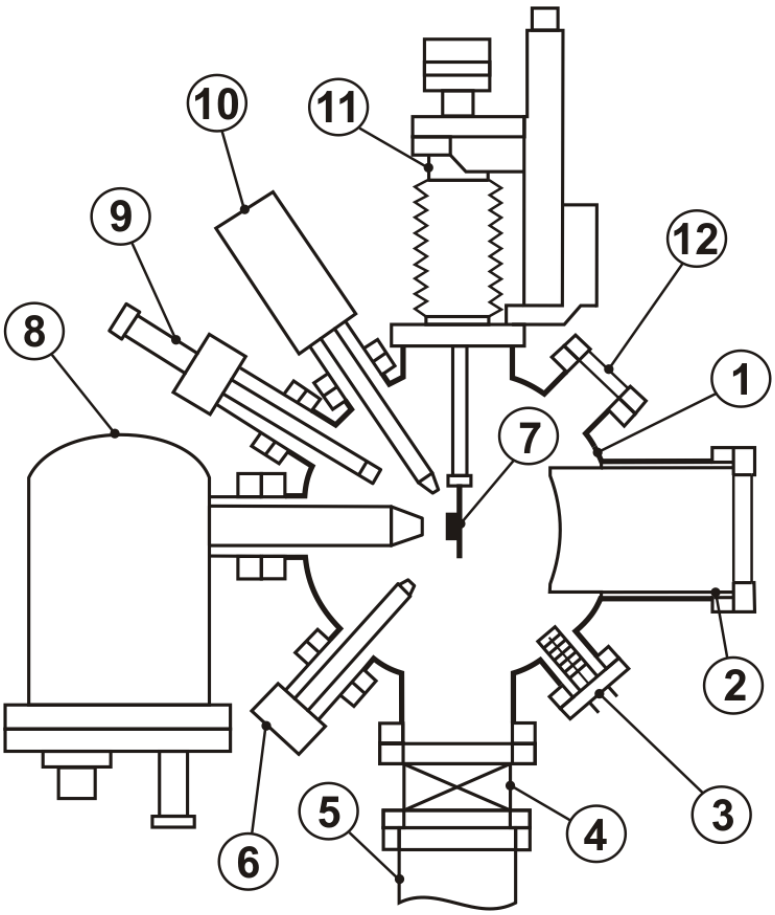

Figure 2.4 Schematic diagram of a typical UHV system in our lab. This figure represents the exact schematic of chamber II and it is adapted from Pushkarev's thesis. The UHV system consists of: 1) chamber body, 2) rear view LEED optics, 3) ionization pressure gauge, 4) primary gate valve, 5) UHV pump, 6) sputter ion gun, 7) single crystal sample, 8) hemispherical energy analyzer, 9) sublimation doser, 10) dual Mg/Al anode X-ray source, 11) XYZ- sample manipulator, 12) viewport, and a precision leak valve (not shown) used for filling the chamber's volume with Ar gas.

2.2 Experimental techniques

2.2.1 Temperature programmed reaction spectroscopy (TPRS)

Thermal desorption methods are the most widely performed experiments to study the kinetics and energetics of a desorption process [89, 91]. Measurements of desorption kinetics are usually performed using an experiment called temperature programmed desorption (TPD). When molecules adsorb and then desorb reversibly without reacting on the surface, TPD can be used to measure the desorption energy, ΔE_{des}. Reversible desorption assumes that the desorption energy ΔE_{des} is lower than any barrier to reaction and thus it is the preferred reaction channel for a molecule on a surface. Temperature programmed reaction spectroscopy (TPRS) is used to measure reaction kinetics and identify the products of surface reactions other than desorption. If the adsorbed molecules react rather than desorb from the surface then it is not possible to use TPD experiment to measure desorption energies. This occurs when the barrier to reaction is lower than the barrier to desorption. In such cases, it is often possible to detect the products desorbing from the surface. This can provide both, an identification of the reaction products and a measure of the barrier to surface reaction ΔE_{dec}.

In TPRS, the progress of a reaction is studied by monitoring the products and the rate of formation of the products during the reaction using a mass spectrometer, while varying the temperature of the sample in a systematic manner. The primary advantage of the TPRS technique lies in its experimental simplicity; however, the challenge lies in interpreting the experimental data in an

accurate and unambiguous manner [89]. Because of this, TPRS is generally used in conjunction with other surface science techniques as well as with kinetic modeling of the experimental data.

2.2.1.1 Mass spectrometer

Using a mass spectrometer, one can identify the individual molecules that have been ionized. This technique provides fingerprint identification of the structural and chemical properties of the molecules. The three principle steps involved in the working of a mass spectrometer are – ionization, separation and detection.

i. *Ionization*

As current flows through the mass spectrometer filament, it glows and emits free electrons. These electrons are accelerated towards the ionizer body by applying a potential difference between the filament and the ionizer body. Here, the electrons collide with the molecules to form positive ions. These ions are extracted from the ionization chamber and focused towards the quadrupole mass filter by a potential difference. When a single electron is removed, a positive ion is created which is referred to as a molecular ion. When the bombarding electrons cause the molecular bonds to break, fragment ions are formed. The fragments ions and their relative intensity (i.e. number of fragment ions formed) often serve as molecular signatures while correctly identifying the products.

ii. *Separation*

Once the ions reach the quadrupole mass filter, they are filtered on the basis of their mass-to-charge (*m/q*) ratio. The quadrupole mass filter is constructed of four

electrically-conducting, parallel cylindrical rods. A constant DC voltage and an alternating RF voltage are applied along the length of the rods. As an ion enters the quadrupole mass filter, the RF and DC fields cause it to undergo oscillations. The values of RF and DC can be set such that only the ions having a particular *m/q* ratio will have stable trajectories between the quadrupoles and can therefore exit the mass filter. Ions with any other *m/q* ratio will have unstable trajectories and get neutralized as they strike the quadrupole rods or the assembly housing. Positive ions that successfully pass through the quadrupole are further focused towards the detector using an exit aperture which is kept at a negative voltage.

iii. *Detection*

An electron multiplier is used as a detector for amplified sensitivity. The ions emerging from the quadrupole are attracted towards the multiplier which is kept at a negative potential. As the ions strike the multiplier, secondary electrons are emitted. This creates a cascading effect as each secondary electron further generates more secondary electrons and they travel down the multiplier tubewall. This results in an amplification of the original signal by a factor of around 10^3 - 10^6.

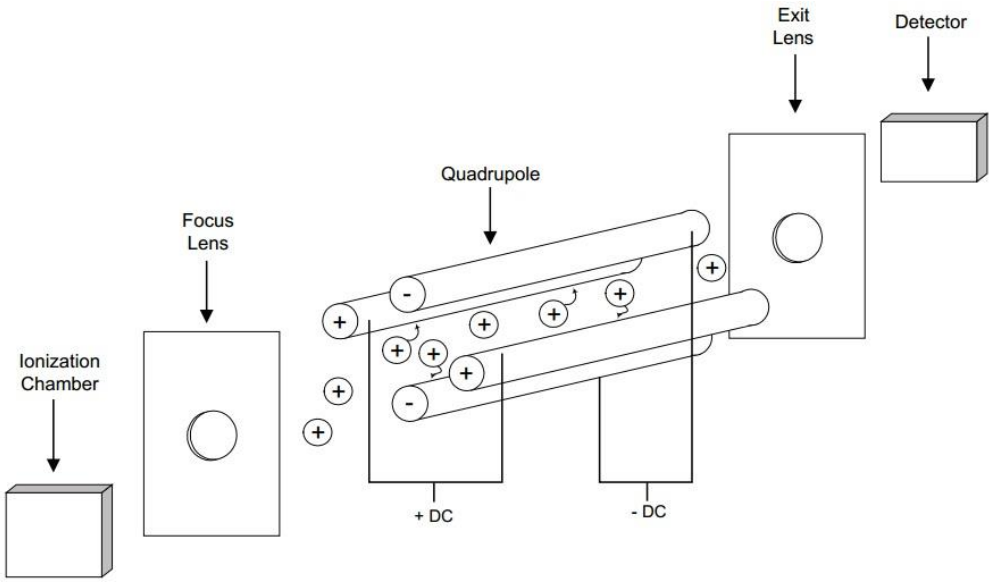

Figure 2.5 Typical components of a quadrupole mass spectrometer. Molecules are ionized in the ionization chamber from where they are extracted and focused towards the quadrupole mass filter by a potential difference. In the quadrupole mass filter, these ions are filtered on the basis of their mass-to-charge (m/q) ratio. Positive ions that successfully pass through the quadrupole are further focused towards the detector using an exit aperture which is kept at a negative voltage. An electron multiplier is used as a detector which amplifies the original signal by a factor of ~ 10^3 – 10^6.

2.2.1.2 TPRS experiment

The TPRS experiment is performed in vacuum so that the mass spectrometer can operate. A typical TPRS experiment involves the following four steps:

1. Surface preparation, which involves preparing a clean uniform surface which acts as a substrate for carrying out the reaction.
2. Adsorption of the reactant on the substrate, generally kept at a low temperature T_0.
3. Heating the substrate at a particular rate say, β K/sec. The temperature of the substrate at any instant is given by $T = T_0 + \beta \cdot t$, where t is the time after initiating the heating process.
4. Simultaneous detection of desorbing product by a mass spectrometer while heating the substrate. A typical TPRS spectrum is a plot of the rate of desorption of a species as a function of temperature (T) or time (t).

The mass spectrometer is tuned to a particular *m/q* ratio, depending upon the products that are desorbing from the surface; and it measures an ion current corresponding to those m/q ratio/s as a function of time (or temperature). The signal that is measured by the mass spectrometer is proportional to the partial pressure of the desorbing species which, in turn, is proportional to the desorption rate (assuming that the desorbing species are being pumped away rapidly):

$$\text{Signal}(T) \propto P(T) \propto r(T) \qquad \ldots\ldots (2.1)$$

The rate of desorption r_{des} is defined as the change in coverage with respect to time.

$$r_{des} = -d\theta/dt = -\beta(d\theta/dt) \qquad \text{..... (2.2)}$$

For most processes one thinks about the desorption rate simply as a reaction which can be zero-, first-, or second-order in the reactant concentration or coverage.

$$r_{des} = k \cdot \theta^n \qquad \text{..... (2.3)}$$

A TPRS experiment can be depicted physically as shown in Figure 2.7. Initially, there is a high coverage θ_0 of adsorbates on the surface, but the rate constant $k(T_0)$ is very low. Therefore the desorption rate is low. As the temperature increases, the rate constant for desorption increases and thus, the desorption rate increases. Because desorption is occurring, the coverage drops. At a particular temperature (T_p), the rate of desorption passes through a maximum and then drops back to zero.

The temperature at which the rate of desorption is maximum is called the peak desorption temperature (T_p). TPRS is an extremely versatile experimental technique and can be used to determine T_p and hence the energy barriers to the reaction i.e. ΔE_{dec}, the coverage θ of an adsorbed species, the number of adsorption sites on a surface, the types of adsorption sites on a surface, and the order *n* of the reaction [89]. From the perspective of our work, as the value of T_p is obtained directly from the TPR spectrum, the spectra can be used to detect enantiospecific differences in the reaction kinetics by demonstrating a difference in the desorption energies (i.e. difference in the values of T_p) between the two enantiomers from a same chiral surface or a single enantiomer from two different chiral surfaces.

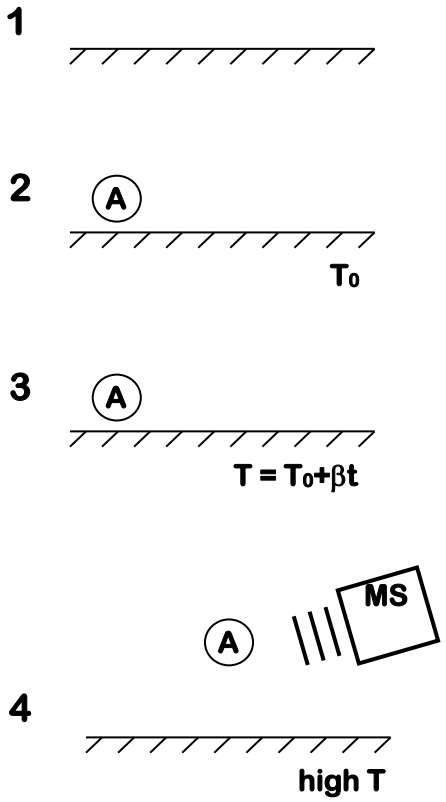

Figure 2.6 Steps in a typical TPRS experiment include: 1. Surface preparation. 2. Adsorption of the reactant on the substrate. 3. Heating the substrate in a systematic manner. 4. Simultaneous detection of desorbing product species by a mass spectrometer while heating the substrate.

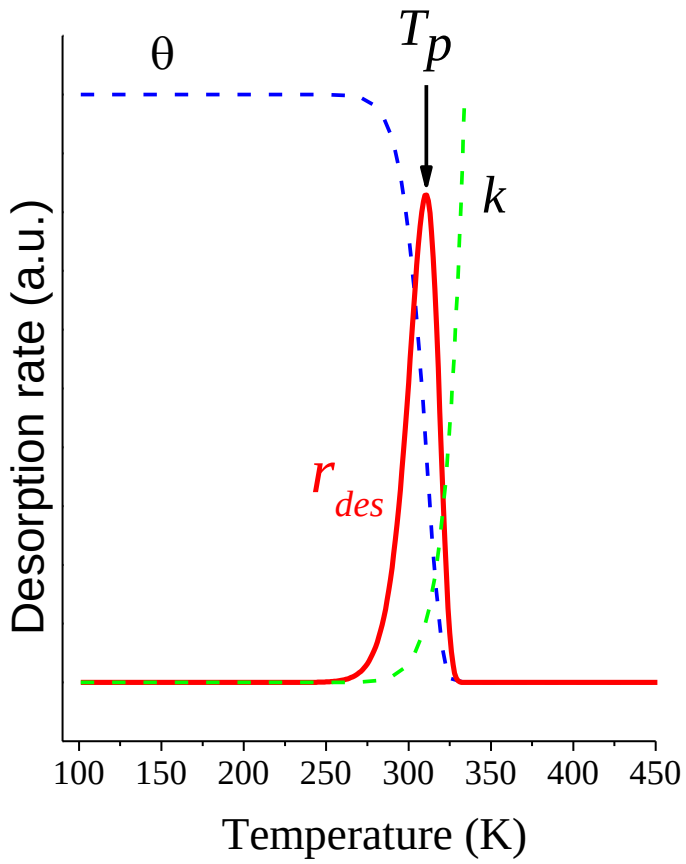

Figure 2.7: A typical TPR spectrum (in solid red line), i.e. a plot of desorption rate as a function of sample temperature. The maximum rate of desorption occurs at the peak temperature, T_p. The blue and the green lines represent the variation of surface coverage (θ) and rate constant (k) as a function of sample temperature T respectively.

2.2.1.3 TPRS experimental set up and procedures

The TPRS experiments were conducted in chambers 1 and 2. Both these chambers were equipped with Ametek MA 200 MF quadrupole mass spectrometers. A clean substrate sample was dosed with TA or Asp at a specific temperature, for a certain time interval and was then allowed to cool below 100 K. The filament and multipliers were turned on, the appropriate *m/q* ratios to be monitored, and the temperature profile to be followed during the experiment were set in the Dycor System 2000 software. Depending upon the experiment, up to 32 different masses could be monitored during a single TPRS experiment. The sample was then positioned ~1mm away from the mass spectrometer aperture and the experiment was initiated to obtain TPR spectra. A TPR spectrum for TA decomposition on Cu(110) at saturation coverage i.e. $\theta_0 = 1$, with a heating rate of $\beta = 1$ K/s collected between 450 to 550 K is depicted in Figure 2.8.

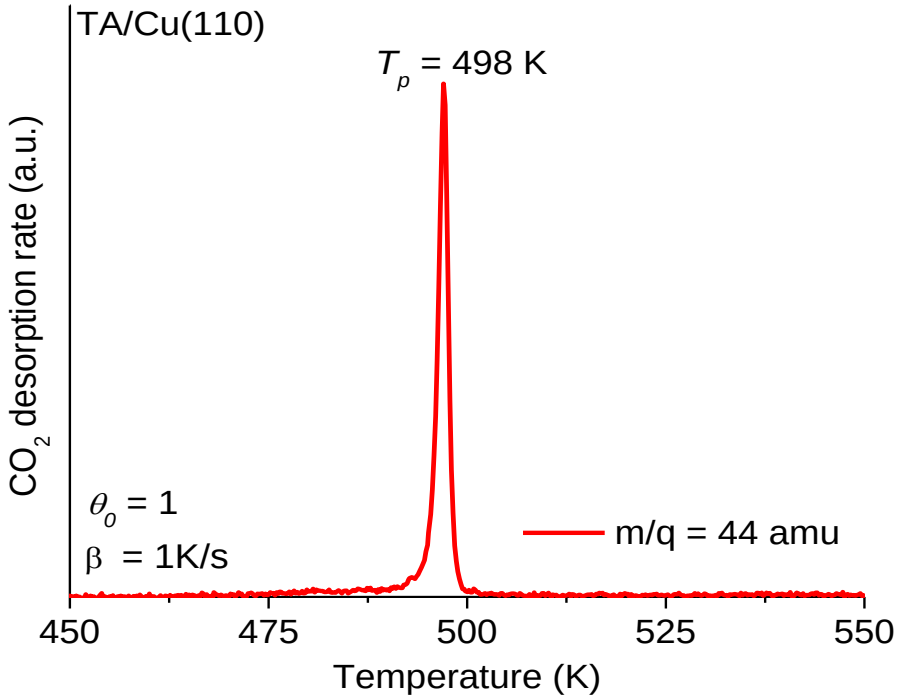

Figure 2.8 TPR spectrum monitored for CO_2 i.e. *m/q* = 44 amu desorption obtained during TA decomposition on Cu(110) at saturation coverage i.e. θ_0 = 1, with a heating rate of β = 1 K/s between 450 to 550 K.

2.2.2 Low Energy Electron Diffraction

Low energy electron diffraction (LEED) is the primary method for surface structure determination and is a commonly used technique in most surface science studies. LEED can be used for determining the unit cells of surface and adsorbed overlayers lattices, and for true quantitative structure determination. The quantitative determination of structure is difficult and computationally intensive. In our work, LEED experiments were performed for structure determination of the surfaces and adsorbed overlayers. This technique involves bombarding the surface with a collimated beam of low energy electrons (20 - 200 eV), the energy of which can be controlled. The diffracted electrons travel away from the sample and towards a phosphor coated fluorescent screen. Of these electrons, only those that are elastically scattered end up reaching the screen to produce a diffraction pattern. The inelastically scattered electrons are filtered by a series of grids placed between the surface and the screen. An important point to note is that LEED can only be used for the determination of ordered surfaces and overlayers. If the sample surface is disordered because the surface is amorphous, polycrystalline or simply contaminated, no diffraction pattern will be obtained as the diffraction of electrons from the surface will be random. Thus, LEED can be used to determine the cleanliness of the sample surface. The schematic for a LEED apparatus is depicted in Figure 2.9.

2.2.2.1 Formation of LEED patterns

From De Broglie's wave-particle duality principle, an incident electron beam can be considered as electron waves incident on the surface. These electrons

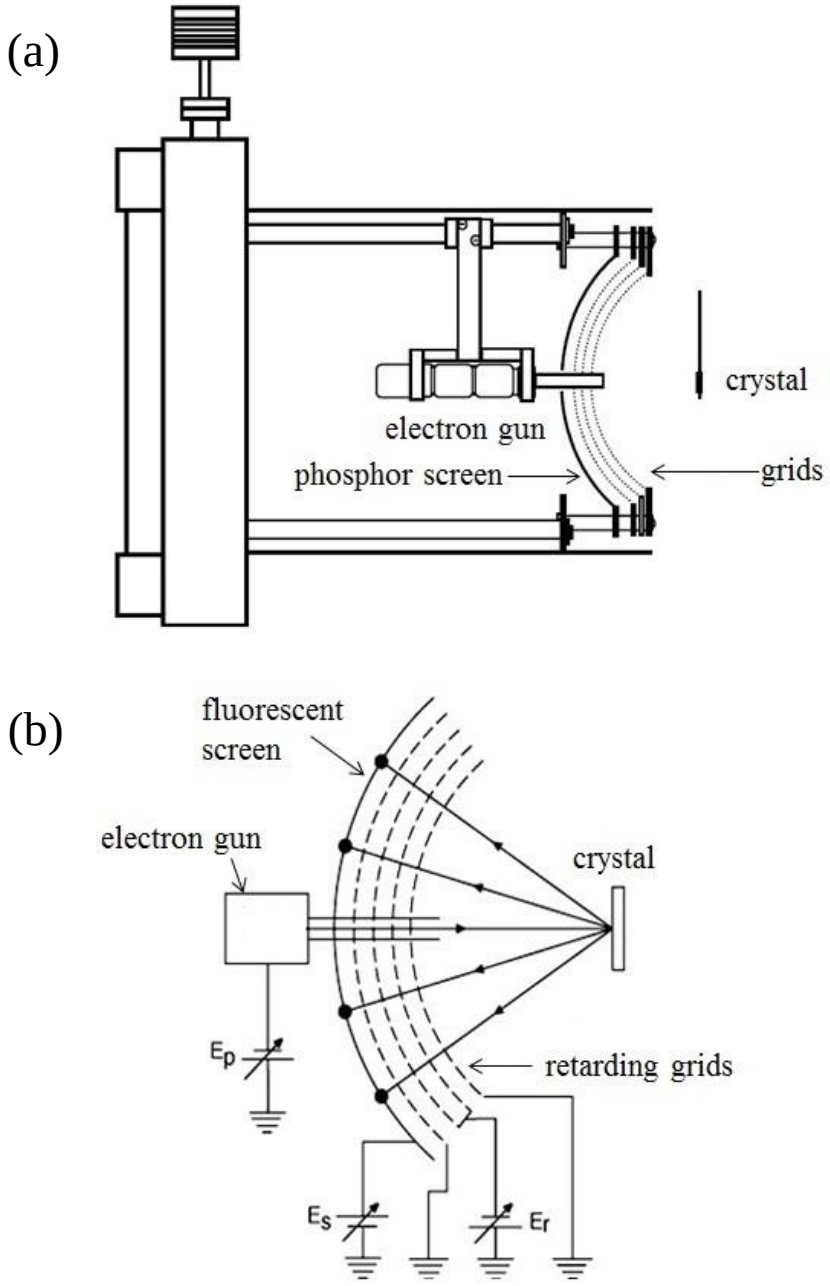

Figure 2.9 a) Schematic diagram of a LEED apparatus which consists of an electron gun, retarding grids and a fluorescent screen. b) Representation of a LEED experiment on a single crystal surface. Low energy electrons scatter off the grounded crystal surface to reach the fluorescent screen and generate diffraction patterns. Only the elastically scattered electrons contribute to the diffraction pattern while the inelastically scattered electrons are filtered out by the middle grids.

are scattered by regions of high localized electron density i.e. surface atoms. The surface atoms can therefore be considered to be point scatterers and the scattered electrons in turn are again waves originating from these point sources. The wavelength 'λ' of these electron 'waves' is given by De Broglie's wavelength equation,

$$\lambda = h/\sqrt{2 \cdot m \cdot e \cdot V} \qquad \text{..... (2.4)}$$

where, h - Planck's constant (J·s); m - mass of electron (kg); e - electronic charge (C); and V - beam voltage (eV). Based on this equation, the wavelength of an electron beam with energy in the range of 20 eV and 200 eV can be calculated to be 0.87 Å and 2.7 Å respectively. This range is comparable with the atomic spacing of the Cu crystals, which is the necessary condition for diffraction to be observed.

Consider a 1D lattice with lattice spacing 'a' as shown in the Figure 2.10 and consider a wave with wavelength 'λ' incident on this lattice with an incident angle θ_0. If we consider the scattering of a wave from two adjacent atoms at an angle θ to the surface normal, then the path difference (d) between the electrons scattered from two adjacent atoms is

$$d = (a \cdot \sin\theta - a \cdot \sin\theta_0) \qquad \text{..... (2.5)}$$

Now, according to Bragg's condition, for complete constructive interference to occur, the path difference must be an integral multiple of the wavelength i.e. $d = (a \cdot \sin\theta - a \cdot \sin\theta_0) = n \cdot \lambda$, where '$n$' is an integer. Therefore, for observing a LEED pattern, this condition must be satisfied when the scattered electrons interfere at the detector. Depending on the wavelength of the incident

electron beam, the diffracted intensity can vary anywhere between zero [i.e destructive interference in which $d = (a \cdot \sin\theta - a \cdot \sin\theta_0) = (n + ½) \cdot \lambda$] and a maximum value [i.e. constructive interference in which $d = (a \cdot \sin\theta - a \cdot \sin\theta_0) = n \cdot \lambda$].

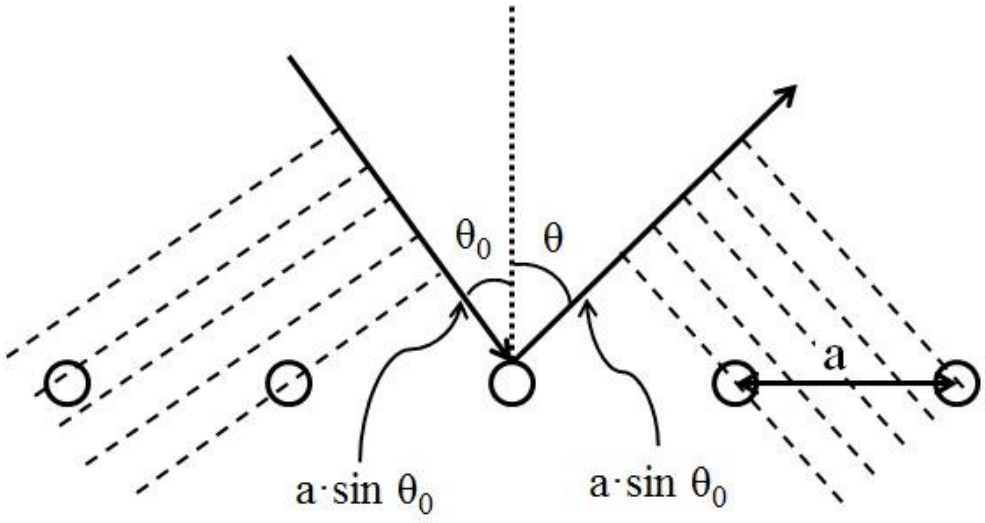

Figure 2.10 Illustration of one-dimensional scattering. An electron beam with a specific wavelength λ is scattered by a line of atoms each separated by distance *a*. Constructive interference occurs if the path difference *d* between adjacent electron beams is an integral multiple of the wavelength i.e. $d = (a \cdot \sin\theta - a \cdot \sin\theta_0) = n \cdot \lambda$. For observing a LEED pattern, this condition must be satisfied when the scattered electrons interfere at the detector.

2.2.2.2 *Interpretation of the LEED pattern*

2.2.2.2.1 Reciprocal Lattice

The LEED pattern observed for any two-dimensional surface lattice is actually an image of the reciprocal lattice and not a direct representation of the real space lattice of the atoms on the surface. For any lattice with vectors $(\vec{a}_1, \vec{a}_2)$ one can define the reciprocal lattice $(\vec{a}_1^*, \cdot\, \vec{a}_2^*)$:

$$\vec{a}_1 \cdot \vec{a}_2^* = \vec{a}_2 \cdot \vec{a}_1^* = 0 \qquad \text{….. (2.6)}$$

$$\vec{a}_1 \cdot \vec{a}_1^* = \vec{a}_2 \cdot \vec{a}_2^* = 1 \qquad \text{….. (2.7)}$$

The reciprocal lattice is periodic and has symmetry just like the real space lattice (Figure 2.11). Interpretation of the LEED pattern requires transforming the image of the reciprocal lattice back into the real lattice based on Equations 2.6 and 2.7.

2.2.2.2.2 Overlayers and Superlattices

Some surfaces can reconstruct such that the periodicity of the surface is different from that of the bulk termination plane. When atoms or molecules are adsorbed on surfaces, they tend to form well defined structures. They will adsorb on well-defined sites on the surface and often with long range order or periodicity which is commensurate with the substrate. The ordered overlayers are lattices of atoms or molecules. Adsorbed atoms also produce ordered overlayers with lattice parameters different from that of the substrate. For example, in Figure 2.12, the relationship between the two lattices can always be given as

$$\vec{b}_1 = m_{11}\vec{a}_1 + m_{12}\vec{a}_2 \qquad \text{….. (2.8)}$$

$$\vec{b}_2 = m_{21}\vec{a}_1 + m_{22}\vec{a}_2 \qquad \text{….. (2.9)}$$

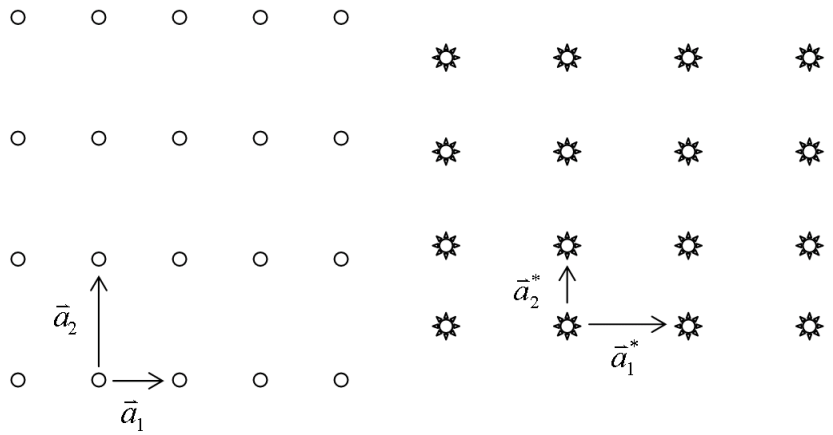

Figure 2.11 The figure illustrates a real space lattice (left section) and its reciprocal lattice (right section). The reciprocal lattice is periodic and has symmetry just like the real space lattice. Interpretation of the LEED pattern requires transforming the image of the reciprocal lattice back into the real lattice based on: $\vec{a}_1 \cdot \vec{a}_2^* = \vec{a}_2 \cdot \vec{a}_1^* = 0$ and $\vec{a}_1 \cdot \vec{a}_1^* = \vec{a}_2 \cdot \vec{a}_2^* = 1$.

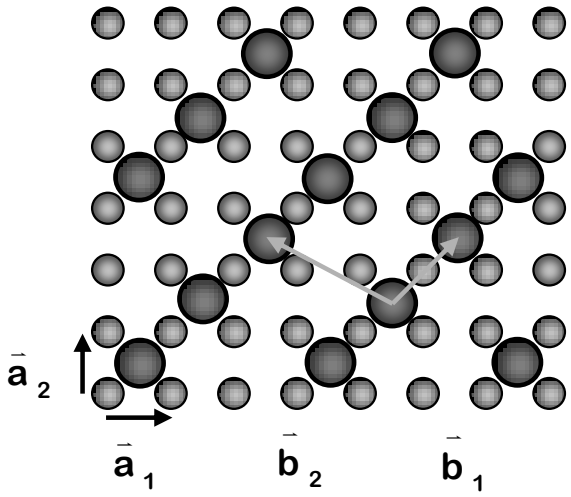

Figure 2.12 The figure represents a real-space substrate lattice with vectors $(\vec{a}_1, \vec{a}_2)$ and an adsorbate lattice with vectors $(\vec{b}_1, \vec{b}_2)$.

The overlayer can then be denoted by a simple matrix which transforms the overlayer lattice into the substrate lattice.

$$\begin{pmatrix}\vec{b}_1\\ \vec{b}_2\end{pmatrix} = \begin{bmatrix}m_{11} & m_{12}\\ m_{21} & m_{22}\end{bmatrix}\begin{pmatrix}\vec{a}_1\\ \vec{a}_2\end{pmatrix} = M\begin{pmatrix}\vec{a}_1\\ \vec{a}_2\end{pmatrix} \qquad \text{….. (2.10)}$$

For example, consider the substrate lattice denoted by vectors $(\vec{a}_1, \vec{a}_2)$ and the overlayer lattice denoted by vectors $(\vec{b}_1, \vec{b}_2)$.

$$\vec{b}_1 = 1 \cdot \vec{a}_1 + 1 \cdot \vec{a}_2 \qquad \text{….. (2.11)}$$

$$\vec{b}_2 = -2 \cdot \vec{a}_1 + 1 \cdot \vec{a}_2 \qquad \text{….. (2.12)}$$

$$M = \begin{bmatrix}1 & 1\\ -2 & 1\end{bmatrix} \qquad \text{….. (2.13)}$$

The LEED pattern of the adsorbate overlayer is also an image of its reciprocal lattice and it is necessary to derive the real space lattice of the overlayer structure from this reciprocal lattice. Similar to Equation 2.5, the overlayer reciprocal lattice vectors $(\vec{b}_1^*, \vec{b}_2^*)$ can be related to those of the substrate vectors $(\vec{a}_1^*, \vec{a}_2^*)$ by:

$$\begin{pmatrix}\vec{b}_1^*\\ \vec{b}_1^*\end{pmatrix} = \begin{bmatrix}m_{11}^* & m_{12}^*\\ m_{21}^* & m_{22}^*\end{bmatrix}\begin{pmatrix}\vec{a}_1^*\\ \vec{a}_1^*\end{pmatrix} = M^*\begin{pmatrix}a_1^*\\ \vec{a}_1^*\end{pmatrix} \qquad \text{….. (2.14)}$$

where M^* is the reciprocal space overlayer matrix from which the real space overlayer matrix, M, can be calculated from the following relationship:

$$M = [(M^*)^t]^{-1} \leftrightarrow M^* = [(M)^t]^{-1} \qquad \text{….. (2.15)}$$

$$M^* = \begin{bmatrix}1/3 & 2/3\\ -1/3 & 1/3\end{bmatrix} \qquad \text{….. (2.16)}$$

2.2.2.3 LEED experimental set-up and procedures

The LEED experiments were primarily conducted in chamber II. This chamber was equipped with an OCI Vacuum Microengineering optics with 77˚ solid angle view and a 75 mm diameter dual microchannel-plate for image intensification. This allowed the LEED patterns to be obtained with an electron beam current of a few nanoamps, thereby minimizing damage to the TA overlayer. Because the microchannel plates and phosphor screen are flat, the reciprocal space image of the LEED pattern is slightly distorted from the true reciprocal lattice that is obtained with a spherical screen. This has not complicated the assignment of the LEED patterns. The LEED experiments were performed with the sample kept normal to the incident electron beam with a beam voltage of 60 – 200 eV. During the experiments, the temperature of the sample was around 100 ± 10 K and the sample was electrically grounded. An example of a LEED pattern obtained from a clean Cu(110) and the corresponding ball model of the surface is shown in Figure. 2.13.

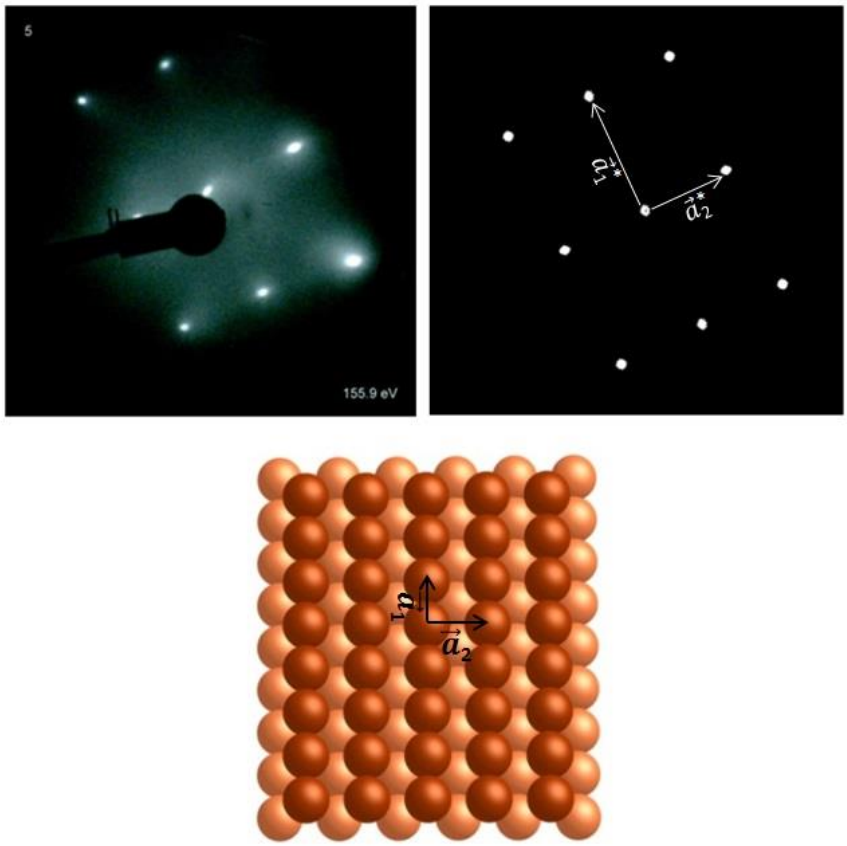

Figure 2.13 Top section**:** LEED pattern obtained from a clean Cu(110) surface (left) with its reciprocal lattice outline and reciprocal lattice vectors ($\vec{a}_1^*, \vec{a}_2^*$). Bottom section: Ball model of a Cu(110) surface representing real space lattice with lattice vectors ($\vec{a}_1, \vec{a}_2$). $\vec{a}_2 = \sqrt{2} \cdot \vec{a}_1$. Therefore, $\vec{a}_1^* = \sqrt{2} \cdot \vec{a}_2^*$.

2.2.3 X-ray photoelectron spectroscopy

X-ray photoelectron spectroscopy (XPS), also known as electron spectroscopy for chemical analysis (ESCA), is the most widely used surface analysis technique because of its relative simplicity in use and data interpretation. The technique is based on Einstein's photoelectron effect and was developed by Kai Siegbahn and his research group at the University of Uppsala, Sweden [92]. Deep core electrons have binding energies corresponding to the energies of photons that lie in the X-ray region [89]. When a solid absorbs a photon with energy (hv) in excess of the binding energy (E_B) of an electron, a photo-electron is emitted and the kinetic energy (E_K) of the photoelectron is related to the energy of the photon by the relation:

$$E_B = hv - E_K \qquad \text{..... (2.17)}$$

Deep core electrons do not participate in bonding and their energies are characteristic of the atom from which they originate. Therefore, XPS is particularly useful for elemental analysis of a sample. XPS spectra are obtained by irradiating a material with a beam of X-rays while simultaneously measuring the kinetic energy and number of electrons that escape from the top 1 to 10 nm of the material being analyzed. The experimentally measured energies of the photoelectrons are given by:

$$E_B = hv - E_K + E_w \qquad \text{..... (2.18)}$$

where, E_w is the work function of the spectrometer. An XPS spectrum is a plot of signal intensity i.e. number of electrons as a function of E_B which is a characteristic of each element. The peak areas can be used (with appropriate

sensitivity factors) to determine the composition of the material's surface. When the energies of core levels are investigated in more detail, it is found that small but easily detected spectral peak shifts do occur. These shifts in binding energies are known as 'chemical shifts' and they are influenced by the chemical environment around the atom. Therefore, chemical shifts can be used to identify the chemical state of the materials being analyzed. XPS is not sensitive to hydrogen or helium, but can detect all other elements. Typically, XPS is used to determine the [89, 92, 93]:

- elemental composition of the surface (top 1–10 nm usually)
- empirical formula of pure materials
- elements that contaminate a surface
- chemical or electronic state of each element in the surface
- uniformity of elemental composition across the top surface (or line profiling or mapping)
- uniformity of elemental composition as a function of ion beam etching (or depth profiling)

The information that XPS provides about surface layers or thin film structures is of value in many industrial applications including: polymer surface modification, catalysis, corrosion, adhesion, semiconductor and dielectric materials, electronics packaging, magnetic media, and thin film coatings [94].

2.2.3.1 XPS apparatus

Figure 2.14 shows the basic elements of an XPS apparatus. X-rays illuminate an area of a sample, causing electrons to be ejected with a range of energies and directions. Al K_α (1486.6eV) or Mg K_α (1253.6eV) are often the photon energies of choice. Other X-ray lines can also be chosen such as Ti K_α (2040eV). The electron analyzer lens assembly, which is a set of electrostatic lens units, collects a proportion of these emitted electrons. The analyzer lens focuses these electrons to the electron analyzer entrance slit while applying a varying retarding field (of energy E_R) that decelerates the photoelectrons thereby reducing their kinetic energy. A hemispherical analyzer is the most common type of analyzer used because of its excellent energy resolution characteristics. Electrostatic fields within the hemispherical analyzer (HSA) are established to allow electrons of a given energy, called the 'pass energy (PE or E_P)' to completely follow the entire curved trajectory and arrive at the detector slits and onto the detector electron multiplier. In the HSA, if the kinetic energy of the electrons (KE or E_k) is more than the set E_P, they will collide with the outer hemisphere. If the $E_k$is too low, they will collide with the inner hemisphere. Thus, only electrons in the narrow energy region (E_P) reach the electron multiplier which records the electron count and E_k at a particular instant. The instantaneous kinetic energy of the electrons as recorded by the detector is given by:

$$E_k = E_P + E_R \qquad \text{..... (2.19)}$$

From 2.18 and 2.19

$$E_B = hv - (E_P + E_R) + E_w \qquad \text{..... (2.20)}$$

By varying the range and step size of E_R i.e. ΔE_R, the electron counts corresponding to a range of binding energies can be collected, which is a typical XPS spectrum (Figure 2.15). ΔE_R and E_P are the key parameters that dictate the resolution of an XPS spectrum.

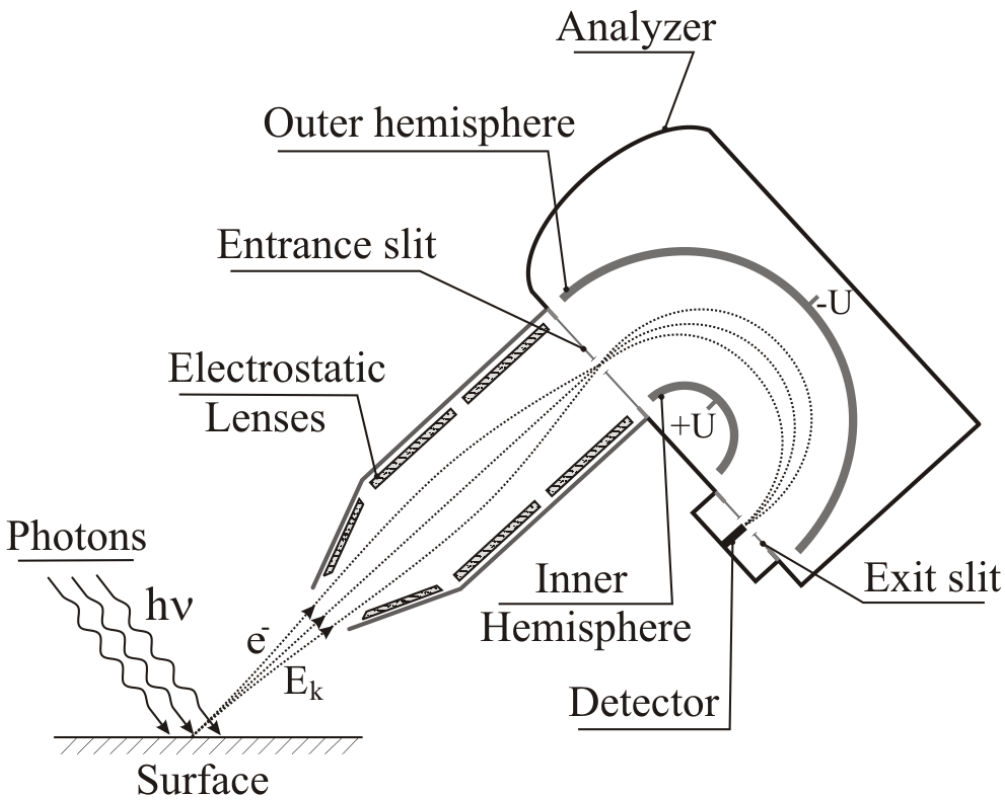

Figure 2.14 Basic elements of an XPS system. The apparatus consists of an X-ray source, an electrostatic lens and an electron analyzer. The binding energy of the ejected photoelectrons is given by $E_B = h\nu - E_K$. The system is capable of determining the number of photo-electrons ejected from the surface corresponding to a particular binding energy.

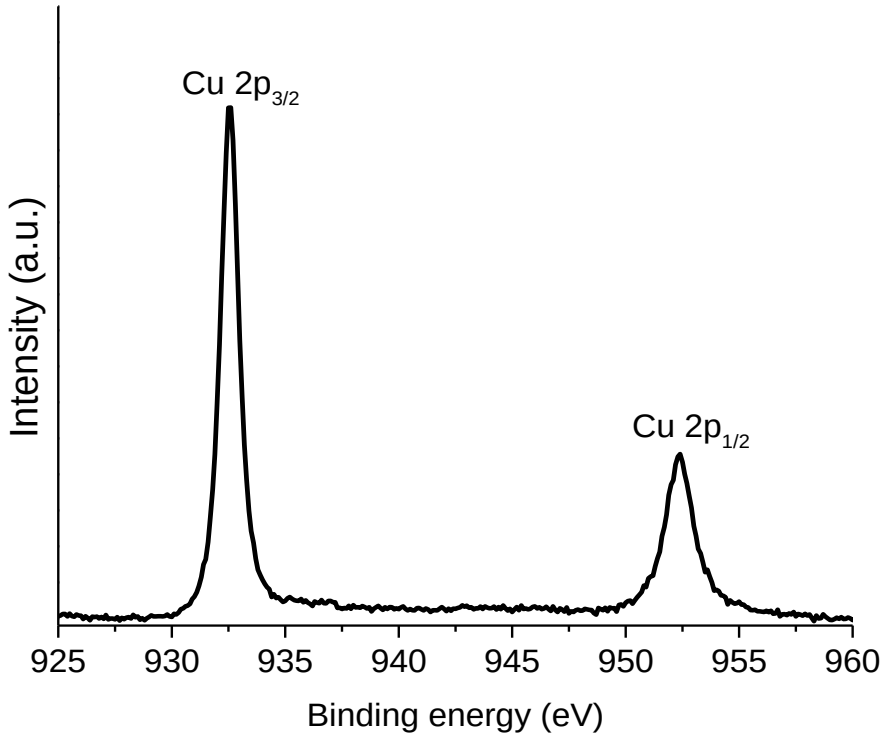

Figure 2.15 A typical XPS spectrum is a plot of number of photo-electrons i.e. intensity as a function of their binding energy E_B . The figure depicts an XPS spectrum obtained for Cu surface while monitoring the intensity of the photo-electron signal as a function of binding energy E_B corresponding to the $2p_{3/2}$ and $2p_{1/2}$ orbitals.

2.2.3.2 XPS experimental set-up and procedures

The TA/Cu(643)$^{R\&S}$ XPS experiments detailed in this thesis were performed in chamber I whereas the Asp/Cu(110) XPS experiments were performed in chamber III (Thetaprobe).

In chamber I, the primary purpose of XPS experiments was to determine the coverage of the adsorbate (TA) on Cu(643)$^{R\&S}$ surfaces. XPS was also used to verify the cleanliness of the surface before every experiment. This chamber was equipped with a 350 mm Single Anode Mg - XR3HP X-ray Source from VG Scientific and an EA 125 hemispherical analyzer with a mean radius of 125 mm and a detector comprising of seven channel electron multipliers (Channeltrons) from Omnicron. The Channeltron amplifies the current of a single electron/ion by a factor of about 10^8. The sample was placed normal to the analyzer lens whereas the X-ray source was oriented at 45˚ w.r.t to the sample normal. The pass energy used during the experiments was E_p = 100 eV. The detailed procedure for determining the surface coverage, along with the relevant calculations is detailed in Appendix 5.1.

In chamber III i.e Thetaprobe, the primary objective of the XPS experiments was to identify the chemical groups present on the surface. XPS was also used to verify the cleanliness of the surface before every experiment. The experimental apparatus consisted of Thermo Scientific MXR1 monochromatic X-ray source and a Thermo Scientific 'Theta' Spectrometer. The pass energy used during the experiments was E_p = 40 eV. Figure 2.15 illustrates a C 1s XPS spectra obtained for a) clean Cu surface and b) Cu surface saturated with L-Asp.

It is evident from the spectrum in Figure 2.16 a that the surface is clean and that there are no carbon impurities initially present on the surface. Similar spectra were obtained to detect O and N impurities. Figure 2.16 b illustrates the C 1s XPs spectrum obtained after dosing the clean surface with L-Asp. Different states of C-atom on the surface i.e. different chemical species present on the surface, can be readily identified after de-convoluting the XPS spectrum. For example, depending upon the positions of the de-convoluted peaks, it can be identified that four carbon-containing species i.e. CH_2, $CH(NH_2)$, COO and COOH are present on the surface. In a similar manner, the chemical states of N and O atoms were also identified to confirm the state of the molecules adsorbed on the surface. This will be discussed in detail in chapter 4.

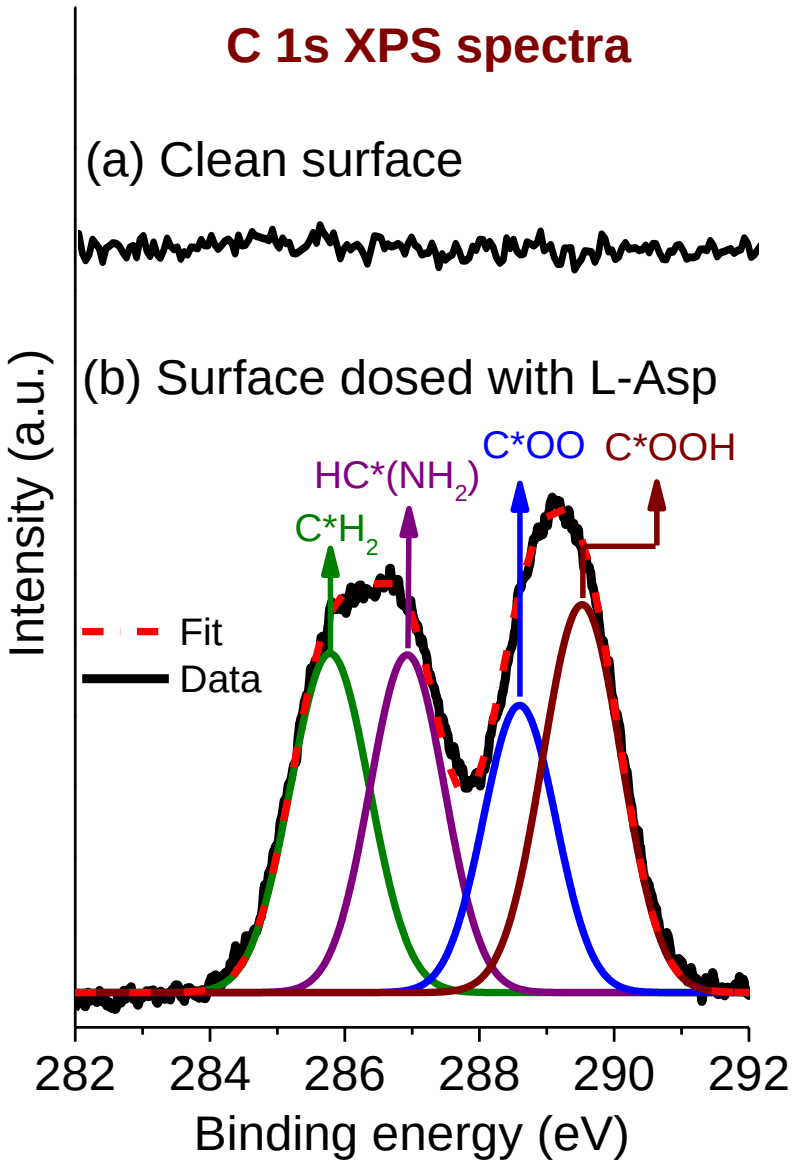

Figure 2.16 C 1s XPS spectra obtained for clean Cu surface and Cu surface saturated with L-Asp. a) C 1s XPS spectrum obtained for a clean surface before dosing it with L-Asp. It is evident from the spectrum that the surface is clean and that there are no carbon impurities initially present on the surface. b) C 1s XPs spectrum obtained after dosing the surface with L-Asp. Different states of C-atom on the surface i.e. different chemical species present on the surface, can be readily identified after de-convoluting the XPS spectrum.

2.3 Materials

2.3.1 Copper single crystals

All experiments detailed in the thesis were performed on Cu (purity 99.999+%) single crystals purchased from a commercial source (Monocrystals Company). Each single crystal disk was ~10 mm in diameter and ~2 mm thick and was sub-micron polished on both the sides. Chambers 1 and 2 permitted mounting only one crystal at a time. In the case of Cu(110),both the crystal faces were of the same orientation and only one side was used for experiments. However, in the case of Cu(hkl)$^{R\&S}$, the two crystal faces expose two surfaces of opposite handedness i.e. one side exposes Cu(hkl)^{R} surface while the other side exposes Cu(hkl)^{S} surface.

The crystals used for experiments in Chambers 1 and 2 were spot welded between two tantalum (Ta) wires (Omega, 99.95 % purity) at the end of a UHV manipulator. The crystal could be heated (resistively) or cooled (using Liq. N_2) over 80 to 1000 K with the temperature measurement being made by a chromel-alumel thermocouple spot welded to the edge of the crystal. In Chamber III, the crystals were mounted on customized sample holders. Two Ta plates were used to press the crystal against the ceramic heater of the sample holder. A soft copper braid was introduced between the crystal and the ceramic heater to ensure uniform contact. The crystal could be cooled to below 300 K by passing cold air from an ice bath, and could be heated upto 900 K with the temperature measurement being made by a nisil-nicrosil thermocouple spot welded to the edge of the crystal.

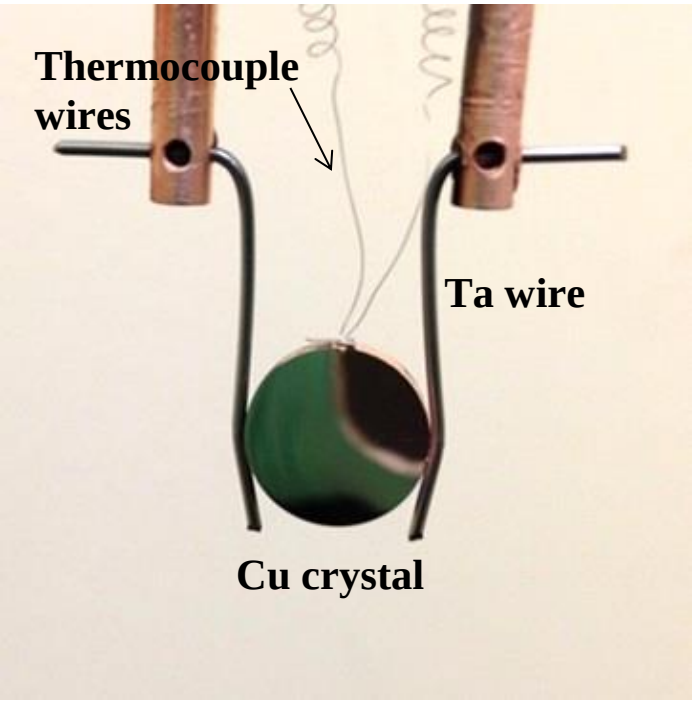

Figure 2.17 Cu(110) single crystal mounting procedure during experiments in chamber I and chamber II.

2.3.2 Chemical reagents

Argon (Matheson, 99.995% purity), oxygen (Matheson, 99.995% purity) and carbon dioxide (Matheson, 99.995% purity) gases were obtained in high pressure lecture bottles. Argon was used for sputtering the sample. Oxygen was used for eliminating carbon impurities on the surface by oxidation at high temperatures (1000 K). Two high-precision leak valves (Varian) were dedicated for introducing argon and O_2. The purity of the gases was verified using the mass spectrometer.

CO_2 and Acetonitrile i.e. C_2H_3N (Fluka, 99.9% purity) were used for obtaining their respective mass spectrums in our UHV system i.e for the determination of the intensity of various signals corresponding to the fragmentation in the mass spectrometer. C_2H_3N was first transferred to clean glass vials and subjected to multiple freeze-pump-thaw cycles to remove impurities before introducing in the chamber using a leak valve.

Crystalline powders of D-TA (Sigma-Aldrich, >99% purity), L-TA (Sigma-Aldrich, >99% purity), meso-TA (Sigma-Aldrich, >98% purity), L-Asp (Sigma-Aldrich, >99% purity), 1-^{13}C L-Asp (Sigma-Aldrich, >99% purity), 1,4-$^{13}C_2$ L-Asp (Cambridge Isotope Laboratories, Inc., >99% purity) were used as received.

2.4 Experimental procedure

Each experimental procedure consisted of 3 main steps: sample preparation, dosing and experimental analysis.

2.4.1 Sample preparation

Before each experiment the Cu single crystal sample was oxidized for 300 secs at 1000 K in presence of 5 x 10^{-10} Torr O_2 to remove surface carbon. The sample was then cleaned through repeated sputter-anneal cycles. The sputtering was carried out with a focused beam of Ar^+ ions of 1.5 keV energy at a sample current of ~10 μA. Sputtering was carried out with crystal at 750 K and each cycle was 900 secs long. After each sputtering step the crystal was cooled down and then annealed at 1000 K for 600 secs. Surface ordering and cleanliness were verified with LEED and XPS.

2.4.2 Dosing

TA (or Asp) was deposited on the surfaces of the single crystals by exposing them to TA (or Asp) vapor emanating from sublimation sources mounted in each of the UHV chambers. These sublimation sources were constructed from glass vials heated by passing electrical current through resistive metal (nickel−chromium or tungsten) wire coiled tightly around the vials. The temperatures of the sources were monitored by chromel-alumel thermocouples placed in direct contact with the vial walls. The TA (or Asp) fluxes incident on the Cu surfaces from the sublimation sources depended on the source temperature (338−358 K) and on the distance between the source and the sample surface. In general, exposure of TA (or Asp) to the surfaces was controlled by the time of exposure to TA (or Asp)

vapor emanating from the source, while the source temperature and the distance to the Cu surfaces were kept fixed. Unless otherwise mentioned the experiments were performed by adsorbing TA (or Asp) on the Cu surfaces at 405 K. This temperature allowed monolayer saturation on the surface without allowing the formation of multilayer. Lower exposure times were used to generate subsaturation coverages.

2.4.3 Experimental analysis

2.4.3.1 TPRS

The sample was then positioned within ~1 mm of the aperture to the mass spectrometer and heated while monitoring the signals at one or more *m/q* ratios. The temperature of the sample was controlled to generate a constant heating rate for normal TPRS, or constant temperature for isothermal TPRS. The detailed procedure including the equipment information for the TPRS experiments has been explained in section 2.2.1.3.

2.4.3.2 LEED

Low energy electron diffraction (LEED) patterns were obtained from the clean and TA modified Cu(110) surfaces held at 90 - 110 K. The LEED experiments were performed with the sample kept normal to the incident electron beam with a beam voltage of 60 – 200 eV. The detailed procedure including the equipment information for the LEED experiments has been explained in section 2.2.2.3.

2.4.3.3 XPS

During XPS experiments performed on chamber I the spectra were obtained from clean and TA modified Cu(110) and Cu(643)$^{R\&S}$ surface with the sample was placed normal to the analyzer lens whereas the X-ray source was oriented at 45˚ w.r.t to the sample normal. The pass energy used during the experiments was E_p = 100 eV. In case of experiments performed on chamber III the spectra were obtained from clean and Asp modified Cu(110) surface with the X-ray source and analyzer lens both oriented at 45˚ w.r.t to the sample normal. The pass energy of E_p = 40 eV used was used during the experiments. The detailed procedure including the equipment information for the XPS experiments has been explained in section 2.2.3.2.

Chapter 3

Investigating the initiation process in surface explosions using Tartaric acid on Cu(110)

3.1 Introduction

As discussed previously in section 1.5.4 one of the most poorly understood aspects of surface explosions is the initiation process. Surface defects are often implicated as initiation sites; although there is no direct evidence that this is indeed the case. Vacancies in adsorbate overlayers could also be formed by thermal fluctuations in local density or some other irreversible process such as adsorbate decomposition or desorption. These are difficult processes to probe and the aim of this section of the thesis is to extend our understanding of the processes that initiate explosive decomposition reactions on surfaces.

3.1.1 Tartaric acid

Tartaric acid (TA, HO_2C-CH(OH)-CH(OH)-CO_2H) undergoes autocatalytic decomposition on the Cu(110) surface and the chemistry of TA on Cu(110) has received significant attention over the past two decades [69, 95-103]. Each molecule of TA has two asymmetric centers, leading to three different isomers, which are denoted D-(2S,3S)-, L-(2R,3R)- and meso-(2R,3S)-TA. L- and D-TA are chiral enantiomers of each other. The naturally occurring form of the acid is L-tartaric acid which is found in many plants, particularly grapes, bananas, and tamarinds. Salts of tartaric acid are known as tartrates. Tartaric acid played an important role in the discovery of chemical chirality. Louis Pasteur in 1847 investigated the shapes of ammonium sodium tartrate crystals, which he

found to be chiral [104]. By manually sorting the differently shaped crystals Pasteur was the first to produce a pure sample of D-TA which is perhaps the first recorded instance of chiral resolution. As discussed earlier, tartaric acid has been successfully implemented as a chiral modifier in heterogeneous enantioselective catalysis for hydrogenation of β-ketoesters and β-diketones [31, 100, 105-110].

The chemistry of tartaric acid studied in this work offers significant insight into the explosion initiation process. Kinetic data are presented for the surface explosion of TA/Cu(110) obtained under a range of conditions including variable initial coverage, variable heating rates and isothermal heating over a range of temperatures.

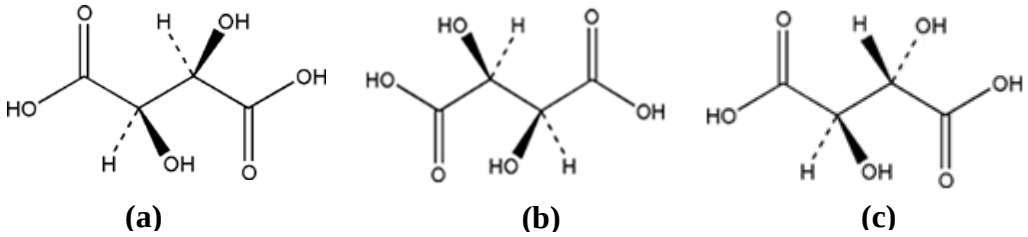

(a) **(b)** **(c)**

Figure 3.1. Structural formulae of the three isomers of tartaric acid, a) meso-(2R,3S)-tartaric acid, b) L-(2R, 3R)-tartaric acid and c) D-(2S,3S)-tartaric acid. The molecules have two chiral centers each.

3.2 Tartaric acid on Cu(110) surface

3.2.1 Adsorption of tartaric acid on Cu(110) at 405 K

The surface chemistry of D- and L-TA on Cu(110) has been documented by Raval *et al.*, Ernst *et al.* and Gellman *et al.* over the past decade [1, 2, 69, 95-103]. At low coverage and ~405 K, adsorbed TA forms a bitartrate (-O_2C-HCOH-HCOH-CO_2-) species that is deprotonated at both ends to form carboxylate moieties that bind to the surface [100]. The adsorbed TA forms ordered overlayer denoted (9,0; -1,2) in the case of D-TA and (9,0; 1,2) in the case of L-TA. These are enantiomorphous overlayers that have been observed using both low energy electron diffraction (LEED) and scanning tunnel microscopy (STM). The (9,0; $\pm$1,2) overlayer lattices have a nominal coverage of [TA] = 1/6 ML (monolayer) relative to the areal density of Cu atoms in the Cu(110) surface. At absolute coverages of [TA] > 1/6 ML the (9,0; $\pm$1,2) overlayer co-exists with a (4,0;2,1) overlayer. The (4,0;2,1) overlayer is formed by a monotartrate (-O_2C-CH(OH)-CH(OH)-CO_2H) species that is deprotonated only at one end and has an absolute coverage of 1 TA molecule per 4 surface Cu atoms (i.e. per unit cell) or 0.25 ML. At absolute coverages of [TA] > 1/4 ML, L-TA forms a densely packed overlayer which has been denoted (4,1; 2,5) and has an absolute coverage of [TA] = 5/18 ML. The coverage assignment was based on work of Ernst *et al.* in which they demonstrate that saturation of the surface monolayer occurs at 0.278 ML in the case of pure TA enantiomers and at 0.25 ML in case of racemic TA [69, 96]. The (4,1; 2,5) overlayer has the saturation absolute coverage of TA on Cu(110) and for purpose of this work will be assigned a fractional coverage of θ^{TA} = 1.

With this definition of fractional coverage, the (4,0; 2,1) overlayer has coverage θ^{TA} = 0.9 and the (9,0; 1,2) overlayer has θ^{TA} = 0.6. To be consistent with the general overlayer notation rules recently proposed by Ernst, we will denote the (4,1; 2,5) overlayer as (4,1; -2,4). Also, since our interest is predominantly in the explosion initiation process, we describe our observations of a ($\pm$6,7; $\mp$2,1) phase that appears to be relevant to explosion initiation process [96].

3.2.2 LEED patterns and STM images of ordered phases of L-TA on Cu(110)

3.2.2.1 (4,1; -2,4) overlayer

At saturation coverage, L-TA is adsorbed as a monotartrate species on the Cu(110) surface and in a (4,1; -2,4) overlayer with an absolute coverage of θ^{TA}= 0.278 ML. The LEED pattern and reciprocal space lattice vectors (inset) for the (4,1; -2,4) overlayer formed by L-TA/Cu(110) are shown in the left hand panel of Figure 3.2 A. The real space lattice is shown in the middle panel of Figure 3.2 A. The STM image is shown in the right hand panel of Figure 3.2 A.

3.2.2.2 (4,0; 2,1) overlayer

At an absolute coverage of θ^{TA}= 0.25 ML, L-TA is adsorbed as a monotartrate species on the Cu(110) surface and in a (4,0; 2,1) lattice. The LEED pattern and reciprocal space lattice vectors (inset) for the (4,0; 2,1) overlayer formed by L-TA/Cu(110) are shown in the left hand panel of Figure 3.2 B. The real space lattice is shown in the middle panel of Figure 3.2 B. The STM image is shown in the right hand panel of Figure 3.2 B.

3.2.2.3 (6,7; -2,1) overlayer

A Cu(110) surface with the (4,0; 2,1) phase of L-TA was heated at β = 1 K/s to 483 K, just below the explosion temperature and then quenched. This resulted in the formation of the (6,7; -2,1) overlayer with the LEED pattern and reciprocal space lattice (inset) displayed in the left hand panel of Figure 3.2 C. The real space lattice is shown in the middle panel of Figure 3.2 C. This overlayer is not reported in previous studies by Raval *et al.* and Ernst *et al.*, but appears to be relevant to the onset of the explosion reaction. XPS spectra taken before and after the annealing to 483 K indicate ~5% reduction in the coverage of adsorbed TA. The right hand panel of Figure 3.2 C shows an STM image of this overlayer. It is clearly quite unlike any other STM image of this surface in that it reveals the presence of rows of Cu adatoms, presumably extracted from the Cu(110) plane to reside on the surface. Although the contrast in this image does not reveal them, there are features between the rows on Cu adatoms that can be observed under other imaging conditions and arise from TA molecules on the surface.

3.2.3 Explosive decomposition kinetics for TA/Cu(110)

The decomposition of TA on the Cu(110) surface during TPRS exhibits two signature phenomena of an explosive reaction mechanism: occurrence of the reaction over a very narrow temperature range, and a peak reaction rate that shifts to higher temperature with increasing initial TA coverage. Figure 3.3 shows a series of TPR spectra, monitored for CO_2 desorption, for TA decomposition during heating at 1 K/s and using initial coverage, $\theta_0^{TA} = 0.18 - 1$. These experiments were performed by a previous group member, Vladimir Pushkarev. It

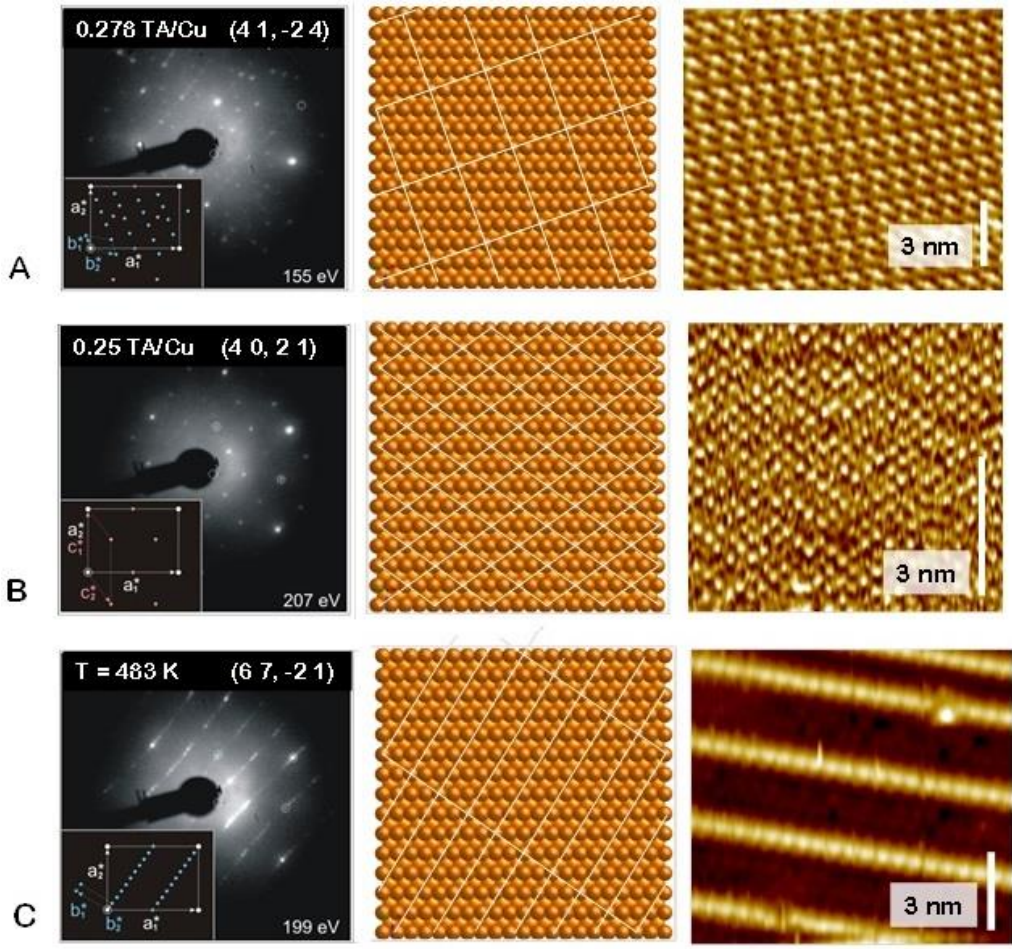

Figure 3.2 LEED (left panels), real space representations of the unit cell (middle panels) and STM images (right panels) of the A) (4,1; -2,4), B) (4,0; 2,1) and C) (6,7; -2,1) overlayers formed at high coverages of L-TA on Cu(110). LEED experiments were performed by Pushkarev and the LEED images are adopted from his thesis. STM experiments were performed by members of Sykes group at Department of Chemistry, Tufts University.

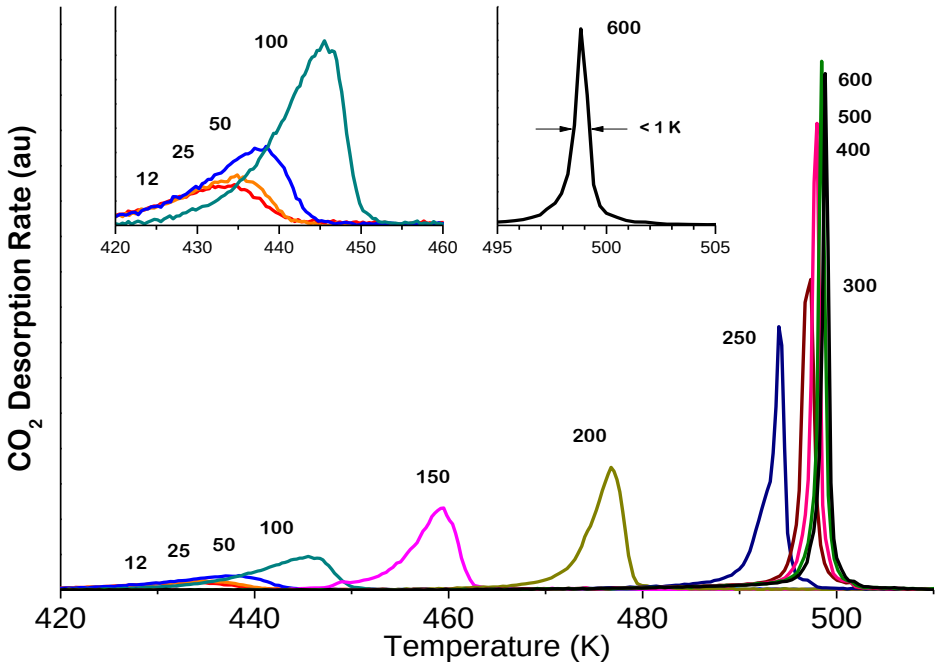

Figure 3.3 TPR spectra of D-TA decomposition on Cu(110) monitored for CO_2 desorption, following increasing exposures to D-TA vapor. The exposure times are labeled with each TPD spectrum. The left-hand inset shows the low coverage decomposition spectra with T_p at ~435 - 445 K. The right-hand inset shows saturation coverage TPR spectrum with a T_p at 499 K and a peak width at half maximum of ΔT_{FWHM} < 1 K. The heating rate in all cases was β = 1 K/s. TA/Cu(110) variable coverage experiments were performed by Pushkarev and this figure is adopted from his thesis.

is evident from the figure that the peaks shift from 432 K to 499 K as the initial TA coverage is increased from $\theta_0^{TA} = 0.18 - 1$. This is a clear indication that at a given temperature, the initial rate is decreasing with increasing initial coverage, i.e. the adsorbate is being stabilized with increasing initial coverage. At saturation coverage i.e. θ_0^{TA} = 1, the peak width has a value of $\Delta T_{FWHM} < 1\ K$. In order to gain further insight into the decomposition kinetics of TA/Cu(110), Pushkarev also conducted TPRS experiments at $\theta_0^{TA} = 1$ using heating rates in the range $\beta = 0.25 - 4.0\ K/s$ as illustrated in the Figure 3.4. As expected, the value of T_p increases with heating rate.

For an explosive decomposition process the isothermal rate must increase with the extent of reaction. Prior studies of surface explosions have used isothermal TPRS to reveal the increase in rate with extent of reaction. Figure 3.5 shows isothermal TPRS of TA decomposition on Cu(110) at temperatures in the range 440 – 470 K. The isothermal condition was achieved by heating the Cu(110) sample to the desired temperature, T_{iso}, at 1 K/s and then holding it at a constant set point. The temperature ramp had an overshoot of < 1K and a settling time of ~10 s (Figure 3.6). Let us consider the TPR spectra at T_{iso} = 440 K, in which we see an initiation period of >400 s during which there is no detectable CO_2 desorption. After 400 s at T_{iso} = 440 K the rate of TA decomposition starts increasing until it reaches a maxima at ~500 s and then drops to zero as TA is consumed. The initiation time decreases with increasing temperature and approaches zero as the temperature tends towards 499 K, the value of T_p observed during TPRS at heating rate of β = 1 K/s. At T_{iso} = 470 K we can see CO_2

desorption at the point of reaching constant temperature and so, we have not collected data for T_{iso} > 470 K. These isothermal data are clear evidence of autocatalytic or explosive decomposition of TA on Cu(110).

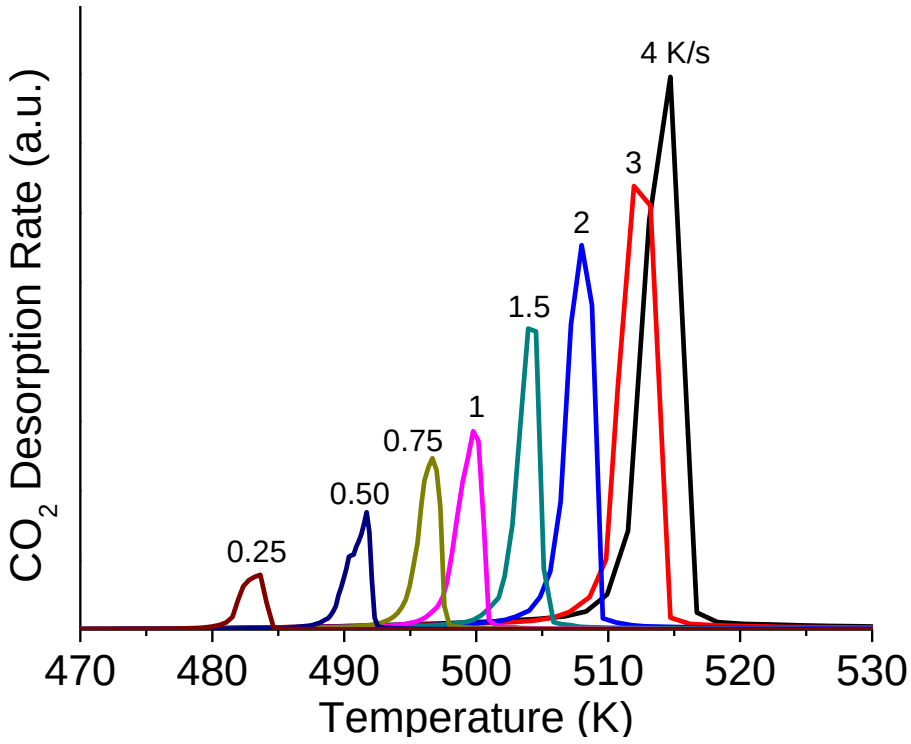

Figure 3.4 TPR spectra of CO_2 produced by decomposition of D-TA on Cu(110) at various heating rates for saturation surface coverage of D-TA. The heating rates are labeled with each TPR spectrum. TA/Cu(110) variable heating rate experiments were performed by Pushkarev and this figure is adopted from his thesis.

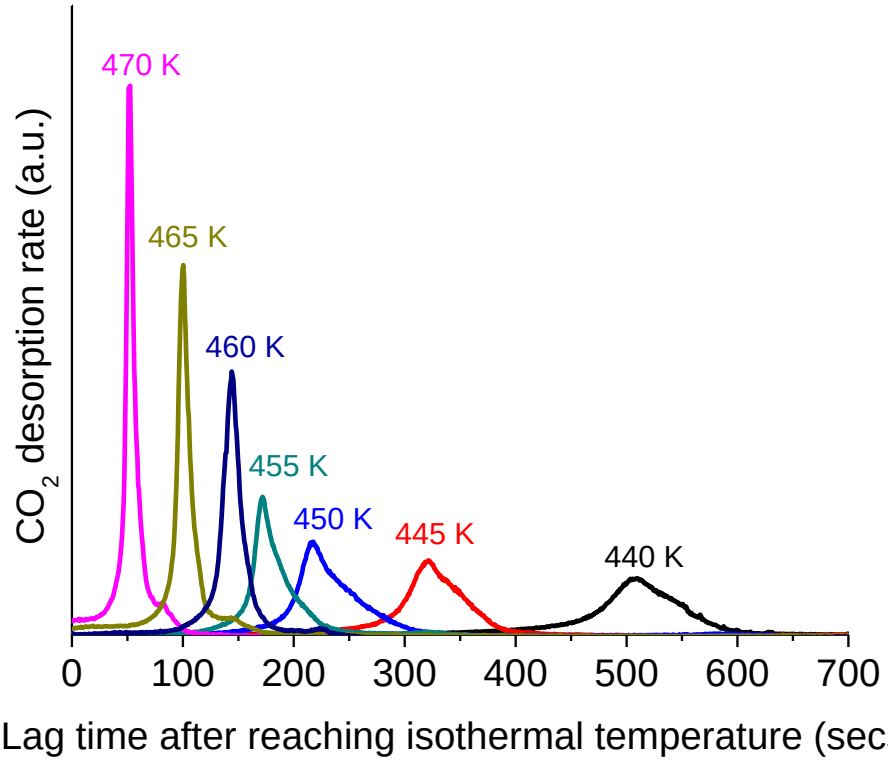

Figure 3.5 TPR spectra of CO_2 produced by decomposition of D-TA on Cu(110) at various isothermal temperatures T_{iso} for saturation surface coverage of D-TA. The isothermal temperatures are labeled with each TPR spectrum.

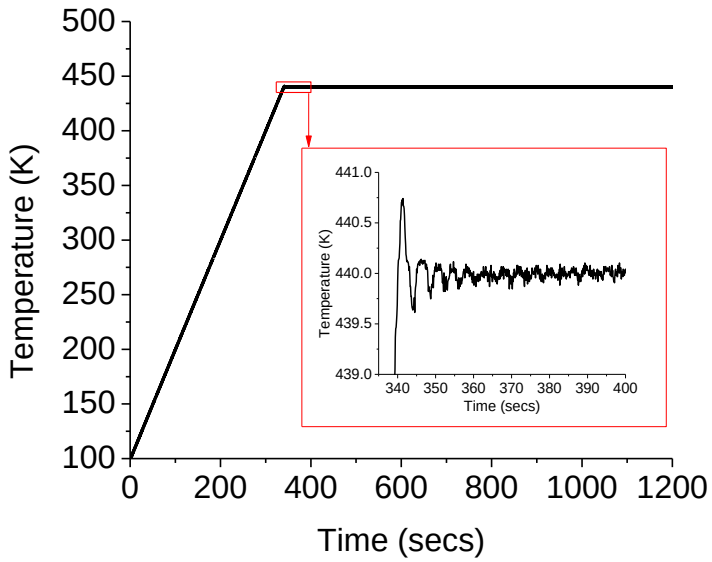

Figure 3.6 Typical temperature ramp during isothermal experiments. The isothermal condition was achieved by heating the Cu (110) sample to the desired temperature, T_{iso}, at 1 K/s and then holding it steady at a constant set point, T_{iso} = 440 K in this case. The temperature ramp had an overshoot of < 1 K and a settling time of ~ 10 s.

3.2.3.1 Multi-mass isothermal TPRS

The isothermal TPRS experiments are well suited to identifying the products of TA decomposition on the Cu(110) surface. Isothermal TPR spectra have been used to monitor desorption signals at *m/q* = 2, 12-18, 25-33, 41-46 and 58, as illustrated in Figure 3.7. These reveal that the major products of decomposition are CO_2, H_2, and H_2O plus several small hydrocarbons consisting primarily of methanol (CH_3OH), formaldehyde (HCOH), ethanol (CH_3CH_2OH) and acetaldehyde (CH_3COH). All species desorb with the same time profiles except that there is some desorption of H_2 prior to desorption of other products. This suggests that the TA decomposition mechanism is one in which the adsorbed monotartrate is first deprotonated to form the bitartrate. Subsequent cleavage of a C-CO_2 bond to yield CO_2 may then be the rate limiting step that leads to rapid fragmentation and product desorption.

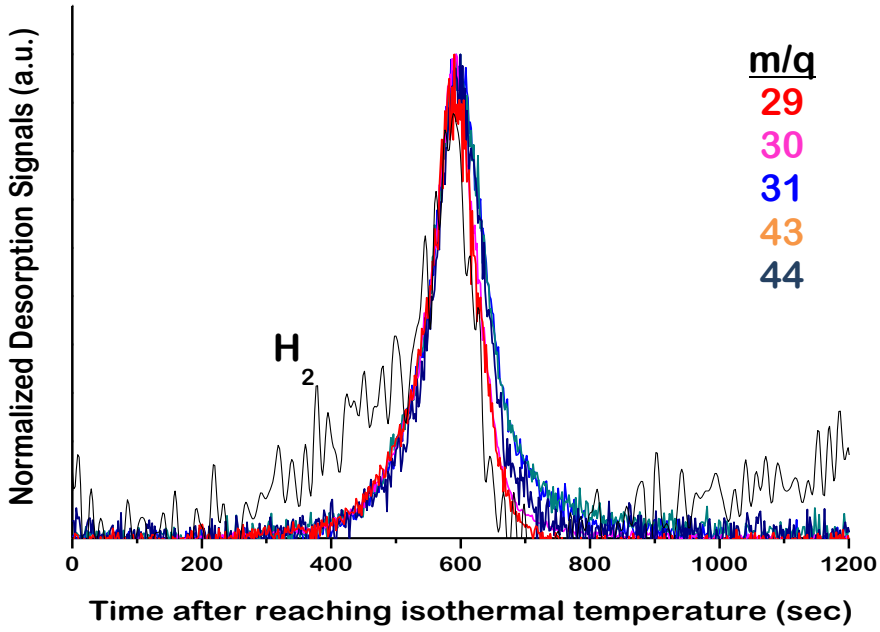

Figure 3.7 Multimass isothermal decomposition spectrum of D-TA/Cu(110) at 440 K. The surface is initially saturated with the monotartrate species. The figure show a subset of the desorption signals obtained at 24 different *m/q* ratios. The desorption of H_2 precedes the explosive decomposition of the monotartrate species. All other decomposition fragments desorb into the gas phase with the same rate limiting step, as indicated by the overlapping leading edges.

3.2.3.2 Initiation sites on the surface

In order to explore the characteristics of the explosion nucleation process, we compare the decomposition of TA on Cu(110) and on Cu(651)^S. The ideal structure of the Cu(651)^S surface is shown in Figure 3.8. It is vicinal to the (110) plane and thus, has (110) terraces that are separated by kinked step edges. Note, that the Cu(651)^S surface has a chiral structure, hence the denotation 'S'. As a consequence, the kinetics of L-TA decomposition can depend on the relative handedness of the adsorbate and the surface; however, enantiospecific explosions will be discussed in chapter 5 of the thesis and are not relevant to the primary point of this chapter.

The initial objective of our study of L-TA decomposition kinetics on Cu(651)^S is to determine whether or not the explosive decomposition of TA can occur on such a highly defected surface. As mentioned earlier, prior studies of surface explosions have suggested that defects on surfaces may be responsible for initiation of surface explosions, however, the nature of the defect has never been clearly defined [62, 76, 97]. If the defect initiation sites are structural features such as steps or kinks, it is not obvious that a surface such as Cu(651)^S with kinks and steps spaced by molecular dimensions would induce explosive decomposition of adsorbed TA. In other words, there are almost as many defects for initiation as TA molecules to undergo explosion. Nonetheless, L-TA does exhibit explosive decomposition kinetics on the Cu(651)^S surface that are quite similar to those observed on the Cu(110) surface. The upper section of Figure 3.8 illustrates an isothermal TPRS of L-TA/Cu(651)^S at 450 K and starting with $\theta_0^{TA} = 1$. The

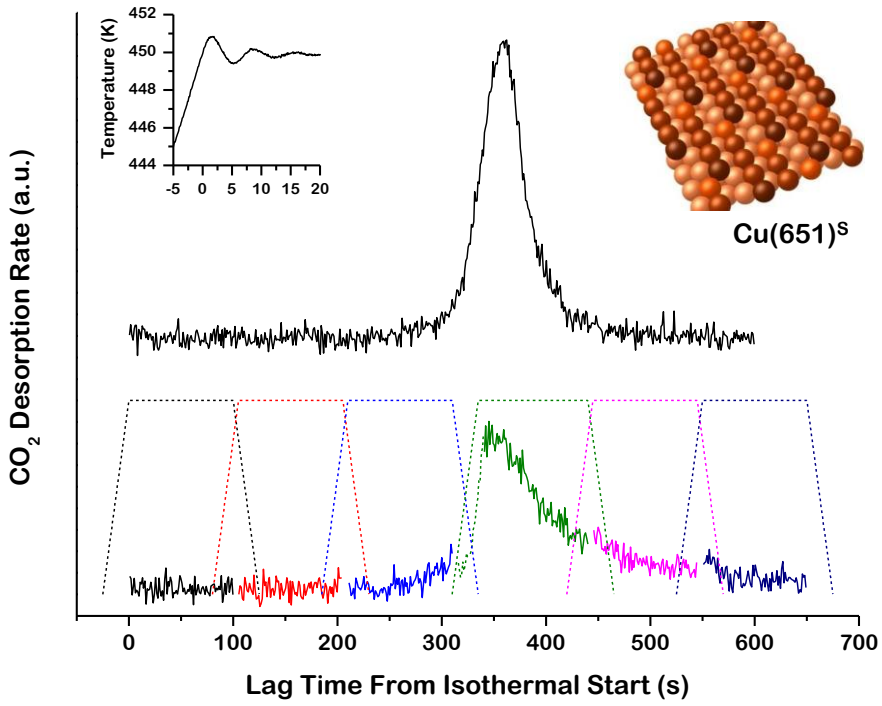

Figure 3.8 Isothermal TPR spectra of saturated L-TA (i.e. $\theta_0^{TA} = 1$) on Cu(651)^S at 450 K. The inset shows the temperature ramp during heating and the stabilization at 450 K. The upper trace (offset for clarity) is an experiment in which the temperature was held at 450 K for 600 s. The explosive decomposition is much like that observed on Cu(110). The lower trace shows six desorption spectra obtained by holding the surface at 450 K for 100 s and then cooling (at β = -1 K/s) for 100 s before starting another temperature ramp. The spectra have been stitched together such that the overall spectra only represents the signals and the time when the crystal was at 450 K. L-TA/Cu(651)^S experiments were performed by Holsclaw and this figure is adopted from his thesis.

insert is a plot of the temperature profile as the set point changes from a heating rate of β = 1 K/s to a constant T_{iso} = 450 K. The TPRS shows an initiation period of ~300 s followed by explosive decomposition and the complete consumption of the L-TA by ~400 s. The induction periods are comparable on the Cu(651)^S and Cu(110) surfaces at 450 K, although it should be pointed out that the two isothermal experiments were done in two different chambers (Cu(110) was conducted in chamber I while Cu(651)^S study was conducted in chamber II) and the temperature measurements may not be reproduced exactly between the two. Nonetheless, the explosive decomposition occurs on Cu(651)^S and the implication is that defects in surface structure are not responsible for initiation of the explosion.

3.2.3.3 Irreversible initiation process

The explosion initiation process that is occurring during the isothermal induction period is not accompanied by detectable desorption of CO_2. At this point one can ask whether the process is reversible or not ? The bottom section of Figure 3.8 represents the TPR spectra from an experiment in which the L-TA/Cu(651)^S surface was quenched intermittently during the anneal at 450 K. In this experiment the Cu(651)^S surface saturated with L-TA was repeatedly heated to 450 K at 1 K/s, held at 450 K for 100 s and then cooled to 300 K. The dashed lines indicate the temperature profiles, but stitched together so that the beginning and end of the consecutive isothermal anneal periods are aligned. The TPRS trace shows the CO_2 desorption signals obtained only while the sample was at 450 K. During the first three 100 s periods there is no detectable CO_2 desorption until the

very end of the third period. During the fourth heating cycle there is clearly observable desorption of CO_2 that reaches a maximum and then decays during heating at 450 K. A residual amount of CO_2 desorbs during the fifth cycle and almost none during the sixth. The point clearly illustrated by the data in Figure 3.8 is that the initiation process is irreversible. In spite of the interrupted heating profile, the explosive decomposition of L-TA/Cu(651)^S still occurs between 300 and 400 s of annealing at 450 K.

3.2.3.4 Isothermal STM during initiation and explosion of TA/Cu(110)

The initiation-explosion behavior of TA/Cu(110) creates an unusual opportunity to monitor the slow changes occurring on the surface during isothermal heating and leading to the explosive decomposition reaction. Furthermore, the data illustrated in Figure 3.8 indicates that quenching the sample temperature during isothermal heating, does not significantly perturb the initiation and explosion kinetics. As a consequence, it has been possible to study the initiation process with STM by annealing the TA/Cu(110) at 440 K and quenching the temperature to 300 K after every 50 s of isothermal annealing. The temperature measurement on the STM is probably not as accurate as in the TPRS apparatus but the reaction initiation time observed in the STM suggests that the temperature corresponds roughly to the TPRS spectrum observed at 440 K in the TPRS apparatus. Figure 3.9 shows an isothermal TPR spectrum obtained in the TPRS chamber with the TA/Cu(110) at 440 K. Also shown are a number of STM images of the TA/Cu(110) surface (heated to 440 K in the STM chamber) obtained by quenching at various times throughout the initiation and explosive decomposition process.

To conduct these experiments, the TA/Cu(110) surface was saturated at 405 K with an initial coverage of $\theta_0^{TA} = 1$. The STM image at $t = 0$ s clearly shows the ordered (4,1; -2,4) phase. At $t = 50$ s there is some evidence of disordered regions in the (4,1; -2,4) phase that appear to grow from the step edge running vertically through the image. At $t = 100$ s, there is further evidence of the disordered region and it appears to grow predominantly from the top of the step

edge onto the terrace. At t = 150 s, the surface is clearly covered with domains of both the (4,1; -2,4) and the (4,0; 2,1) phase. The (4,0; 2,1) domains grow across the terraces from the step edge. Note that the local coverage in the (4,0; 2,1) phase is θ^{TA} = 0.90 relative to the local coverage of θ^{TA} = 1 in the saturated (4,1; -2,4) phase. This means that there has been a global decrease in the coverage of adsorbed L-TA but with no detectable CO_2 desorption. At t = 300 s with the onset of measureable CO_2 desorption one observes the appearance of the rows of Cu adatoms that have been extracted from the Cu(110) surface. At t = 400 s the rows of Cu atoms are order into the (6,7; -2,1) structure. The explosive decomposition then accelerates and by t = 500 s the surface is clean and free of adsorbed L-TA.

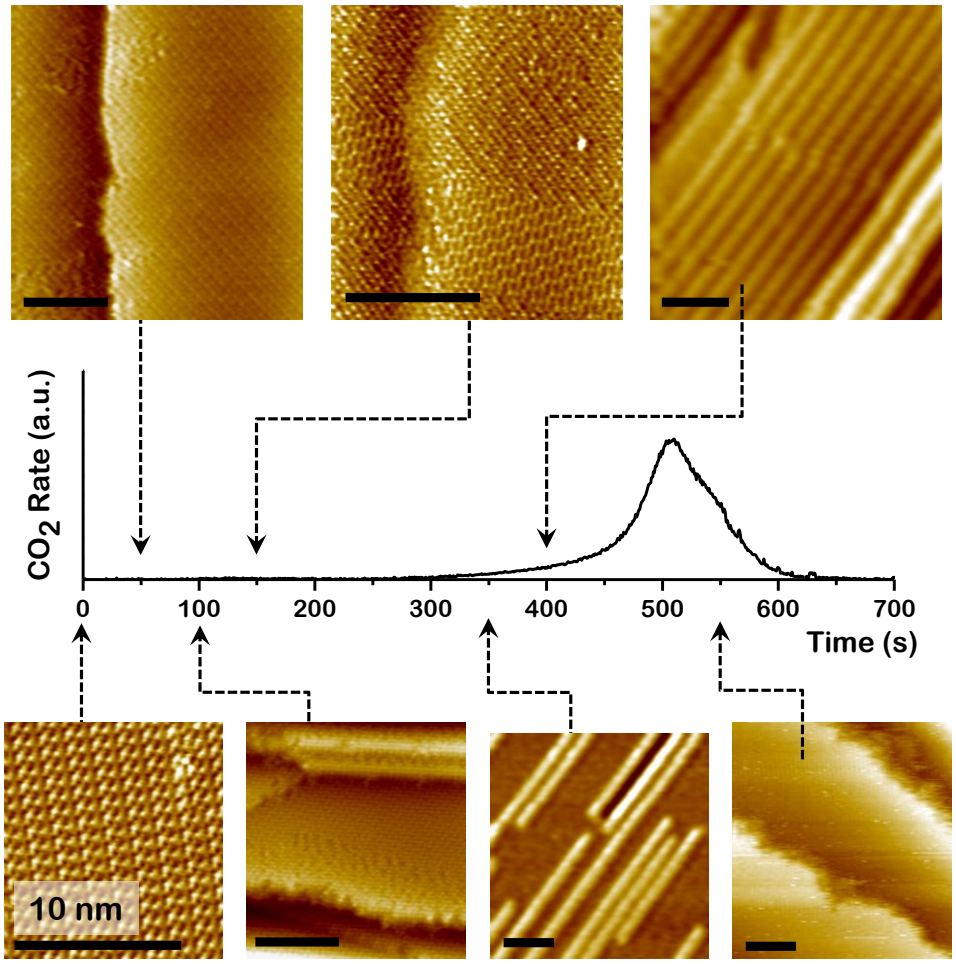

Figure 3.9 Isothermal TPR spectrum of TA on Cu(110) at 450 K with accompanying STM images of the surface. Initial coverage of L-TA was $\theta_0^{TA} = 1$. The STM images were obtained by stopping the heating after every 50 s interval and cooling to room temperature. The surface starts in the (4,1; -2,4) phase at saturation coverage. The (4,0; 2,1) phase begins to appear after 50 s and is readily apparent after 150 s, however there is no detectable CO_2 desorption. The onset of detectable CO_2 desorption is accompanied by the formation of the (6,7; -2,1) phase which dominates during the explosive decomposition. STM experiments were performed by members of Sykes group at Department of Chemistry, Tufts University.

3.2.3.5 Isothermal LEED during initiation and explosion of D-TA/Cu(110)

In addition to STM, LEED was used to monitor the changes on the surface occurring during isothermal annealing of D-TA/Cu(110). Figure 3.10 shows a set of LEED patterns and an isothermal TPR spectrum obtained from a saturated layer of D-TA/Cu(110) annealed at 440 K but with periodic interruption of the annealing every 100 s to cool the sample and obtain a LEED pattern. The interrupted TPR spectrum is analogous to that obtained from $Cu(651)^S$ (Figure 3.8) and reveals the irreversibility of the explosion initiation process on Cu(110). Although the isothermal TPR spectrum taken in the LEED chamber has much lower signal to noise than that obtained in the TPRS chamber (Figure 3.5), it is more than sufficient to observe the explosion reaction.

The key point about the data in Figure 3.10 is that there is a direct link between the timescale for the evolution of the LEED patterns and the TPR spectrum because they were obtained from the same D-TA/Cu(110) sample during one experiment. Before annealing at 440 K the surface exhibits the (-4,1; 2,4) LEED pattern associated with the saturated layer of TA/Cu(110). After heating at 440 K for 100 and 200 s the surface exhibits the LEED pattern of the (4,0; 2,1) overlayer. After annealing for 300 s, just prior to the onset of the explosion reaction, the appearance of the (-6,7; 2,1) pattern is observed. The (-6,7; 2,1) pattern is well developed after 400 s at the peak of the reaction rate. After 500 s and the completion of the reaction, the (1,0; 0,1) pattern of the clean Cu(110) surface is observed. This temporal evolution of the LEED patterns in Figure 3.10 is consistent with the evolution of the STM images shown in Figure

3.9 and reveals the nature of the irreversible changes to the surface occurring prior to the onset of observable CO_2 desorption.

Clearly, the initiation process is one in which there is a net decrease in the coverage of adsorbed TA, and an increase in the areal vacancy concentration, as revealed by the conversion from the ($\pm$4,1; $\mp$2,4) phase to the (4,0; 2,1) phase. Whether this is due to the decomposition of adsorbed TA, molecular desorption or some other irreversible process is not clear. While we cannot detect desorption of CO_2 during the early parts of the initiation period, it may simply be that the rate of decomposition over the long time period of the initiation process is simply too low to be detected. The onset of the detectable CO_2 desorption is accompanied by the appearance of the ($\pm$6,7; $\mp$2,1) phase, although the cause-effect relationship is unclear.

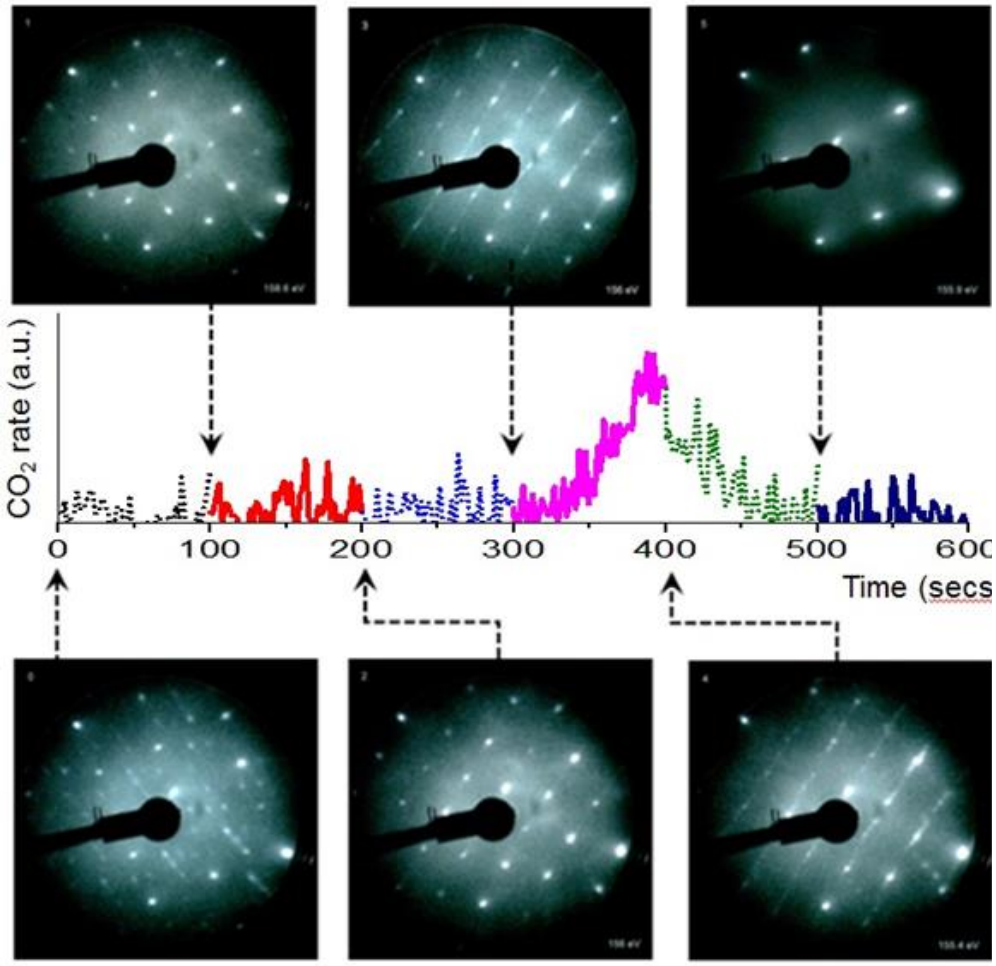

Figure 3.10. TPRS and LEED patterns obtained during isothermal annealing of the D-TA/Cu(110) surface at 440 K. The sample temperature was quenched every 100 s to obtain the LEED pattern. The TPR spectrum is only plotted for the time with the sample at 440 K. The LEED images evolve with time from (-4,1; 2,4) to (4,0; 2,1) to (-6,7; 2,1) and finally the (1,0; 0,1) pattern.

3.2.4 Surface Explosion Kinetics

Most previous efforts to model the kinetics of vacancy mediated surface explosion reactions have used rate laws such as eqn. 1.1 - 1.3 in chapter 1 to model the results of TPRS experiments. [62, 66, 67, 76, 77, 85, 87, 88] As mentioned, the initiation process has not been well-defined in many of these models, largely, because there has been little firm basis for choosing between postulated initiation processes. We have obtained a fairly comprehensive set of kinetic data for TA decomposition on Cu(110) and gained some insight into the nature of the initiation process. On the basis of this insight, we have chosen to model our TPR spectra using a rate expression that explicitly represents the initiation process as a reaction step that creates vacancies via consumption of adsorbed TA,

$$r = k_i\theta^{TA} + k_e\theta^{TA}(1-\theta^{TA})^n \qquad \text{….. (3.1)}$$

where k_i is a rate constant for the initiation process, k_e is the rate constant for the explosion and n defines the order of the explosion reaction with respect to the vacancy concentration. By using this expression to simulate the CO_2 TPR spectra, we are explicitly assuming that the initiation process generates CO_2 in addition to creating vacancies. The use of the rate law expressed in eqn. 3.1 explicitly accounts for the irreversible initiation process by introducing a new parameter, k_i, that must be estimated from the kinetic data but at the same time eliminates any assumption about initiation site density; denoted by the parameter f in previous models [111-113].

The TPR spectra illustrated in Figure 3.11 have been simulated using the rate expression of eqn. 3.1 and used to estimate the activation energies and pre-exponential factors that determine the two rates constants: A_i, E_i, A_e, and E_e. The predicted spectra are shown in the top row of Figure 3.11 for comparison with the measurements (Figures 3.3-3.5) illustrated in the bottom row. The values of the parameters derived from this process are listed in Table 1. The parameter estimation approach has searched for the values of $ln(A_i)$, E_i, $ln(A_e)$, and E_e that minimize the differences between the predicted and measured values of T_p for the TPR spectra and the predicted and measured values of the peak times, t_p, for the isothermal decomposition reactions. Note first that the parameter estimation process restricted the values of the reaction order in vacancy concentration to $n = {}^{1}/_{2}$, 1, or 2 and identified the optimal reaction order of $n = 2$. This suggests that two vacancies are needed for TA dissociation. It is worth noting that reaction orders of $n = {}^{1}/_{2}$ or 1 cannot come close to predicting the range of temperatures spanned by the coverage dependent TPR spectra shown in Figures 3.3. Given the presence of multiple phases, changing coverages and multiple parallel processes, it is not surprising that rate expression of eqn. 3.1 is incapable of reproducing all of the kinetic data exactly. In some respects it is remarkable that it does as well as it does. One question is, whether these multiple phases are critical to the overall process. The fact that one can observe very much the same type of initiation and explosion kinetics on the Cu(651)^{S} surface suggests that the exact nature of the different phases of adsorbed TA on Cu(110) are not significant to the overall process or its kinetics. What is critical is the initial decrease in coverage cause by

an initiation step, followed by the onset of the autocatalytic explosion. The ($\pm$4,1; $\mp$2,4), (4,0; 2,1) and ($\pm$6,7; $\mp$2,1) phases merely provide a convenient way to monitor the time dependent changes occurring on the surface during initiation.

Table 3.1. Kinetic parameters estimated* for the explosive decomposition of TA/Cu(110) using eq. 4 with $n = 2$.

	A (1/sec)	E (kJ/mole)
Initiation, k_i	3.7×10^3	63
Explosion, k_e	6.1×10^{13}	125

* Parameter estimation by minimization of $\sum \left(x_{expt} - x_{model}\right)^2 / x_{expt}^2$ where x are the peak temperatures and the peak times for the variable coverage, variable heating rate and isothermal heating rate TPRS data in Figures 3.3-3.5.

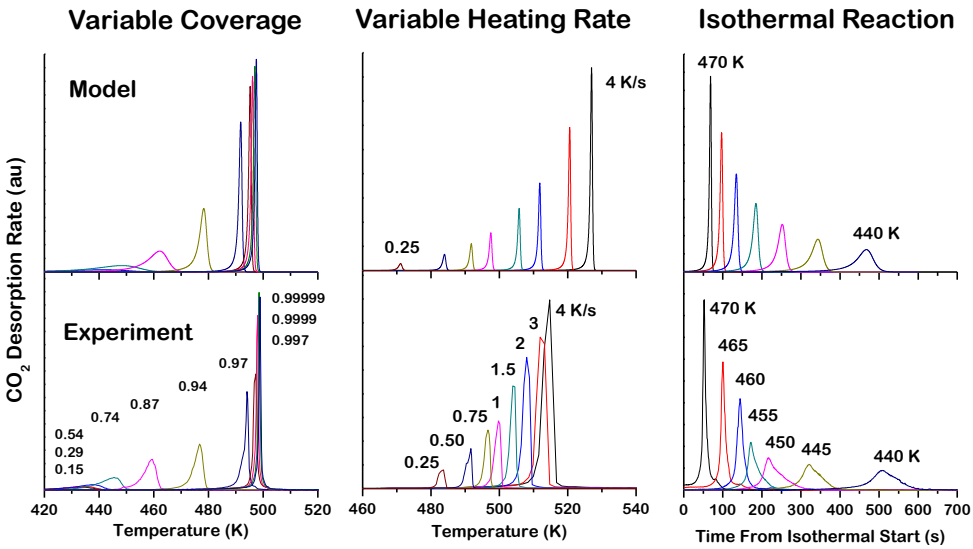

Figure 3.11. Experimental measurements (bottom row) and model simulations (top row) of the kinetics of D-TA decomposition on Cu(110) to yield CO_2 desorption. Left column) TPR spectra using various initial coverages of D-TA in the range $\theta_0^{TA} = 0.15 - 1.0$, as labeled with experimental data in bottom graph. Heating rate was β = 1 K/s. Middle column) TPR spectra using heating rates in the range β = 0.25 – 4 K/s as labeled in the bottom graph. Initial coverage of D-TA was $\theta_0^{TA} = 1$. Right column) Isothermal decomposition of D-TA on Cu(110) at temperatures in the range T_{iso} = 440 – 470 K, as labeled in the bottom graph. Initial coverage of D-TA was $\theta_0^{TA} = 1$.

3.3 Conclusions

The explosive decomposition of TA on Cu(110) is initiated by an irreversible process that leads to slow decrease in the coverage of TA on the surface and the concomitant formation of vacancies in the adsorbed overlayer. The initiation process is not associated with structural defects on the surface; instead it can be described simply as an irreversible initiation step in the reaction mechanism that is then followed by the explosive autocatalytic decomposition of TA. The onset of the explosive decomposition is accompanied by the appearance of Cu adatoms on the Cu(110) surface, observed in LEED and by STM as a $(\pm 6,7; \mp 2,1)$ phase.

Chapter 4

Surface chemistry of aspartic acid decomposition on Cu(110)

4.1 Introduction

In case of TA decomposition on the Cu(110) surface we observed (Figure 3.7) that the desorption of H_2 precedes the explosive decomposition of the monotartrate species [1, 103]. All other decomposition fragments desorb into the gas phase with the same rate-limiting step, as indicated by the overlapping leading edges of the TPR spectra. One method for probing the origin of this H_2 peak would involve the use of isotopically labeled tartaric acid. Isomers of tartaric acid have the general molecular formula: HOOC–$(CHOH)_2$–COOH. If we could obtain specifically deuterated tartaric acids such as DOOC–$(CHOH)_2$–COOD, HOOC–$(CDOH)_2$–COOH and HOOC–$(CHOD)_2$–COOH; a simple TPRS experiment performed by monitoring H and D bearing products would reveal the origin of the hydrogen atoms that initiate the explosive decomposition reaction. In an ideal scenario, the same experiments could be performed using isotopomers of tartaric acid with labeled C, H and O atoms at different positions. The data obtained would help assign the origin of atoms in the products and, thereby, understanding the mechanism of the surface reaction. However, a practical constraint to the above experiments is the fact that, tartaric acid isotopomers are not commercially available.

4.1.1 Aspartic acid as a probe molecule

We have demonstrated that 'surface explosions' can be exploited to attain high enantioselectivity on chiral surfaces. Considering the simplicity of the TPRS experiments and their significance in understanding the mechanism of surface explosion reactions, it is important to identify other chiral probe molecules that react via surface explosion and that can be obtained in isotopically labeled forms. Aspartic acid, HOOC–CH(NH_2)–CH_2–COOH, has a molecular structure similar to tartaric acid, i.e. a four-carbon backbone with carboxylic acid groups on either end i.e. at the C^1 and C^4 carbon atoms. Aspartic acid is an α–amino acid where the α–carbon atom is the chiral center. Figure 4.1 illustrates the two enantiomers of aspartic acid. Most importantly from the perspective of this work, a number of isotopomers of aspartic acid are commercially available in the enantiomerically pure L-form.

4.1.2 Aspartic acid decomposition on Cu(110)

Figure 4.2 depicts the TPR spectra for the decomposition of L–Asp on Cu(110) for increasing initial coverages 'θ_0^{Asp}' of L-Asp on the surface. It can be seen that, as θ_0^{Asp} increases, the TPR spectra shift to the higher temperatures and the range of peak temperatures spans from ~490 K at low coverage to 536 K at saturation. Also, at saturation coverage, a characteristic narrow peak with a ΔT_{FWHM} of ~3 K and a peak temperature at T_p = 536 K can be observed, which is indicative of surface explosion. Another signature of explosive kinetics is that the rate of reaction increases with the extent of the reaction during isothermal heating. Figure 4.3 depicts TPR spectra obtained at isothermal temperatures 'T_{iso}' in the

range 485–510 K while monitoring the CO_2 desorption rate as a function of lag time after reaching the isothermal temperature. It can be seen that the rate of reaction increases as a function of time at constant T_{iso}. As in the case of TA decomposition on Cu surfaces, the lower the value of T_{iso}, the longer the lag time before reaction initiation and longer the desorption peak time *'t_p'*.These two phenomenon are signatures of surface explosion mechanism and confirm that aspartic acid decomposition on the Cu(110) surface does proceed via an explosive mechanism. Therefore, aspartic acid was chosen as a probe molecule for investigating the chemistry of surface explosions.

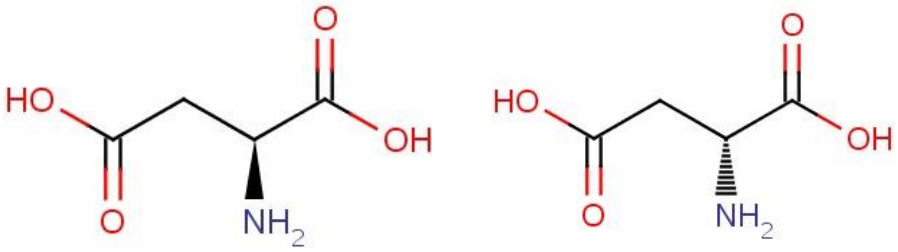

L-Aspartic Acid **D-Aspartic Acid**

Figure 4.1 D- and L- enantiomers of aspartic acid. Aspartic acid is an α-amino acid and the α-carbon atom is the chiral center. Various isotopically labeled varieties of aspartic acid are commercially available.

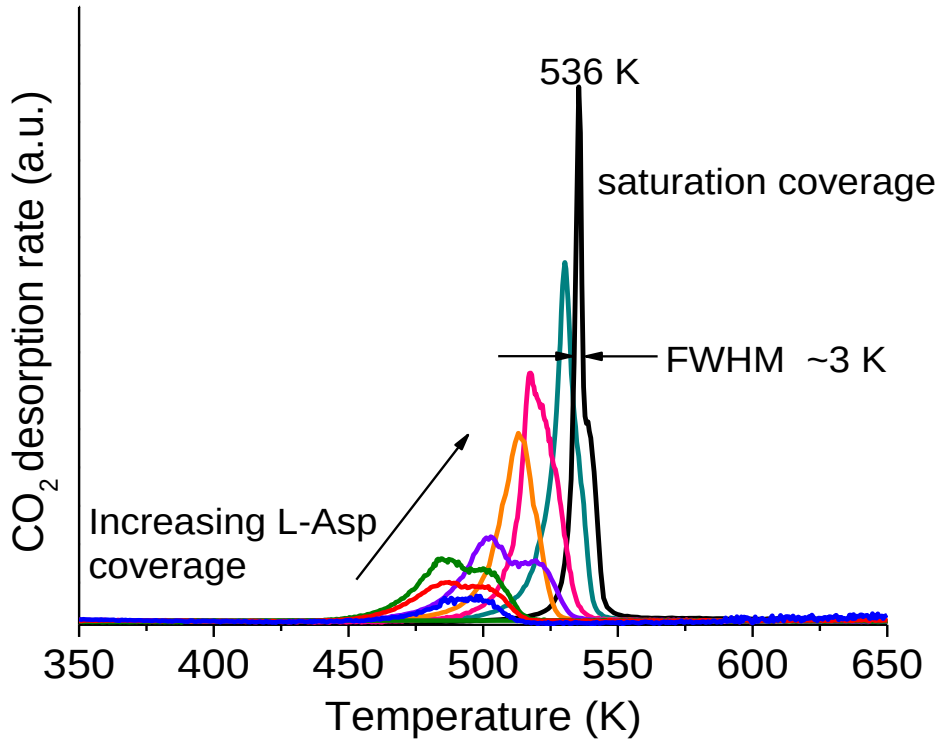

Figure 4.2 TPRS spectra of L–Asp on Cu(110) for increasing θ_0^{Asp}. The TPR spectra shift with peak temperature at T_p ~490 K at low coverage to T_p ~536 K at saturation. Also, at saturation coverage, the characteristic narrow peak with a ΔT_{FWHM} ~ 3 K is indicative of surface explosion.

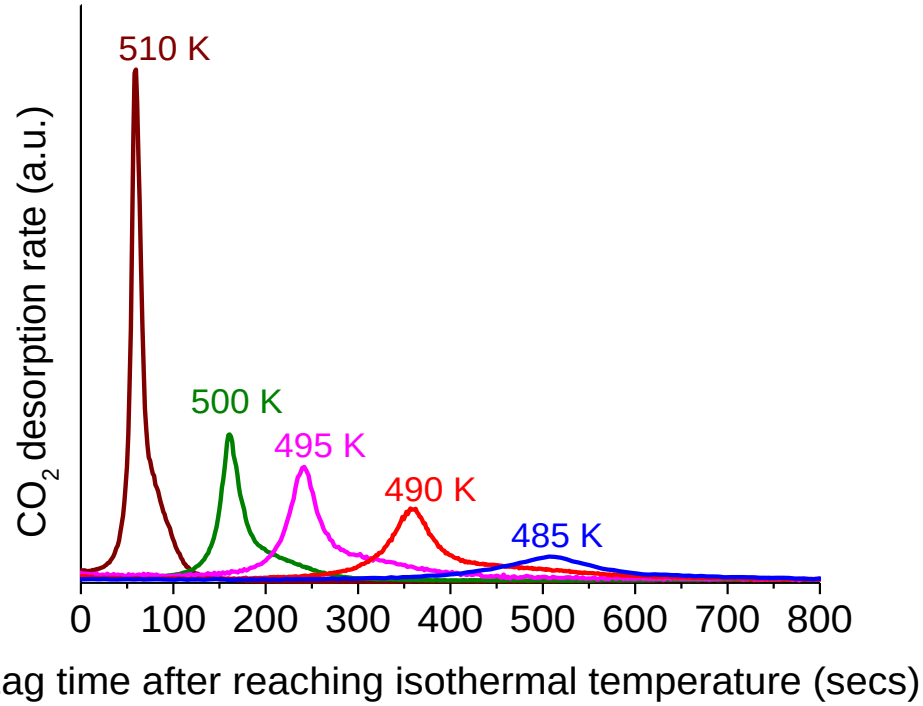

Figure 4.3 TPR spectra of L-Asp/Cu(110) obtained at various isothermal temperatures 'T_{iso}', at saturation coverage, while monitoring the CO_2 desorption rate as a function of the lag time after reaching T_{iso} (labeled with each spectrum). The rate of reaction increases as a function of time at constant T_{iso}. As in the case of TA decomposition on Cu surfaces, the lower the value of T_{iso}, the longer the lag time before reaction initiation and longer the desorption peak time *'t_p'*.

4.2 Surface chemistry and kinetics of aspartic acid decomposition on Cu (110)

4.2.1 XPS based determination of L-Asp form on Cu(110)

Tartaric acid can exist in three different forms on Cu surfaces: the bi–acid form [HOOC–CH(OH)–CH(OH)–COOH]; the monotartrate form in which one of the carboxylic acid groups has deprotonated to give a monocarboxylate moiety [OOC–CH(OH)–CH(OH)–COOH]; and the bitartrate form in which both acid groups have deprotonated [OOC–CH(OH)–CH(OH)–COO] [95-99, 101, 103, 114]. For the purpose of understanding the surface chemistry of decomposition, it is important to know the state of the adsorbed molecule which decomposes during the reaction. In our study, of Asp/Cu(110), XPS was used to determine the state of the adsorbed molecule. For example, in the case of TA/Cu(110), when TA is in a bi–acid form, the carbon atoms exist in two different states i.e. –C*OOH and –C*H(OH)–. In the monotartrate form, the carbon atoms exist in three different states i.e. –C*OO, –C*OOH and –C*H(OH). And in the bi tartrate form, the carbon atoms exist in –C*OO and –C*H(OH)– states. The '*' denotes the carbon atom in a particular state. Similarly, oxygen atoms exist in different states including –CO*O*, –CO*O*H and –CH(O*H)–, depending upon the state of the adsorbed molecule.

Figure 4.4 depicts C 1s, O 1s and N 1s XPS spectra obtained after dosing the crystal with Asp with surface temperature <330 K. This results in the deposition of Asp multilayers on the surface. The fit for the C 1s XPS spectrum at multilayer coverage (Figure. 4.4 a) shows peak energies corresponding to four groups with binding energies of: 285.7 eV (–C*H_2), 286.9 eV (–C*HNH_3^+), 288.6

eV (–C*OO) and 289.5 eV (–C*OOH). The fit for the O 1s XPS spectrum at multilayer coverage (Figure. 4.4 b) shows peak energies corresponding to two groups with binding energies of: 532 eV (–CO*O*) and 533.2 eV (–CO*O*H). The fit for N 1s XPS spectrum at multilayer coverage (Figure. 4.4 c) shows a major peak at 402.2 eV ($–N^*H_3^+$) and a minor peak at 400.2 eV ($–N^*H_2$). The minor peak in the N 1s XPS spectrum at 400.2 eV is assumed to arise from the molecules adsorbed on the surface while the peak at 402.2 eV arises from those in the multilayer. The XPS analysis is indicative of the presence of the zwitterionic form of L–Asp [$HOOC–CH_2–CH(NH_3)^+(COO)^-$] in the multilayer. In this form, the amine group is protonated and the α–carboxylic acid group is deprotonated, while the aliphatic side chain consists of a carboxylic acid at the γ–position [86, 115].

Upon heating the crystal to 405 K, as shown in the Figure 4.5 , the C 1s and O 1s XPS signals corresponding to the –COOH group, i.e. the C 1s signal at 289.5 eV and O 1s signal at 533.2 eV, disappear. The N 1s signal corresponding to the zwitterion i.e. $–N^*H_3$ at 402.2 eV disappears, whereas the signal at 400.2 eV corresponding to the amine group ($–N^*H_2$) dominates the XPS spectrum. This analysis is indicative of the presence of biaspartate species, $OOC–CH_2–CH(NH_2)–COO$, on the surface in which both the acid groups have deprotonated to form carboxylate moieties [86, 115].

All the experiments mentioned in the subsequent sections, unless otherwise mentioned, were performed at saturation coverage of L–Asp on the surface.

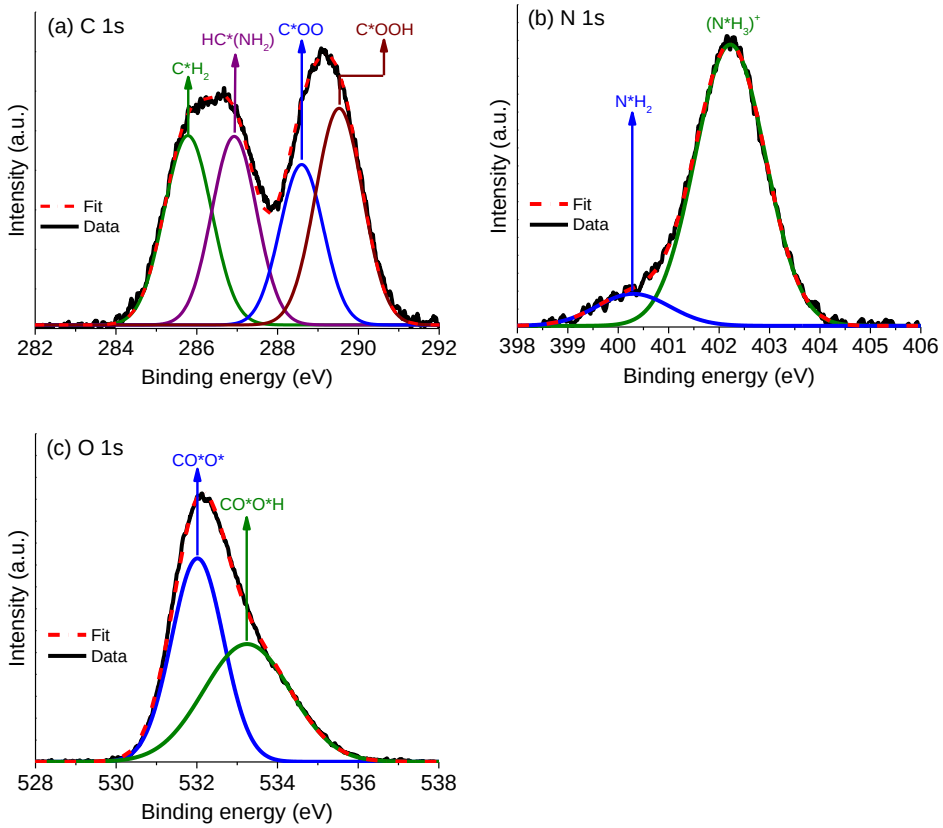

Figure 4.4 C 1s, O 1s and N 1s XPS spectra after dosing Cu(110) with L-Asp with the surface temperature <330 K. This results in formation of Asp multilayers on the surface. (a) The C 1s spectrum shows peaks with binding energies at 285.7 eV (–C*H_2), 286.9 eV (–C*HNH_3^+), 288.6 eV (–C*OO) and 289.5 eV (–C*OOH). (b) The O 1s spectrum shows peaks with binding energies at 532 eV (–CO*O*) and 533.2 eV (–CO*O*H). (c) The N 1s spectrum shows a major peak at 402.2 eV (–N*H_3^+) and a minor peak at 400.2 eV (–N*H_2). The XPS analysis is indicative of the presence of the zwitterionic form of L–Asp, $HOOC–CH_2–CH(NH_3)^+(COO)^-$, in the multilayer.

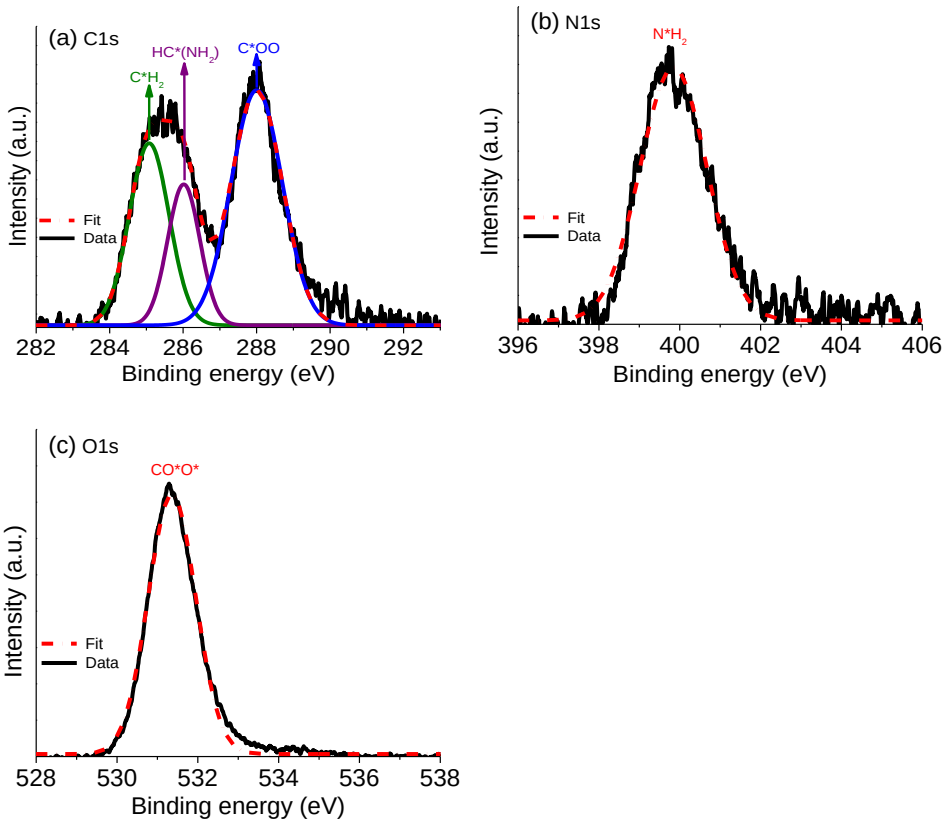

Figure 4.5 C 1s, O 1s and N 1s XPS spectra after heating the Cu(110) surface with multilayers of L-Asp to 405 K. This results in formation of Asp saturated, monolayer on the surface. With reference to Figure 4.3, the C 1s and O 1s XPS signals arising from the –COOH group i.e. the C 1s signal at 289.5 eV and O 1s signal at 533.2 eV, disappear and the N 1s signal corresponding to the zwitterion i.e. $–(N^*H_3)^+$ at 402.2 eV disappears. The signal at 400.2 eV corresponding to the amine group $–(N^*H_2)$ dominates the N 1s XPS spectrum. This analysis is indicative of the presence of biaspartate species, $OOC–CH_2–CH(NH_2)–COO$, on the surface.

4.2.2 L–Asp/Cu(110)

Figure 4.6 shows a subset of the TPR spectra obtained at multiple *m/q* ratios for L–Asp decomposition on Cu(110) at saturation coverage. The most prominent signal in the spectra corresponds to *m/q* = 44, i.e. CO_2, formed during the decomposition reaction. This signal in Figure. 4.6 has a width of 3.2 K and peak temperature of T_p = 535.5 K. It also shows a characteristic shoulder at T_s = 539.5 K. Corresponding to this shoulder are several other prominent *m/q* ratios (38–42), a subset of which is shown in Figure. 4.6 (b). Also, corresponding to CO_2 signal is a signal at *m/q* = 28, which show characteristic features similar to the CO_2 signal i.e. T_p = 535.5 K and T_s = 539.5 K, as shown in Figure. 4.6 (a).

4.2.2.1 Product analysis from multi-mass TPRS experiments

This section details the general analysis procedure followed for the identification of the products from multi–mass TPR spectra obtained during the decomposition reaction. In Figure 4.6 a, the *m/q* = 28 signal can arise either from CO, N_2, C_2H_4 or from the fragmentation of CO_2 or some other molecule. If the signal were to arise only from the fragmentation of CO_2, the normalized spectra for *m/q* = 28 and 44 should overlap each other. This is assuming, of course, that the *m/q* = 44 signal arises only from the fragmentation of CO_2 formed during aspartic acid decomposition. It is evident from Figure 4.7 which represents the normalized desorption signals for *m/q* = 28 and 44 that the signal corresponding to *m/q* = 28 is not entirely due to CO_2 fragmentation. Acetonitrile (C_2H_3N), one of the products formed during L–Asp decomposition has a prominent fragmentation signal at *m/q* = 28. In Figure 4.6 b, we can observe prominent signals

corresponding to *m/q* = 38–42. Figure 4.8 b compares the relative areas of the signals at *m/q* = 28 (after appropriately subtracting the contribution from the CO_2 signal) and *m/q* = 38-42, plotted as a function of their *m/q* ratios. When the plot in Figure 4.8 b is compared with the C_2H_3N mass spectrum in Figure 4.8 a (which was measured for our system), it is evident from this comparison that acetonitrile is one of the products formed during the decomposition reaction. Figure 4.9 represents the normalized TPR spectra of *m/q* = 38 – 42. The overlapping of these signals further confirms the fact that these signals are only due to acetonitrile fragmentation. H_2 was identified as another product formed during the L-Asp decomposition reaction. H_2 kinetics will be discussed in detail in section 4.2.4.1. CO_2, C_2H_3N, and H_2 entirely account for the products formed during L-Asp decomposition on Cu(110). So, the general decomposition of L–Asp decomposition on Cu(110) can be represented as:

$$OOC–CH_2–CH(NH_2)–COO \rightarrow CO_2 + C_2H_3N + H_2$$

In order to identify the specific carbon atoms or groups on the decomposing molecule which end up in each of these products, we used specifically labeled isotopomers of aspartic acid.

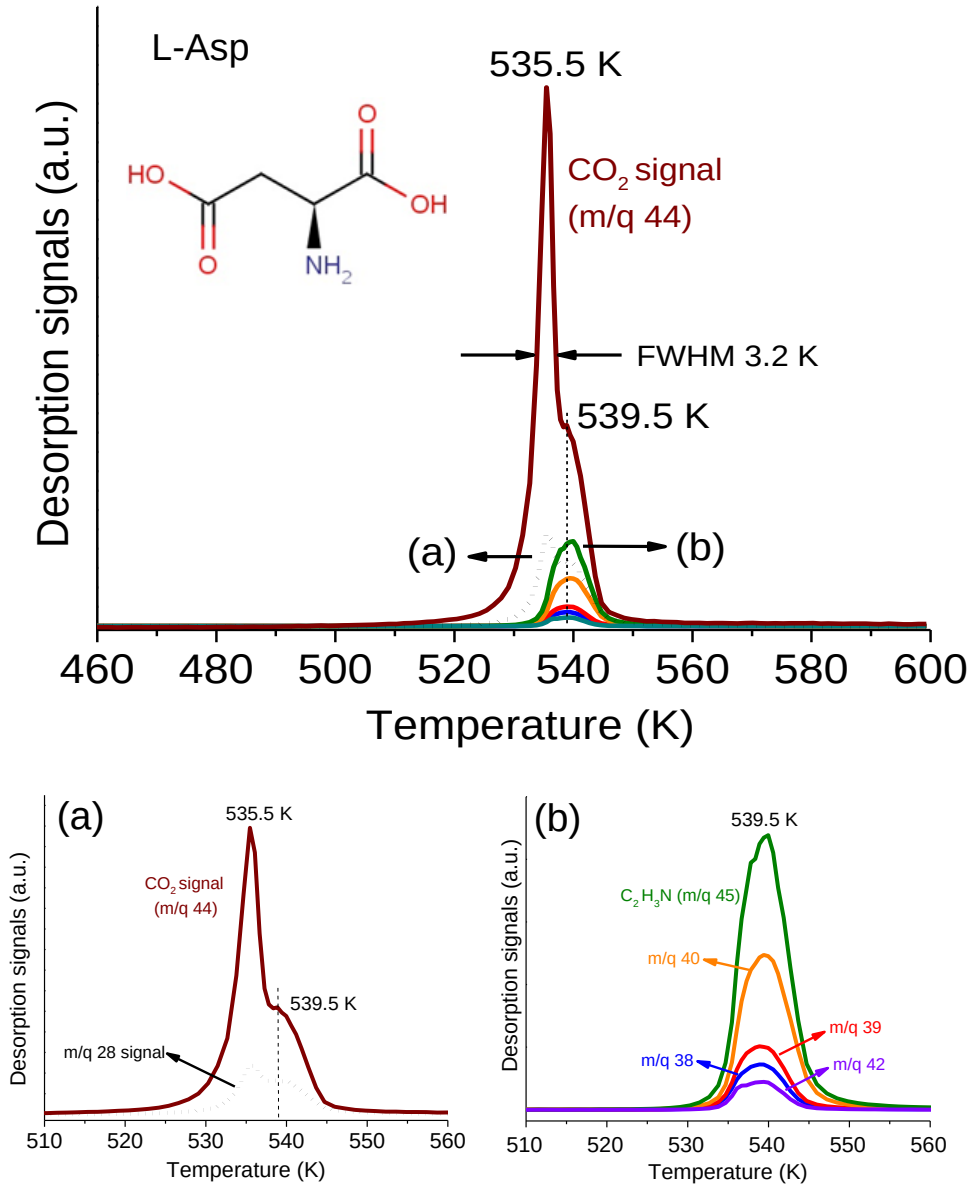

Figure 4.6 Subset of the TPR spectra obtained at multiple *m/q* ratios for L–Asp decomposition on Cu(110) at saturation coverage. The most prominent signal in the spectra corresponds to *m/q* = 44 i.e. CO_2, formed during the reaction. This signal has a width of 3.2 K and peak temperature of T_p = 535.5 K. It also shows a characteristic shoulder at T_s = 539.5 K. Corresponding to this shoulder are several other prominent signals (*m/q* = 38–42), a subset of which is shown in (b). Corresponding to the CO_2 signal is a signal at *m/q* = 28, which shows features similar to the CO_2 signal i.e. T_p = 535.5 K and T_s = 539.5 K, a subset of which is shown in (a).

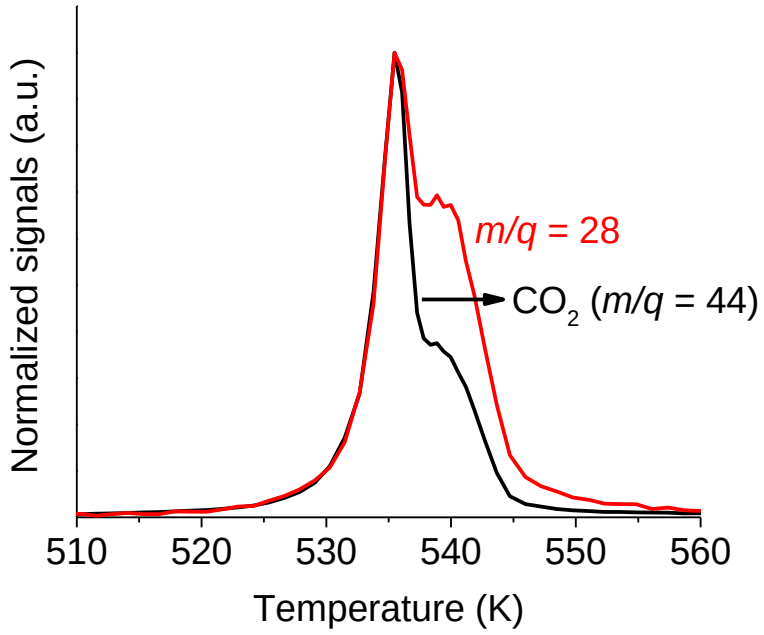

Figure 4.7 The normalized TPR spectra at *m/q* = 28 and 44. These signals do not overlap each other indicating that *m/q* = 28 signal is not entirely due to CO_2 fragmentation.

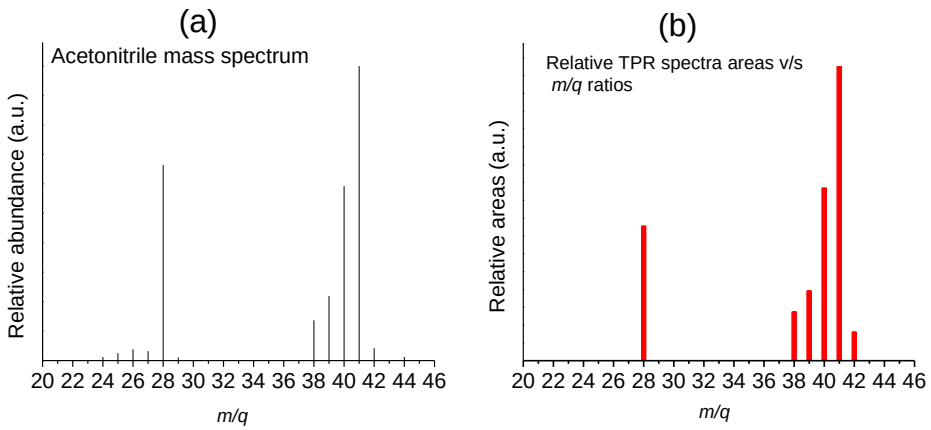

Figure 4.8 (a) The acetonitrile (C_2H_3N) fragmentation pattern determined for our system. (b) The area under the TPR spectra at *m/q* = 28 (after appropriate signal subtractions taking into account the fragmentation from the CO_2 signal) and *m/q* = 38-42 [obtained during L-Asp decomposition on Cu(110)], plotted as a function of the *m/q* ratios. It is evident from this comparison that C_2H_3N is one of the products formed during the decomposition of L-Asp on Cu(110).

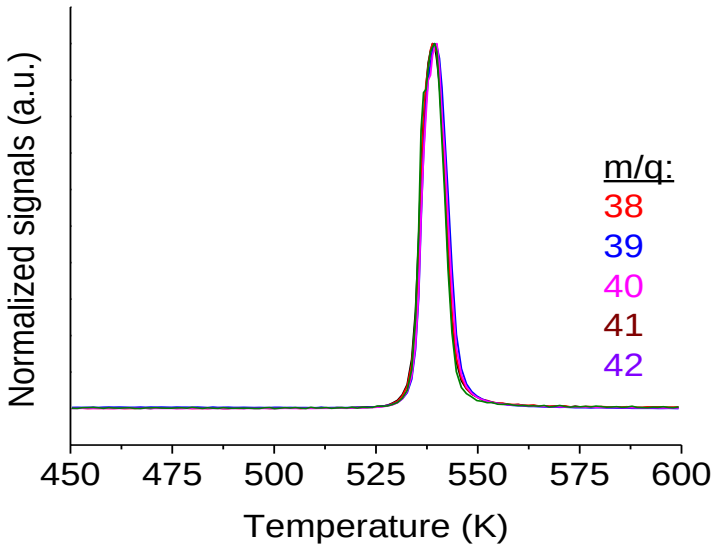

Figure 4.9 Normalized TPR spectra obtained at *m/q* = 38–42. These signals overlap each other confirming the fact that TPR spectra corresponding to these masses are only due to acetonitrile fragmentation.

4.2.3 1,4–$^{13}C_2$ L–Asp/Cu(110)

Figure 4.10 depicts a subset of TPR spectra obtained at multiple *m/q* ratios for 1,4–$^{13}C_2$ L–Asp [OO^{13}C–CH$_2$ –CH(NH$_2$)–^{13}COO] decomposition on Cu(110) at saturation coverage. The most prominent signal in the TPR spectra now corresponds to *m/q* = 45 i.e. $^{13}CO_2$. This signal displays the same features as the signal at *m/q* = 44, i.e. the CO_2 signal in case of unlabeled L–Asp/Cu(110). The *m/q* = 44 signal absent in Figure 4.10. Similar to the CO_2 signal for L-Asp/Cu(110), the $^{13}CO_2$ signal from 1,4–$^{13}C_2$ L–Asp/Cu(110) has a prominent peak at T_p = 535.5 K with a width of ΔT_{FWHM} = 3.2 K. It also shows a characteristic shoulder at T_s = 538.5 K. Corresponding to this shoulder are signals corresponding to C_2H_3N i.e., *m/q* = 38–42, a subset of which is shown in Figure 4.10 b. An interesting point to note is the fact that acetonitrile signals remain essentially unaltered inspite of the ^{13}C labeling on the C^1 and C^4 atoms. Also, corresponding to the $^{13}CO_2$ signal, is a signal at *m/q* = 29 signal due to the fragmentation of $^{13}CO_2$, with the *m/q* = 28 signal arising from to C_2H_3N fragmentation.

This analysis is indicative of the fact that the C^1 and C^4 atoms in the decomposing L-Asp are solely responsible for CO_2 formation, and, that the C^2 and C^3 atoms are not involved in this process. Conversely, the C^2 and C^3 atoms are end up solely in the C_2H_3N. The decomposition of 1,4–$^{13}C_2$ L–Asp decomposition on Cu(110) can be represented as:

$$OO^{13}C–CH(NH_2)–CH_2–^{13}COO \rightarrow {}^{13}CO_2 + C_2H_3N + H_2$$

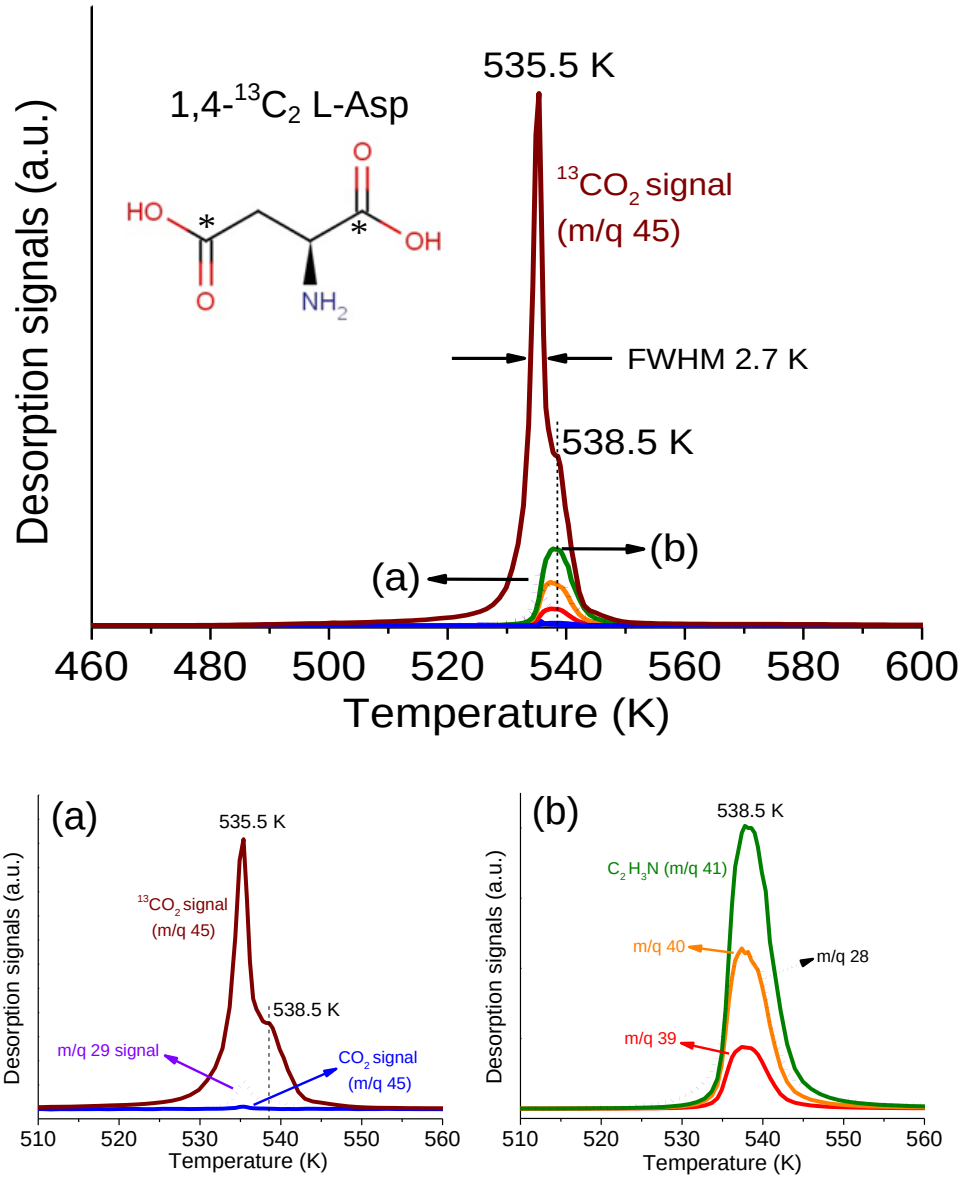

Figure 4.10 Subset of the TPR spectra obtained at multiple *m/q* ratios for 1,4-$^{13}C_2$ L–Asp decomposition on Cu(110) at saturation coverage. The most prominent signal in the spectra corresponds to *m/q* = 45 i.e. $^{13}CO_2$, formed during the reaction. This signal has a width of 2.7 K and peak temperature of T_p = 535.5 K. It also shows a characteristic shoulder at T_s = 538.5 K. Corresponding to this shoulder are several other prominent signal at *m/q* = 28, 38–42, a subset of which is shown in (b). Corresponding to the $^{13}CO_2$ signal is present a signal at *m/q* = 29, which show features similar to the $^{13}CO_2$ signal at *m/q* = 45 as represented in (a). The *m/q* = 44 signal is completely absent while the signal at *m/q* = 28 primarily arises from C_2H_3N fragmentation.

4.2.4 1–^{13}C L–Asp/Cu(110)

Figure 4.11 depicts a subset of TPR spectra obtained at different masses during 1-^{13}C L-Asp [OOC–CH_2 –$CH(NH_2)$–^{13}COO] decomposition on Cu(110) at saturation coverage. In this case, the CO_2 i.e., *m/q* = 44 signal has a peak temperature of T_p = 535 K and it only corresponds to the primary peak that was observed at T_p *~535 K* in the case of L-Asp/Cu(110) and 1,4-$^{13}C_2$ L-Asp/Cu(110). The $^{13}CO_2$ i.e., *m/q* = 45 signal on the other hand has a peak temperature of T'_p = 539 K and it only corresponds to the position of the shoulder that was observed at T_s ~539 K in the case of L-Asp and 1,4-$^{13}C_2$-L-Asp on Cu(110). TPRS signals corresponding to C_2H_3N remain unaltered compared to those observed in case of L-Asp/Cu(110) and 1,4-$^{13}C_2$ L-Asp/Cu(110). Also, the *m/q* = 29 signal corresponds to $^{13}CO_2$ fragmentation only while the *m/q* = 28 signal now has contributions from both CO_2 and C_2H_3N fragmentation.

This analysis is indicative of the fact that during L-Asp decomposition on Cu(110), the C^4 carbon atom ends up in the main CO_2 peak with a peak temperature of T_p = 535 K, while the $^{13}C^1$ carbon atom ends up in the $^{13}CO_2$ shoulder at T_s = 539 K observed in the TPR spectra. Thus, during the decomposition process, the C^3–C^4 bond ruptures first, resulting in the formation of CO_2 comprising of C^4 atom and an intermediate species that is comprised of C^1, C^2 and C^3 atoms. Th C^4O_2 desorption is observed as the first and the most prominent TPRS signal with a peak temperature T_p = 535 K. The intermediate species decomposes to form $^{13}CO_2$, H_2 and C_2H_3N as major products. This species has a slightly higher barrier to decomposition than that of the C^3-C^4 bond in the

adsorbed biasparate, characterized by product TPRS signals with a higher peak temperature T_s = 539 K. This observation is more obvious in TPR spectra corresponding to lower initial coverages in Figure 4.2, depicting L-Asp decomposition on Cu(110) at variable coverage, in which we see two prominent peaks in the TPR spectra.

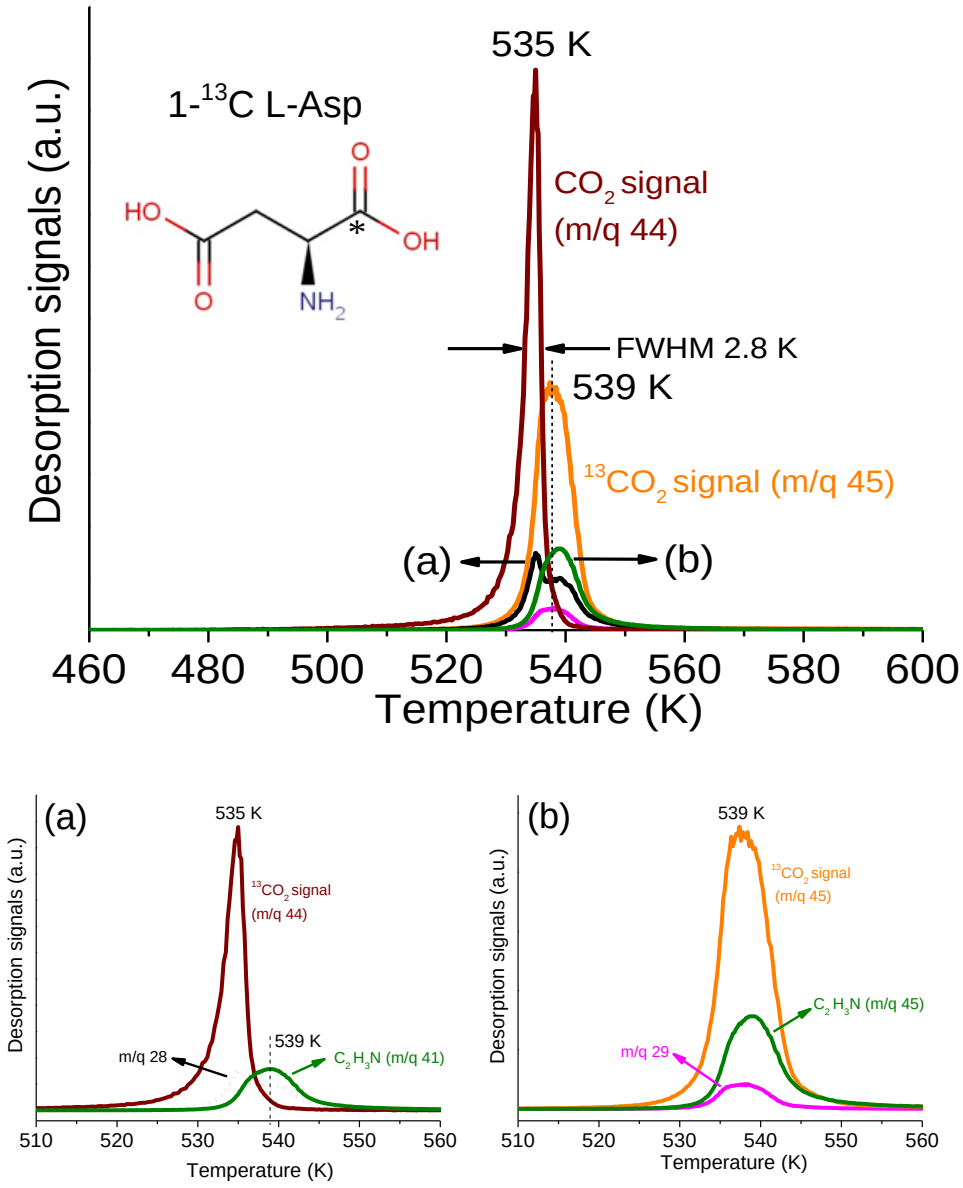

Figure 4.11 Subset of the TPR spectra obtained at multiple *m/q* ratios for 1-^{13}C L-Asp decomposition on Cu(110) at saturation coverage. The *m/q* = 44 signal i.e. CO_2 formed during the reaction has a peak temperature of T_p = 535 K. The *m/q* = 45 signal i.e. $^{13}CO_2$ has a peak temperature of T_p' = 539 K and it only corresponds to the position of the shoulder T_s that was observed in the case of L-Asp and 1,4-$^{13}C_2$ L-Asp on Cu(110). Corresponding to *m/q* = 45 signal are signals at *m/q* = 29 and 41, a subset of which is shown in (b). The *m/q* = 29 signal arises from C_2H_3N fragmentation. The *m/q* = 28 signal now has contributions from both CO_2 and C_2H_3N.

4.2.4.1 Selective elimination of C^4O_2 group

Figure 4.12 illustrates the TPR spectra obtained at *m/q* = 28, 29, 41, 44 and 45, for 1-^{13}C L-Asp decomposition on Cu(110) at low initial Asp coverage on the surface. In this figure, at 470 K, the rate of CO_2 desorption is ~25 times that of $^{13}CO_2$ desorption. There are a couple of ways in which we can exploit this feature to selectively eliminate the carboxylate group containing the C^4 atom, and isolate the intermediate species containing the C^1, C^2, and C^3 atoms. One method would involve heating the crystal dosed with L-Asp to ~470 K, and quenching it so as to retain the intermediate species on the surface. Another way to achieve this would be to expose the Cu(110) surface maintained at 470 K to L-Asp. At this temperature, the C^3-C^4 bond breaking process has a higher rate compared to the decomposition of the intermediate species. We can thus selectively eliminate the carboxylate group containing the C^4 atom and populate the surface with the intermediate surface C^1, C^2 and C^3 atoms, for further analysis. Figure 4.13 a illustrates the TPR spectra obtained after exposing the crystal kept at 470 K to 1-^{13}C L-Asp vapor. The difference between the CO_2 and the $^{13}CO_2$ signals confirms our hypothesis that, during dosing, the intermediate species comprising of C^1, C^2 and C^3 atoms is isolated on the surface. Figure 4.13 b illustrates the XPS spectra obtained for a Cu(110) surface populated with this intermediate species. The relative decrease in the ratio of the C*OO signal intensity w.r.t. the C^*H_2 and $HC^*(NH_2)$ signals, compared to this ratio in case of the C 1s XPS spectrum at saturation coverage in Figure 4.5, is consistent with the result from the TPRS experiment.

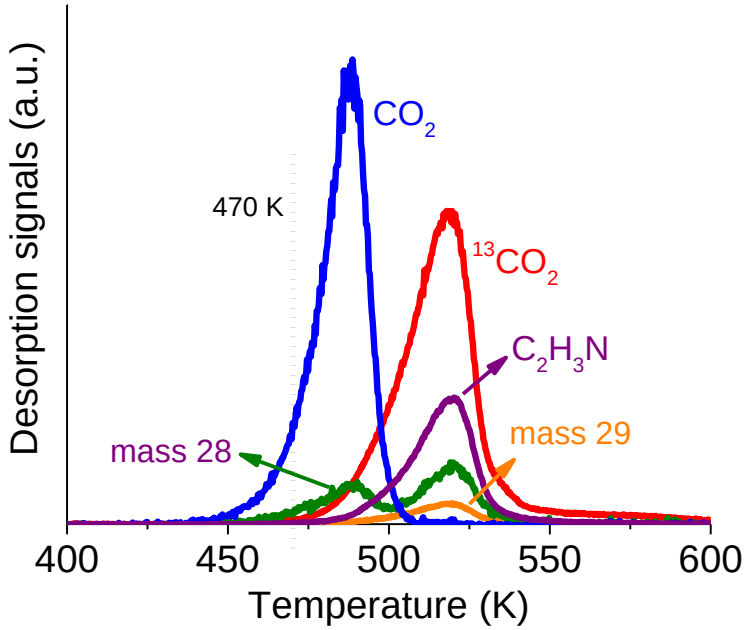

Figure 4.12 The TPR spectra obtained at *m/q* = 28, 29, 41, 44 and 45, for 1-^{13}C L-Asp decomposition on Cu(110) at low initial Asp coverage on the surface. In this figure, at 470 K, the rate of CO_2 desorption is ~25 times that of $^{13}CO_2$ desorption.

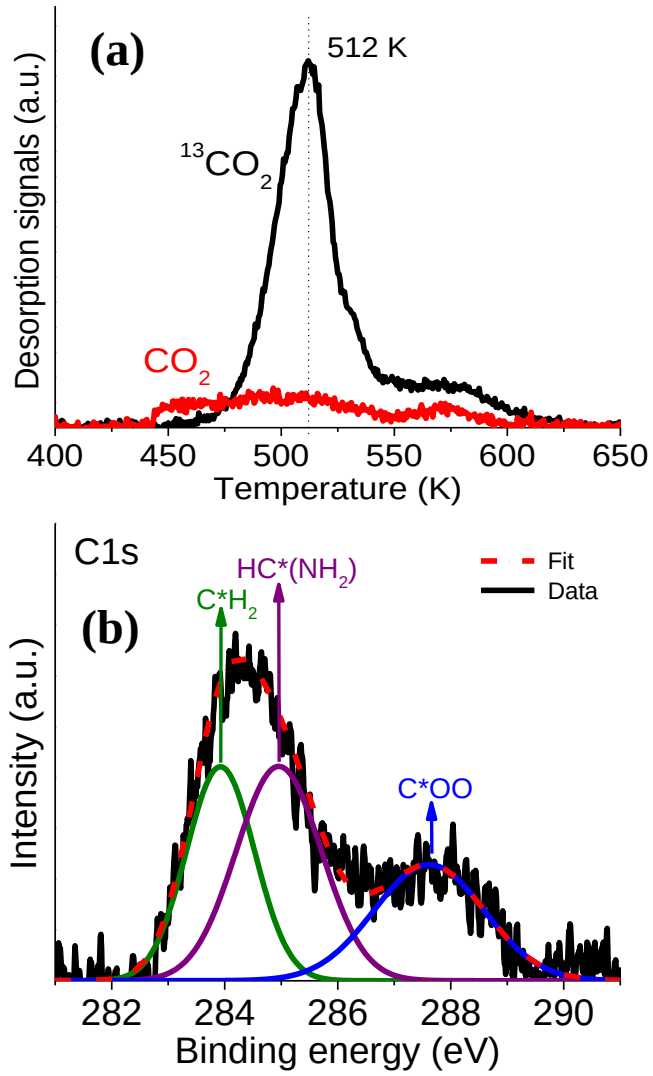

Figure 4.13 (a) The top section illustrates the TPR spectra obtained at *m/q* = 44 and 45, after exposing the Cu(110) crystal kept at 470K to 1-^{13}C L-Asp vapor. The difference between the CO_2 and the $^{13}CO_2$ signals confirms our hypothesis that, during dosing, the carboxylate group containing the C^4 atom is selectively eliminated, while the intermediate species comprising of C^1, C^2 and C^3 atoms is isolated on the surface. (b) The bottom section illustrates the XPS spectrum obtained from a Cu(110) surface populated with this intermediate species. The ratio of the relative decrease in C*OO signal intensity, w.r.t. C*H$_2$ and the HC*(NH$_2$) signals compared to this ratio in the the C 1s XPS spectrum at saturation coverage in Figure 4.5, is consistent with the result from the TPRS experiment.

4.2.4.2 Multi-mass isothermal TPR spectra for product analysis

As discussed earlier, one of the signature characteristics of a surface explosion is that the rate of reaction increases with the extent of the reaction during isothermal heating [1, 103]. Figure 4.3 depicts the TPR spectra obtained for m/q = 2, 28, 29, 40, 41, 44 and 45 during isothermal heating for saturation coverage of L–Asp/Cu(110). Let us consider the spectrum obtained at isothermal temperature of T_{iso} = 490 K. Here, the reaction spans around 250 s this extended time span can be useful for accurately monitoring multiple products formed during the reaction or for a detailed investigation of the differences between the desorption kinetics of various products. Figure 4.14 a) represents the TPR spectra obtained for m/q = 2, 28, 29, 40, 41, 44 and 45, during isothermal heating for saturation coverage of 1-^{13}C L-Asp / Cu(110). It is evident from the figure that the differences between the kinetics of different products are more prominent in the isothermal TPR spectra. For example, in the Figure 4.14 we can see that the difference between the peak times for the CO_2 and the $^{13}CO_2$ signals is ~60 s as opposed to ~4 s in a regular TPRS experiment. Also, using the product analysis technique for multi-mass TPRS experiments, it is possible to compare all the signals accurately in one single experiment.

4.2.4.3 Biaspartate surface species

Using XPS analysis we demonstrated that aspartic acid is present on the surface in biaspartate form at saturation coverage after adsorption at 405 K. Figure 4.14 b. depicts a subset of isothermal TPR spectra at T_{iso} = 490 K, obtained at CO_2, $^{13}CO_2$ and H_2. It is evident that H_2 desorption occurs only after the CO_2

desorption from the surface. This is consistent with the XPS analysis that, L-Asp is present on the surface in biaspartate form.

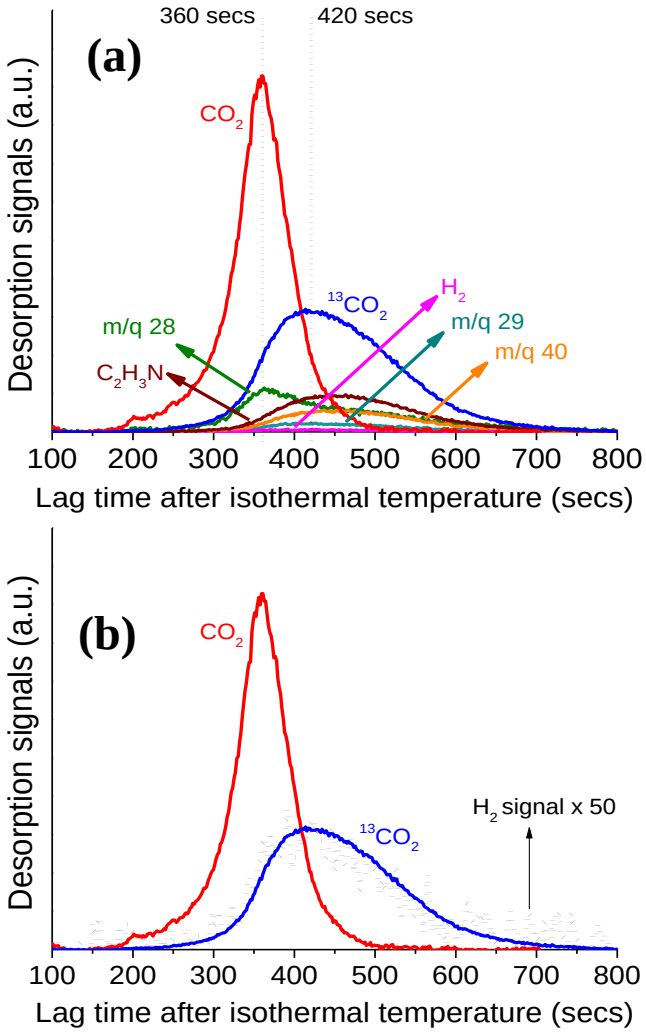

Figure 4.14 (a) The TPR spectra obtained at *m/q* = 2, 28, 29, 40, 41, 44 and 45 during isothermal heating at T_{iso} = 490 K for saturation coverage of 1-^{13}C L–Asp/Cu(110). It is evident from the figure that the differences between the kinetics of different products are more prominent in the isothermal TPR spectra. (b) Subset isothermal TPR spectra of (a) comparing CO_2, $^{13}CO_2$ and H_2 signals. H_2 signal is scaled by a factor of 50 for comparison. It is evident that H_2 desorption occurs only after the CO_2 desorption from the surface. This is consistent with the XPS analysis that, L-Asp is present on the surface in biaspartate form.

4.2.4.4 Surface chemistry and kinetics of L-Asp/Cu(110)

The decomposition reaction of 1,4–$^{13}C_2$ L–Asp decomposition on Cu(110) can now be represented in 2 steps as:

$$OO^{13}C\text{–}CH(NH_2)\text{–}CH_2\text{–}COO \xrightarrow[T_p = 536\ K]{k_1} CO_2 + OO^{13}C\text{–}CH(NH_2)\text{–}CH_2$$

$$OO^{13}C\text{–}CH(NH_2)\text{–}CH_2 \xrightarrow[T_s = 539\ K]{k_2} {}^{13}CO_2 + C_2H_3N + H_2$$

From the TPRS experiments, we observe a difference of ~4 K between the peak temperatures for CO_2 signal and that of other products. Also, CO_2 is the only product formed during the first reaction step and there is no evidence of $^{13}CO_2$ formation. We also discussed earlier that the CO_2 peak results entirely from the carboxylate group containing the C^4 atom, while the peak corresponding to $^{13}CO_2$ results entirely from the carboxylate group containing the C^1 atom. Therefore, during the decomposition of L-Asp/Cu(110), the CO_2 formed during each step can be considered as a separate product.

For kinetic modeling of the autocatalytic decomposition reaction of L-Asp/Cu(110), 1-^{13}C L-Asp is a suitable isotopomer since it differentiates between the two CO_2 molecules, i.e. C^1O_2 and C^4O_2 formed during the reaction. The surface chemistry of the autocatalytic decomposition of L-Asp on Cu(110) can now be represented as :

$$\bullet O_2C\text{-}CH(NH_2)\text{-}CH_2\text{-}CO_2 \rightarrow O_2C\text{-}CH(NH_2)\text{-}CH_2\text{-}CO_2 + \bullet \qquad k_i \quad .. (4.1)$$

$$\bullet O_2C\text{-}CH(NH_2)\text{-}CH_2\text{-}C^4O_2 + n\cdot\bullet \rightarrow C^4O_2 + \bullet O_2C\text{-}CH(NH_2)\text{-}CH_2 + n\cdot\bullet \qquad k_e \quad .. (4.2)$$

$$\bullet O_2C^1\text{-}CH(NH_2)\text{-}CH_2 + n\cdot\bullet \rightarrow C^1O_2 + C_2H_3N + H_2 + (1+ n)\cdot\bullet \qquad k_r \quad .. (4.3)$$

where, • represents an adsorption site on the surface; k_i, k_e and k_r are the rate constants.

In summary, as seen with the case of TA/Cu(110), the L-Asp/Cu(110) decomposition process will also involve an initiation step with rate constant 'k_i', and an explosive decomposition step with rate constant 'k_e' [1, 103]. The explosive decomposition of L-Asp results in the formation of C^4O_2 and an intermediate surface species, $\bullet O_2C^3\text{-}C^2H(NH_2)\text{-}C^1H_2$. C^4O_2 desorption is an instantaneous process [69, 96], and the kinetics of C^4O_2 desorption at variable initial surface coverage 'θ_0^{Asp}', variable heating rate 'β', and variable isothermal temperature 'T_{iso}' were used to model L-Asp/Cu(110) decomposition kinetics for the determination of the rate constants k_i and k_e.

Let the surface coverage of Asp (i.e. $\bullet O_2C\text{-}CH(NH_2)\text{-}CH_2\text{-}CO_2$) in eqn. 4.1 and 4.2 be represented as θ^{Asp}. Therefore, based in our understanding of the kinetics for TA/Cu(110) system from eq. 4.1 and 4.2, the rate of decomposition of L-Asp can now be represented as [1, 103]:

$$r_A = -\frac{d\theta_A}{dt} = k_i\theta^{Asp} + k_e\theta^{Asp}(1-\theta^{Asp})^n \quad \text{..... (4.4)}$$

$$r_A = -\frac{d\theta^{Asp}}{dt} = A_i e^{\frac{-\Delta E_i}{RT}}\theta^{Asp} + A_n e^{\frac{-\Delta E_e}{RT}}\theta^{Asp}(1-\theta^{Asp})^n \quad \text{..... (4.5)}$$

where, A_i & A_e, – nucleation and explosion pre-exponents respectively

ΔE_i & ΔE_e – nucleation and explosion energies respectively

n – order of the explosion reaction w.r.t the vacancy concentration

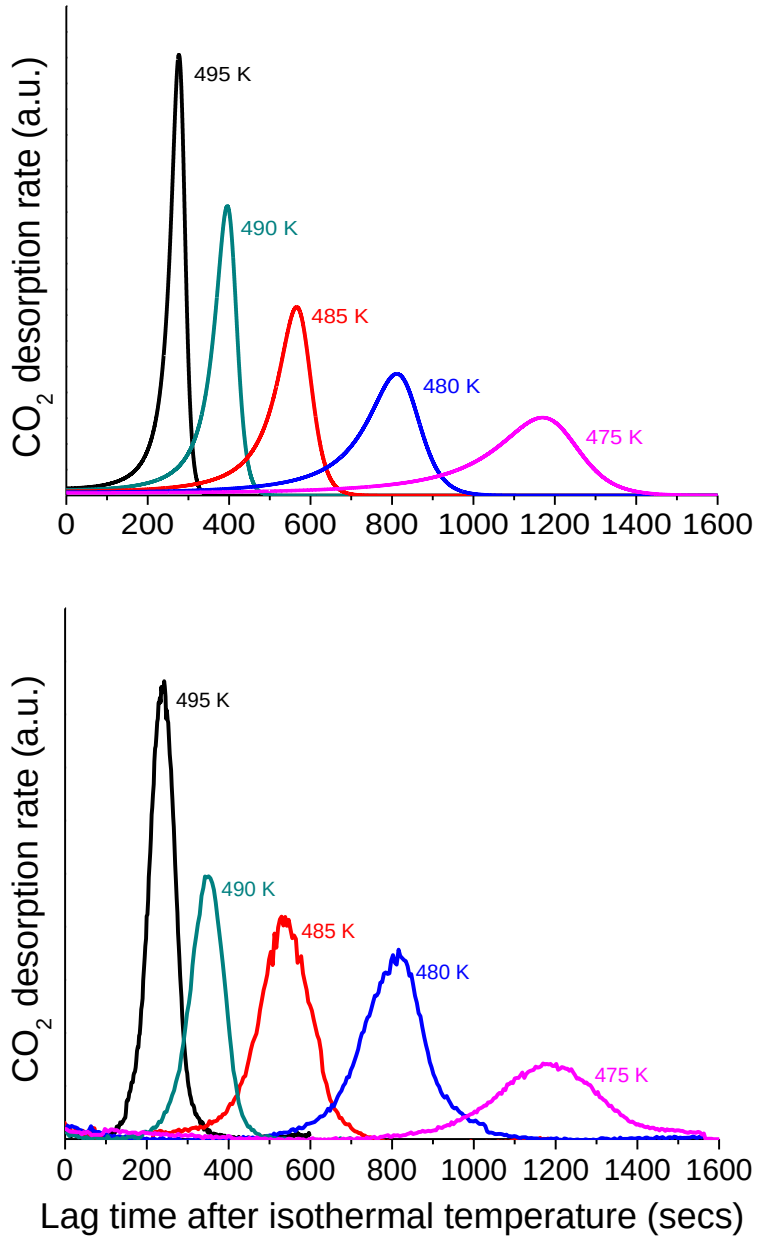

Figure 4.15 Simulated model fits (top section) and TPR spectra (bottom section) obtained at various isothermal temperatures 'T_{iso}' for saturation coverage of L-Asp on Cu(110). The model fits use n = 2 in the equation $r_A = -\frac{d\theta^{Asp}}{dt} = A_i e^{\frac{-\Delta E_i}{RT}}\theta^{Asp} + A_n e^{\frac{-\Delta E_e}{RT}}\theta^{Asp}(1-\theta^{Asp})^n$ and the parameter values as presented in the Table 4.1. The isothermal temperatures are labeled with each spectrum.

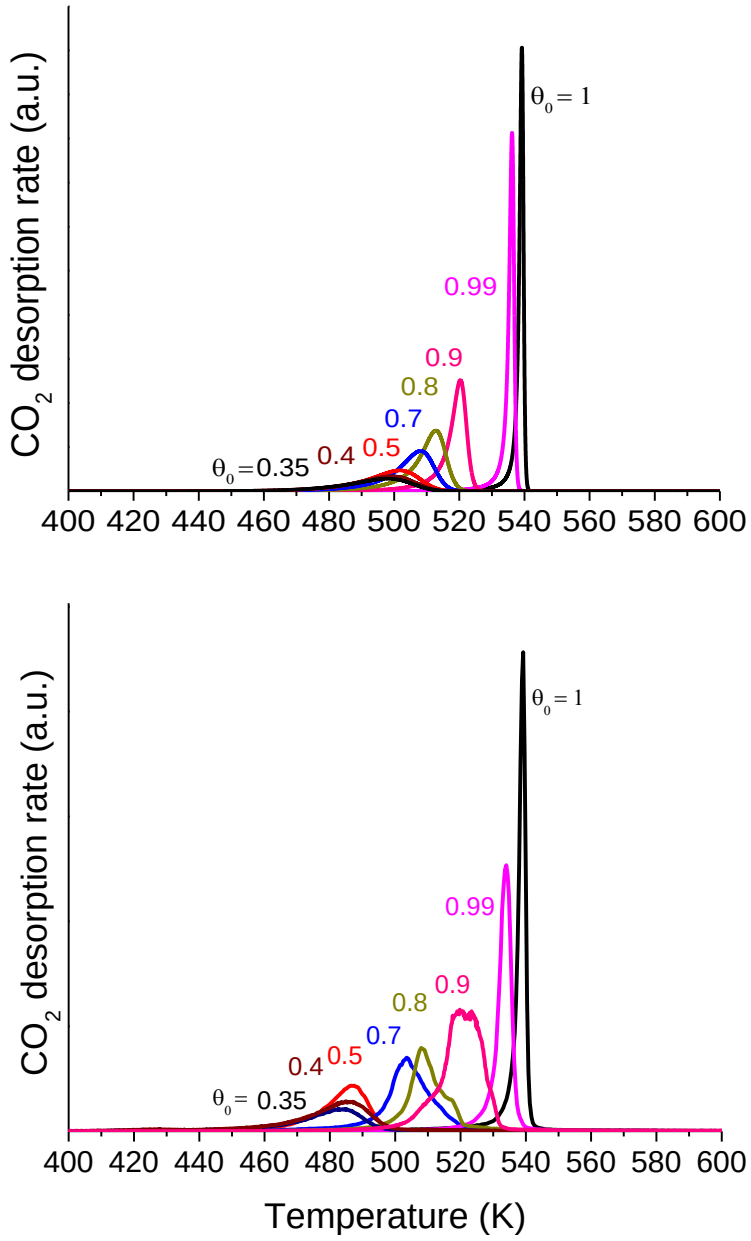

Figure 4.16 Simulated model fits (top section) and TPR spectra (bottom section) obtained for increasing initial coverage of L-Asp onCu(110) i.e. θ_0^{Asp}. The model fits use n = 2 in the equation $r_A = -\frac{d\theta^{Asp}}{dt} = A_i e^{\frac{-\Delta E_i}{RT}}\theta^{Asp} + A_n e^{\frac{-\Delta E_e}{RT}}\theta^{Asp}(1-\theta^{Asp})^n$ and the parameter values as presented in the Table 4.1. Initial coverages have been approximated using the area under the spectra for each peak. The estimated coverages are labeled with each TPR spectrum.

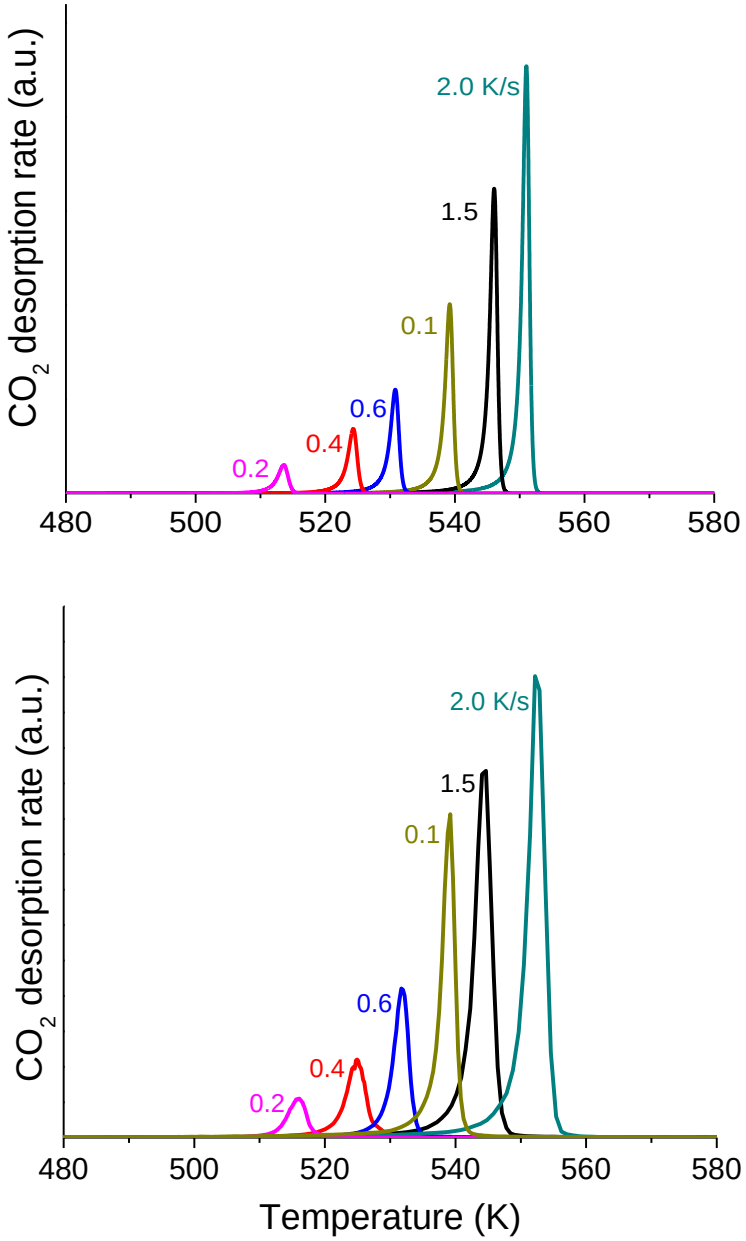

Figure 4.17 Simulated model fits (top section) and TPR spectra (bottom section) obtained at various heating rates 'β' for saturation coverage of L-Asp on Cu(110). The model fits use n = 2 in the equation $r_A = -\frac{d\theta^{Asp}}{dt} = A_i e^{\frac{-\Delta E_i}{RT}}\theta^{Asp} + A_n e^{\frac{-\Delta E_e}{RT}}\theta^{Asp}(1-\theta^{Asp})^n$ and the parameter values as presented in the Table 4.1. The heating rates are labeled with each TPR spectrum.

Table 4.1 Kinetic parameters estimated* for the explosive decomposition of Asp/Cu(110) using eqn. 4.5 with $n = 2$.

	A (1/s)	ΔE (kJ/mole)
Initiation, k_i	8.7×10^6	100.2
Explosion, k_e	1.1×10^{17}	169.2

* Parameter estimation by minimization of $\sum \left(x_{expt} - x_{model}\right)^2 / x_{expt}^2$ where x are the peak temperatures and the peak times for the variable coverage, variable heating rate and isothermal heating rate TPRS data in Figures 4.15 - 4.17.

Since an equation of the form of eqn. 4.5 with n = 2 produced the best fits for TA/Cu(110) data [103], the same value of 'n' was assumed for the kinetic modeling of Asp/Cu(110) data . The TPR spectra depicted in the lower sections of Figures 4.16, 4.17 and 4.18 are the actual experimental data plots. The TPR spectra depicted in the upper sections of Figures 4.16, 4.17 and 4.18 have been simulated using the rate expression in eqn. 4.5 with n = 2. The values of the estimated parameters in the simulated spectra i.e. A_i, A_e, ΔE_i and ΔE_e are listed in Table 4.1. The parameter estimation approach searched for the values of ln(A_i), ln(A_e), ΔE_i and ΔE_e, that minimized the differences between the predicted and the measured values of peak temperatures, T_p, for the variable coverage and heating rate experiments and peak times, t_p, for the isothermal experiments. It can be seen from Figures 4.15-4.17 that the simulated model fits and the TPRS data are in good agreement. In the case of the TPRS data at variable coverage, the area under the TPR spectra was used to determine the initial coverage of L-Asp on the surface. However, since the decomposition kinetics are sensitive to vacancy concentration, more robust means such as XPS should be implemented in future studies to estimate the surface coverage. Beyond θ_0^{Asp} = 0.9, the spectra start getting extremely narrow, and, as the coverage approaches saturation, there are very few points defining the peak. There is a difference of ~10 K between the simulated and the experimental spectra at lower coverage. This might be due to the presence of different phases at lower coverage, which can be investigated by XPS. The model in this case assumes, that the reaction kinetics do not differ between the different phases of the adsorbed L-Asp/Cu(110).

4.3 Conclusions

Aspartic acid undergoes autocatalytic decomposition on Cu(110). At saturation coverage, aspartic acid is present on the surface in the form of biaspartate species, $OOC^4–C^3H_2–C^2H(NH_2)–C^1OO$, in which both the acid groups have deprotonated to form carboxylate moieties. During the decomposition process, the $C^3–C^4$ bond ruptures first, resulting in the formation of C^4O2 and an intermediate species, C^3H_2-C^2HNH_2-C^1OO, that is comprised of C^1, C^2 and C^3 atoms. This intermediate species further decomposes to give CO_2, H_2 and C_2H_3N. Experimental data obtained for variable initial coverage, variable heating rate and isothermal TPRS experiments, while monitoring C^4O_2 desorption is in excellent agreement with a rate law model of the form $r_A = -\frac{d\theta^{Asp}}{dt} = k_i\theta^{Asp} + k_e\theta^{Asp}(1-\theta^{Asp})^2$. This model explicitly accounts for an initiation step and an explosion step which is second order in vacancy concentration.

Chapter 5

Super-enantiospecific surface explosions of tartaric acid on Cu(*hkl*)$^{R\&S}$ surfaces

5.1 Introduction

5.*1.1* *Surface explosions*

The previous chapters focused on the kinetics and chemistry of surface explosions on low Miller index, achiral Cu(110) surface. The primary focus of the work in the case of the TA/Cu(110) study was to investigate the initiation process which involved studying the reaction kinetics through temperature programmed reaction spectroscopy (TPRS), low energy electron diffraction (LEED) and scanning tunnel microscopy (STM). This helped us gain a molecular-level insight into the initiation of surface explosions which, until now, were largely a matter of speculation. An important feature of the surface chemistry of TA / Cu(110) is that, during heating to >400 K its decomposition proceeds via a vacancy mediated autocatalytic surface explosion. The kinetics for the explosive decomposition of TA/Cu(110) are described by a rate expression of the form[1, 103]:

$$r = k_i\theta^{TA} + k_e\theta^{TA}(1 - \theta^{TA})^2 \qquad \ldots\ldots (5.1)$$

where the first term describes a first-order nucleation process and the second term describes the vacancy mediated explosive decomposition. The main objective of the Asp/Cu(110) study was to investigate the surface chemistry of a species undergoing autocatalytic decomposition. From this study, we were able to use

isotopic labeling to identify the particular atoms and groups contributing towards specific products of the reaction.

5.1.2 Naturally chiral Cu(hkl)$^{R\&S}$ surfaces

This chapter focuses on the primary purpose of our work on surface explosions which is to exploit this mechanism to attain high enantiospecificity on chiral Cu(*hkl*)$^{R\&S}$ surfaces. Gellman and co-workers pioneered the concept and use of naturally chiral Cu(*hkl*)$^{R\&S}$ surfaces for enantiospecific surface chemistry. Using R-3-methylcyclohexanone (R-3-MCHO) [24, 53-55], R-2-bromobutane [56], S-1-bromo-2-methylbutane [57], R- and S-propylene oxides [56, 58], it was demonstrated that these surfaces are capable of chiral recognition at the molecular level.

Let us consider the example of R-3-MCHO/Cu(643)$^{R\&S}$ surfaces. Cu(643)$^{R\&S}$ surfaces are comprised of (111) terraces, (100) steps and (110) kinks [59]. Figure 5.2 illustrates the TPD spectra of R-3-MCHO on Cu(643)$^{R\&S}$, with three characteristic peaks at ~ 225 K, ~340 K and ~385 K, corresponding to desorption of R-3-MCHO from terraces, steps and kinks, respectively [24, 59]. On comparing the spectra from Cu(643)^{R} and Cu(643)^{S} surfaces, the desorption peak corresponding to the kinks shows an enantiospecific separation of ~ 3.5 K. However, since the width of the peaks at half maximum (FWHM) is around 25 K, the two peaks cannot be well resolved, and the enantiospecific difference is small.

5.1.3 Detection and measurement of enantiospecificity

In heterogeneous catalysis, the terms ‘enantiospecificity’ and ‘enantioselectivity’ are often used interchangeably, which is not appropriate.

Enantiospecificity is a measure of a difference between the chemical properties of two enantiomers, such as energies, rates (at specific temperature), rate constants (at specific temperature), etc. The enantiospecific properties of a reaction are responsible for the enantioselectivity of the process. However, these properties are independent of the process. Enantioselectivity on the other hand, is a property that is dependent on the process. We can perform enantiospecific chemical processes to obtain a non-racemic mixture of enantiomers. Enantioselectivity of the overall reaction towards a given product (*x*) can then be defined in terms of the yields of 'R' and 'S' enantiomers as:

$$ES_x^R = \frac{Y_x^R}{Y_x^S} \;\&\; ES_x^S = \frac{Y_x^S}{Y_x^R}$$

The enantiometric excess, which does not get defined differently for R and S enantiomers, can then be calculated as:

$$ee_x = \left|\frac{1 - ES_x}{1 + ES_x}\right| = \left|\frac{Y_x^R - Y_x^S}{Y_x^R + Y_x^S}\right|$$

With reference to the TPD spectra in Figure 5.2, let us consider two ways to define 'enantiospecificity' for desorption of R-3-MCHO from Cu(643)$^{R\&S}$. The first one can be referred to as the resolution factor enantiospecificity (or simply resolution factor) '*RF'*, and can be defined as the ratio of the enantiospecific peak shift, ΔT_p^{RS}, to the FWHM, ΔT_{FWHM}. In the case of R-3-MCHO/Cu(643)$^{R\&S}$, $RF^{RS} = \Delta T_p^{RS}/\Delta T_{FWHM} = 0.14$. Another way to estimate enantiospecific differences can be to determine the ratio of the reaction rates, or in this case, the ratio of the desorption rates at a particular temperature. We will refer to this as rate enantiospecificity 'ES_T^{RS}', where $ES_T^{RS} = r_R^D/r_S^D$ at temperature *T*. In this

chapter, unless otherwise mentioned, we will be calculating this ratio at the lower peak temperature 'T_p' of the two TPD spectra being considered. For R-3-MCHO/Cu(643)$^{R\&S}$ the value of rate enantiospecificity is $ES^{RS}_{385\,K} = r^D_R / r^D_S = 1.08$.

5.2 Super-enantiospecific decomposition of TA on Cu(*hkl*)$^{R\&S}$ surfaces

5.2.1 Hypothesis

With reference to the TPD spectra in Figure 5.2, in order to observe highly enantiospecific kinetics we must achieve either a larger separation between the two peaks (i.e. larger value of ΔT_p^{RS}) or reduce the width of the peaks (i.e. smaller value of ΔT_{FWHM}), or both. In each case, one would be aiming to achieve a greater resolution between the two TPD spectra which would be an indication of greater enantiospecificity.

Our hypothesis was that the interaction of chiral TA enantiomers with chiral Cu(643)$^{R\&S}$ surfaces will be enantiospecific, resulting in peak shift ΔT_p^{RS} between the two TPR spectra. Also, if the decomposition is via a vacancy mediated autocatalytic process similar to TA/Cu(110), the reaction should occur over a narrow temperature range, resulting in narrow TPR spectra. Consequently, the two peaks would be well resolved, indicating high enantiospecificity. Many discussions of surface explosion reactions assume that initiation/nucleation of the reaction occurs at the defects on the surface. Therefore, it was not clear whether TA decomposition on a surface such as Cu(643) would occur via an explosive mechanism because the density of the defects on the surface is roughly equivalent to the absolute TA coverage. In chapter 3, we discussed the observation of

explosive kinetics during isothermal TPR spectra obtained for TA decomposition on $Cu(651)^{S}$ surface. The result indicated that surface defects are not responsible for the initiation of surface explosion. The decomposition kinetics of TA on $Cu(643)^{R\&S}$, $Cu(17,5,1)^{R\&S}$ and $Cu(531)^{R\&S}$ further confirm our analysis.

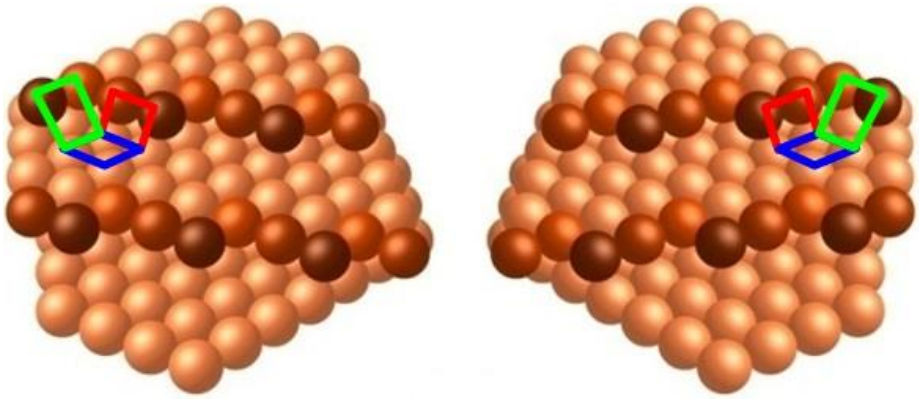

Cu(643)^{S} **Cu(643)^{R}**

Figure 5.1 Cu(643)$^{R\&S}$ surfaces are chiral and have a characteristic structure comprising of terraces, steps and kinks. The step edges are formed by the intersections of (111) terraces, (100) steps and (110) kinks. Kinks are the features on the surface that impart it with its characteristic chirality. The direction from the most close-packed (111) plane to the (100) plane to the least close-packed (110) plane dictates the handedness of the surface: counterclockwise rotation is denoted as S and clockwise rotation is denoted as R.

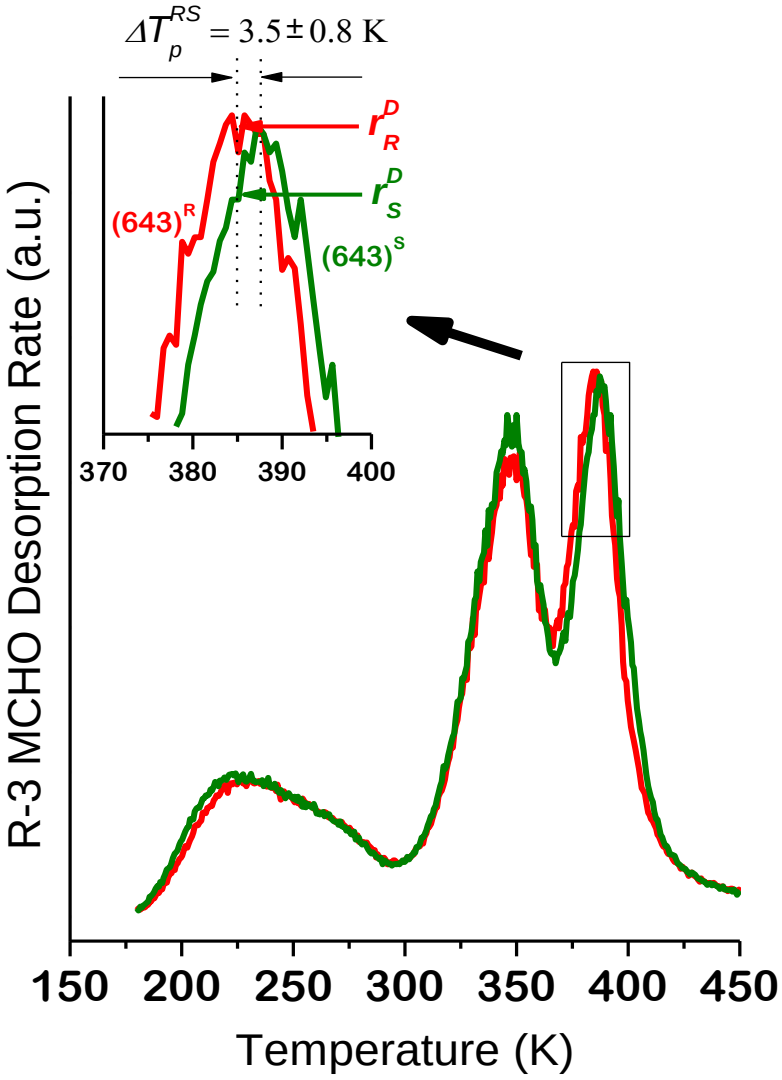

Figure 5.2 TPD spectra of R-3-MCHO on Cu(643)$^{R\&S}$ shows three characteristic peaks at 225 K, 340 K and 385 K, corresponding to the desorption of R-3-MCHO from terraces, steps and kinks, respectively. The inset shows R-3-MCHO desorption from the kinks on Cu(643)$^{R\&S}$ surfaces. The enantiospecific difference in the peak desorption temperature from the kinks on these two surfaces is ΔT_p = 3.5 ± 0.8 K. The resolution factor between the two spectra is $RF^{RS} = \Delta T_p^{RS} / \Delta T_{FWHM} = 0.14$ while the enantiospecificity in the rate at 385 K is $ES_{385\,K}^{RS} = r_R^D / r_S^D = 1.08$.

5.2.2 TA decomposition on Cu(643)$^{R\&S}$ surfaces

As illustrated in Figure 5.3, the TPR spectra of D-TA/Cu(643)^{R} exhibits two characteristics of explosive decomposition. The peak temperature 'T_p' shifts from 430 K at low coverage to 496 K at saturation coverage (i.e. $\theta_0^{TA} = 1$) with a peak width of ΔT_p = 3.5 K at saturation. The peak widths in case of TA/Cu(643)^{R} are always greater than those for TA/Cu(110). This probably arises from the heterogeneity in the local surface structure that results from thermal roughening [116]. Figure 5.4 depicts the TPR spectra of D-TA/Cu(643)^{S} which shows similar widths and relative peak-shifts as D-TA/Cu(643)^{R}, with the main difference being that the peak temperature 'T_p' shifts from around 430 K at low coverage to 486 K at saturation (i.e. $\theta_0^{TA} = 1$). The key observation of the TA/Cu(643)$^{R\&S}$ study is illustrated in Figure 5.5 which compares the TPR spectra of D-TA at saturation coverage on Cu(643)$^{R\&S}$ surfaces. As per our hypothesis, the two spectra are well resolved indicating highly enantiospecific kinetics. From our definitions of enantiospecificity, the resolution factor in this case is $RF^{RS} = \Delta T_p^{RS}/\Delta T_{FWHM} =$ 2.86 which is ~20 times higher than that observed in the case of R-3-MCHO/Cu(643)$^{R\&S}$. The rate enantiospecificity is $ES_{486\,K}^{RS} = r_R^D/r_S^D =$ 47, which is ~40 times that observed in the case of R-3-MCHO / Cu(643)$^{R\&S}$. The initial coverages in Figure 5.3 and Figure 5.4 were determined using XPS. The coverage determination calculations are included in Appendix VIII. Based on these coverages, we can plot the variation of the resolution factor *RF* as a function of coverage as depicted in the lower section of Figure 5.6. This plot illustrates the resolution between the two peaks on Cu(643)$^{R\&S}$ surfaces at various coverages.

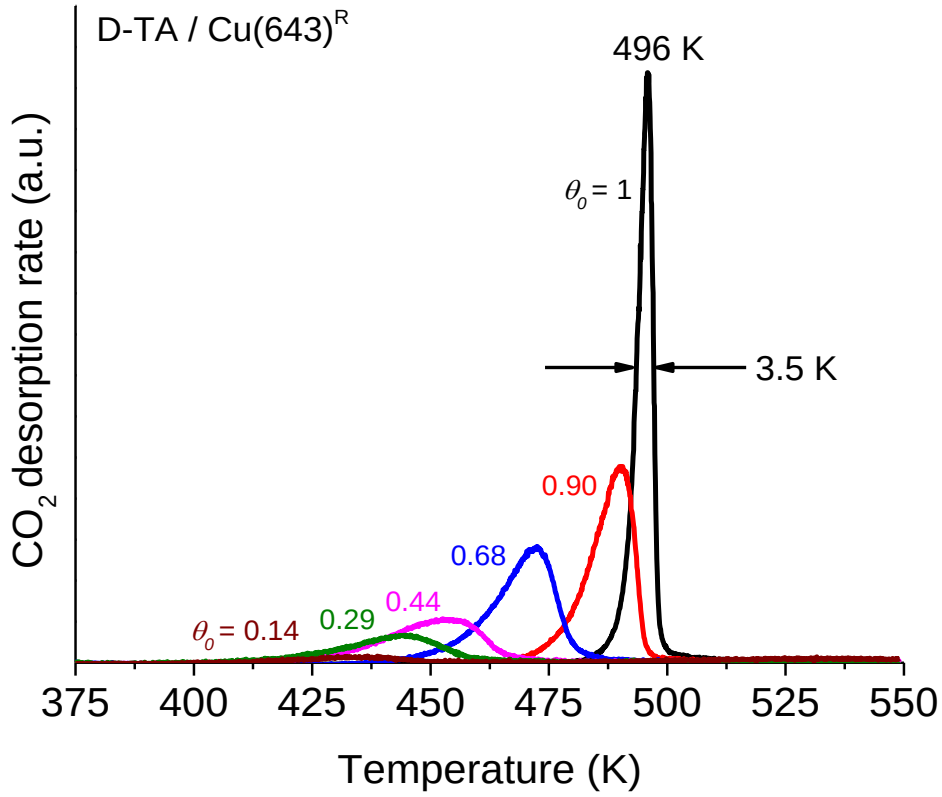

Figure 5.3 TPR spectra of D-TA on the Cu(643)^{R} surface at varying initial coverage of TA on the surface i.e. varying θ_0^{TA}. As the initial coverage increases, the peak decomposition temperature increases and the width of the spectra decreases. At saturation coverage i.e. θ_0^{TA} = 1, the TPR spectra has a peak desorption temperature of T_p = 496 K and a FWHM of only ΔT_{FWHM} = 3.5 K. The spectral shifts and extraordinarily narrow peak at saturation are characteristic indicators of surface explosion.

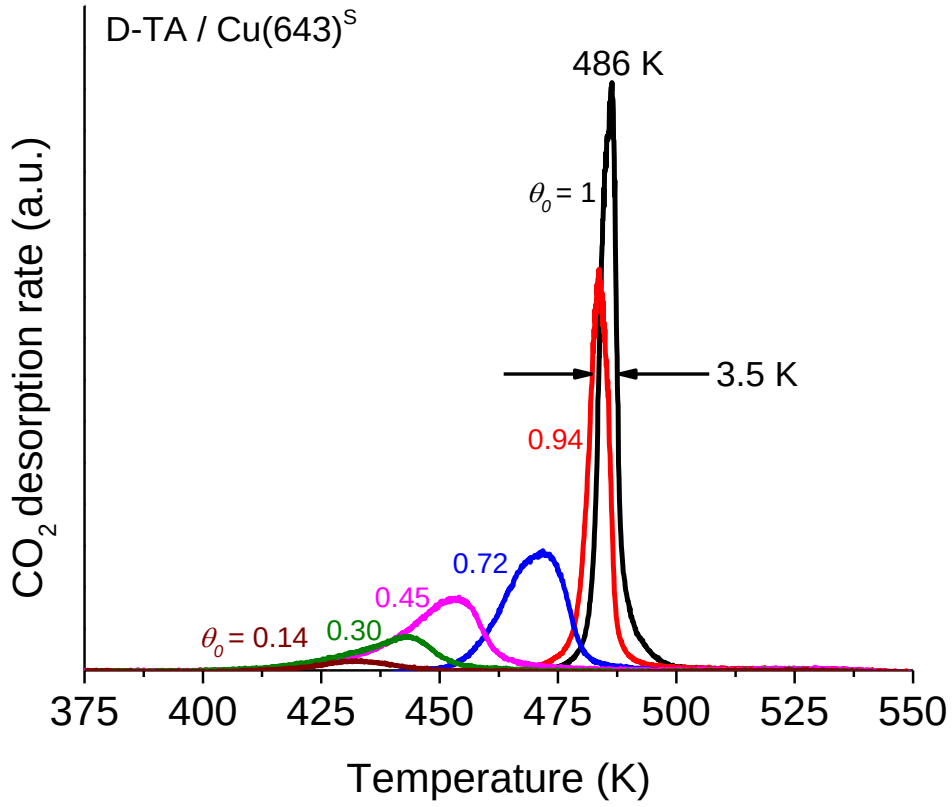

Figure 5.4 TPR spectra of D-TA on the Cu(643)^S surface at varying initial coverage of D-TA on the surface i.e. varying θ_0^{TA}. As the initial coverage increases, the peak decomposition temperature increases and the width of the spectra decreases. At saturation coverage i.e. θ_0^{TA} = 1, the TPR spectra has a peak desorption temperature of T_p = 486 K and a FWHM of only ΔT_{FWHM} = 3.5 K. The spectral shifts and extraordinarily narrow peak at saturation are characteristic indicators of surface explosion.

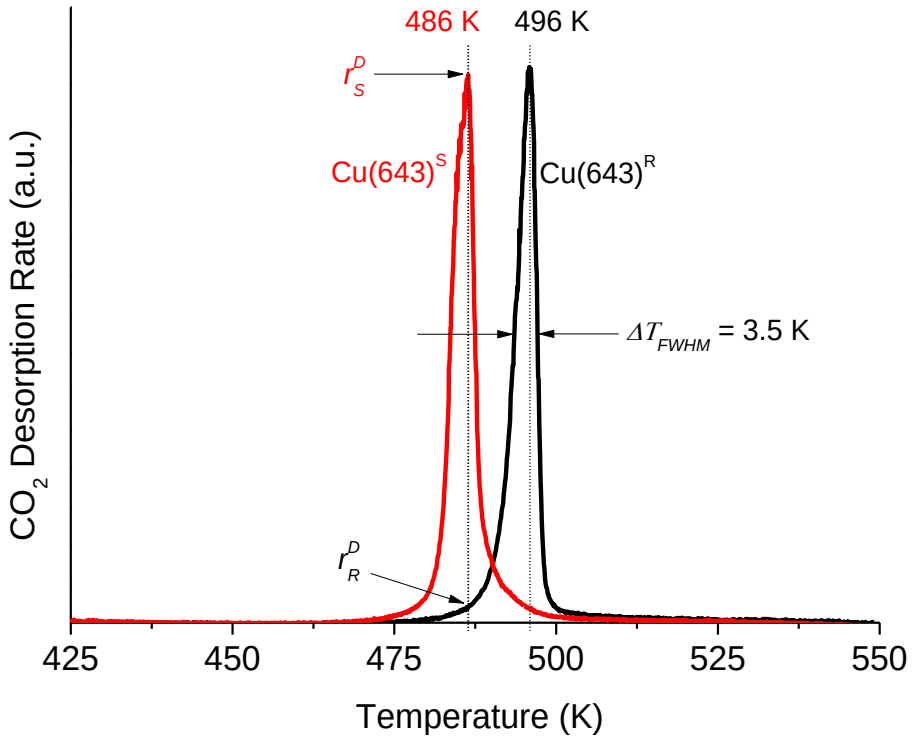

Figure 5.5 The figure illustrates the TPR spectra of D-TA on Cu(643)$^{R\&S}$ surfaces at saturation coverage, θ_0^{TA} = 1. The two peaks are separated by ΔT_p = 10 K and have a narrow width of ΔT_{FWHM} = 3.5 K. These spectra reveal highly enantiospecific kinetics with a resolution factor of around $RF^{RS} = \Delta T_p^{RS}/\Delta T_{FWHM} = 2.8$ and a rate enantiospecificity of around $ES_{486\,K}^{RS} = r_R^D/r_S^D = 47$.

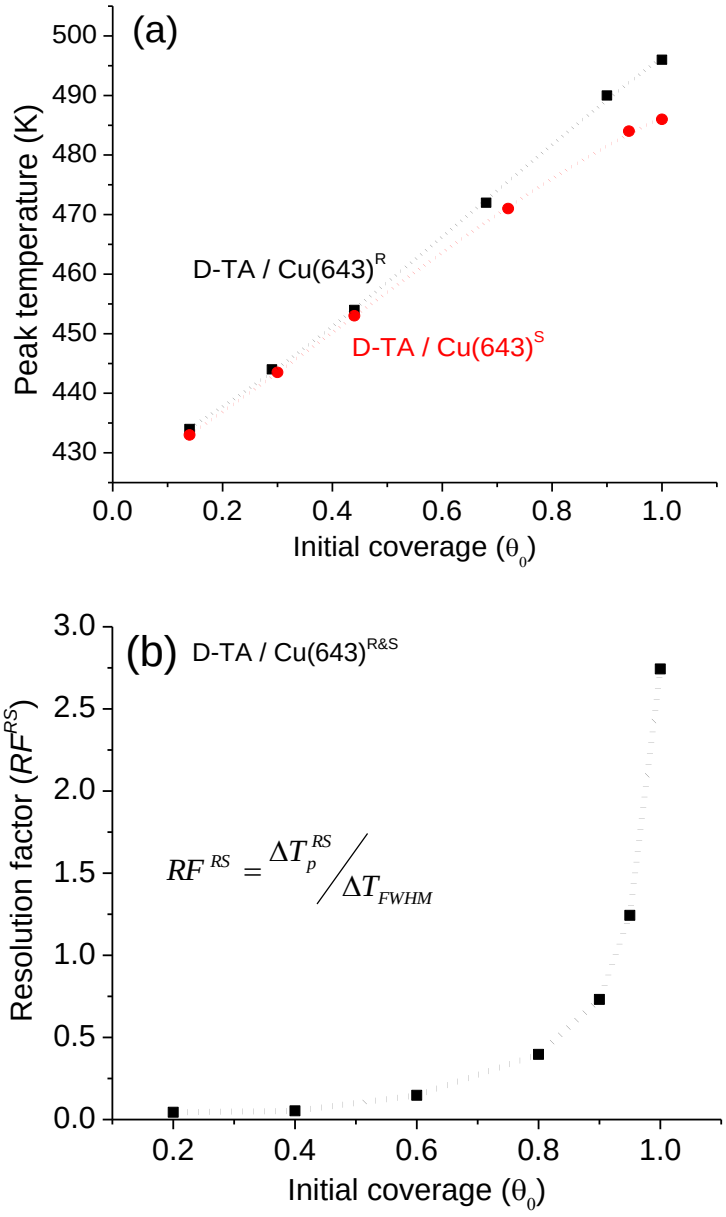

Figure 5.6 (a) Enantiospecific variation of peak temperature as a function of initial surface coverage θ_0 in the case of D-TA/Cu(643)$^{R\&S}$. As θ_0^{TA} increases, the difference between the peak temperature increases. (b) Variation of the resolution factor $RF^{RS} = \Delta T_p^{RS}/\Delta T_{FWHM}$ as a function of θ_0 in case of D-TA/ Cu(643)$^{R\&S}$. As θ_0^{TA} increases, the resolution between the TPR spectra increases.

5.2.3 TA decomposition on Cu(17,5,1)$^{R\&S}$ and Cu(531)$^{R\&S}$ surfaces

The explosive kinetics and extraordinarily high enantiospecificity of TA decomposition appears to hold true in the case of all chiral Cu(*hkl*)$^{R\&S}$ surfaces. Figure 5.7 illustrates ideal chiral Cu(17,5,1)$^{R\&S}$ surfaces and the TPR spectra for the decomposition of D- and L- TA on these surfaces at saturation coverage. The structure of Cu(17,5,1) differs from that of Cu(643) in that, the terraces, steps and kinks are formed from the (100), (110) and (111) microfacets, respectively. The TA decomposition kinetics on Cu(17,5,1)$^{R\&S}$ are highly enantiospecific with a resolution factor of $RF^{RS} = \Delta T_p^{RS}/\Delta T_{FWHM} = 2.14$, while the rate enantiospecificity is $ES^{RS}_{493.5\,K} = r_R^D/r_S^D = 17$. Another important point to note from Figure 5.7 is that the kinetics exhibit true diastereomerism since, $T_p^{L/R} = T_p^{D/S} > T_p^{L/S} = T_p^{D/R}$, proving that the origin of these phenomena lies in the relative handedness of the TA and the Cu surfaces.

Figure 5.7 illustrates ideal chiral Cu(531)$^{R\&S}$ surfaces and the TPR spectra for the decomposition of D- and L- TA on these surfaces at saturation coverage. In the context of our experiments, the structure of Cu(531) is a special one, since it is the 'most chiral' surface that can be derived from the fcc structure. Since all the terraces and steps are one lattice spacing in width, Cu(531) surface has the highest kink density of all fcc (*hkl*) metal surfaces. The TA decomposition kinetics on Cu(531)$^{R\&S}$ are highly enantiospecific with a resolution factor of around $RF^{RS} = \Delta T_p^{RS}/\Delta T_{FWHM} = 2.5$, while the rate enantiospecificity is around $ES^{RS}_{489.8\,K} = r_R^D/r_S^D = 20$. Again, TA decomposition kinetics on Cu(531)$^{R\&S}$

exhibit true diastereomerism since, $T_p^{D/R} = T_p^{L/S} > T_p^{D/S} = T_p^{L/R}$, indicating that the observed differences are truly due to enantiospecific interactions.

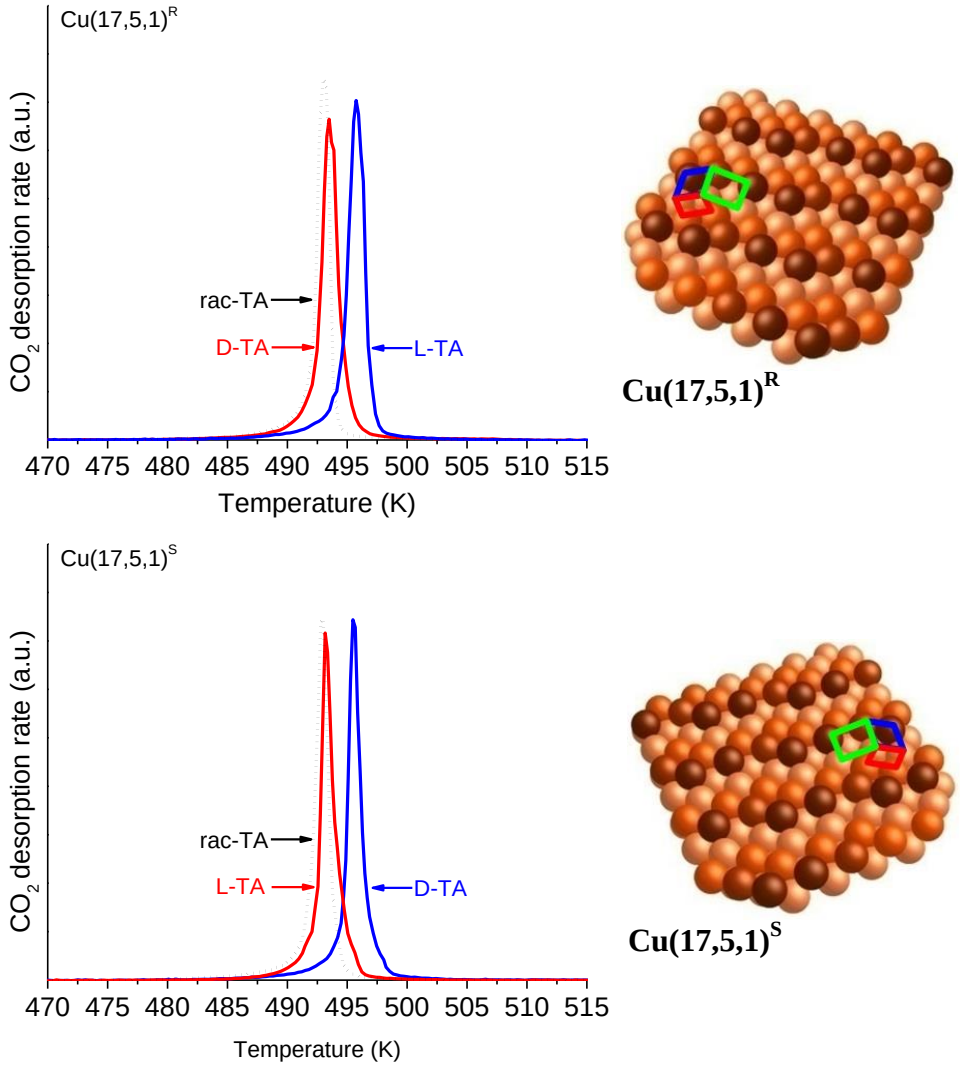

Figure 5.7 The figure illustrates the TPR spectra of D-, L- and rac-TA on Cu(17,5,1)^{R} surface in the top section and on Cu(17,5,1)^{S} surface in the bottom section. These spectra reveal highly enantiospecific kinetics with a resolution factor of around $RF^{RS} = \Delta T_p^{RS}/\Delta T_{FWHM} = 2.14$ and the rate enantiospecificity of around $ES_{493.5\,K}^{RS} = r_R^D/r_S^D = 17$. Also, the kinetics exhibit true diastereomerism since,$T_p^{L/R} = T_p^{D/S} > T_p^{L/S} = T_p^{D/R}$, indicating that the origin of these phenomena lies in the relative handedness of the TA and the Cu surfaces. Decomposition of achiral rac-TA occurs at the same temperature on both surfaces, at the temperature of the less stable adsorbate-substrate combination, $T_p^{\mathrm{rac/S}} = T_p^{\mathrm{rac/R}} = T_p^{\mathrm{D/R}} = T_p^{\mathrm{L/S}}$. TA/Cu(651)^{S} experiments were performed by Pushkarev and these figures are adopted from his thesis [2].

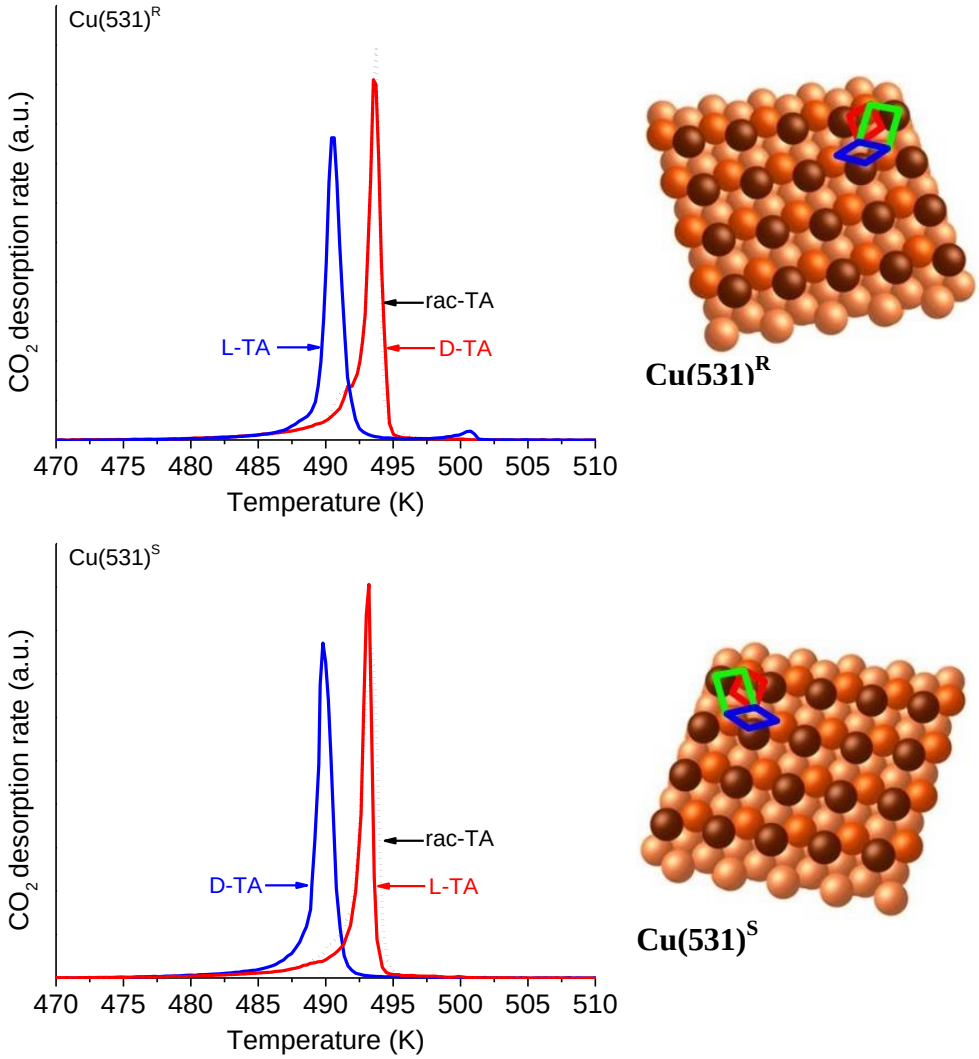

Figure 5.8 The figure illustrates the TPR spectra of D-, L- and rac-TA on Cu(531)^{R} surface in the top section and on Cu(531)^{S} surface in the bottom section. These spectra reveal highly enantiospecific kinetics with a resolution factor of around $RF^{RS} = \Delta T_p^{RS}/\Delta T_{FWHM} = 2.5$ and the rate enantiospecificity of around $ES_{489.8\,K}^{RS} = r_R^D/r_S^D = 20$. Also the kinetics exhibit true diastereomerism, however the order of stability is reversed from that on Cu(17,5,1)$^{R\&S}$ since, $T_p^{D/R} = T_p^{L/S} > T_p^{D/S} = T_p^{L/R}$. Decomposition of achiral rac-TA occurs at the same temperature on both surfaces, but at the temperature of the more stable adsorbate-substrate combination, $T_p^{\mathrm{rac/S}} = T_p^{\mathrm{rac/R}} = T_p^{\mathrm{L/R}} = T_p^{\mathrm{D/S}}$. TA/Cu(651)^{S} experiments were performed by Pushkarev and these figures are adopted from his thesis [2].

5.2.4 Rac-TA decomposition on Cu(17,5,1)$^{R\&S}$ and Cu(531)$^{R\&S}$ surfaces

In the sections 5.2.2 and 5.2.3, we discussed enantiospecific decomposition of pure TA enantiomers on chiral Cu(*hkl*)$^{R\&S}$ surfaces. Racemic TA (rac-TA) should exhibit identical decomposition characteristics on Cu(*hkl*)$^{R\&S}$ surfaces. Adsorption of rac-TA on chiral Cu surfaces ought to give one of two possible outcomes: rac-TA separating into homochiral domains, or the formation of a heterochiral racemate structure. In this case, the decomposition ought to occur at the lower of the two decomposition temperatures, as the less stable enantiomers should result in vacancy formation and autocatalytic explosion should then result in rapid decomposition of both the enantiomers [96]. The dotted lines in Figures 5.7 and 5.8 represent the TPR spectra for the decomposition of rac-TA on Cu(17,5,1)$^{R\&S}$ and Cu(531)$^{R\&S}$, respectively. For both the surfaces, it is evident that $T_p^{rac/R} = T_p^{rac/S}$, and this is a reflection of the fact that rac-TA is achiral. On Cu(17,5,1)$^{R\&S}$ the decomposition of the adsorbed TA occurs at the lower of the two decomposition temperatures observed for the enantiomerically pure TA: $T_p^{rac/R} = T_p^{rac/S} = T_p^{D/R} = T_p^{L/S}$. In contrast to Cu(17,5,1)$^{R\&S}$, rac-TA on Cu(531)$^{R\&S}$ decomposes at the temperature of the more stable pure enantiomer: $T_p^{rac/R} = T_p^{rac/S} = T_p^{L/R} = T_p^{D/S}$.

Our interpretation of this result is that, exposure of the chiral Cu surfaces to rac-TA does not result in the adsorption of a racemic mixture on the surface. Because the surfaces are chiral, one of the two enantiomers will be preferentially adsorbed from the gas phase, yielding an enantiomerically enriched adsorbed layer; in this case, enriched in L-TA on Cu(531)^{S} and D-TA on Cu(531)^{R}.

Although there are no means to verify this without isotopically labeled TA, racemic aspartic acid (HO_2C-$CH(NH_2)$-CH_2-CO_2H) in which the L-Asp is labeled with ^{13}C, has shown enantiomeric enrichment during exposure to chiral $Cu(3,1,17)^{R\&S}$ surfaces [117].

5.2.5 Isothermal TA decomposition on $Cu(651)^{R\&S}$ surfaces

Another signature feature of surface explosion reaction is that, at constant temperature, the reaction rate accelerates with the extent of reaction [1, 103]. We studied this phenomenon in detail in the case of TA/Cu(110) and also with Asp/Cu(110). Figure 5.9 illustrates the TPR spectra of D- and L-TA on $Cu(651)^{R\&S}$ obtained at various isothermal temperatures 'T_{iso}' between 450 – 470 K, while monitoring the CO_2 desorption rate as a function of lag time after reaching T_{iso}. The isothermal decomposition experiments for TA/$Cu(651)^{R\&S}$ were performed by Brian Holsclaw. As depicted in Figure 5.9, the Cu(651) surface has a structure in which the terraces, steps and kinks are formed from (110), (111) and (100) microfacets, respectively. As expected, during the decomposition process, there is an initiation period during which there is no observable desorption of CO_2. Slow nucleation of vacancies reduces θ^{TA} until the autocatalytic decomposition begins to dominate, and rapid acceleration of the reaction depletes the adsorbed TA.

Figure 5.10 shows a plot of peak reaction times t_p versus isothermal temperatures T_{iso} for D- and L-TA on $Cu(651)^{S}$ surfaces. In the plot the black and blue spots are derived from the experimental data. The green and orange curves represent the fit of t_p versus T_{iso}, as estimated using the rate expression in eq. 5.1

and parameters i.e. A_i, A_e, ΔE_i and ΔE_e, in the Table 5.1. The parameters have been adopted from Holsclaw's thesis. The parameter estimation approach here, searched for the values of ln(A_i), ln(A_e), ΔE_i and ΔE_e, that minimized the differences between the predicted and the measured values of peak times t_p. It is evident that the experimental and the simulated values are in close agreement. Figure 5.10 also illustrates the enantiospecific variation between the peak temperature times for D- and L-TA on Cu(651)$^{R\&S}$ as a function of isothermal temperature T_{iso}.

5.2.6 Kinetic interpretation of k_{eff} for explosive decomposition of TA/Cu(hkl)$^{R\&S}$ surfaces

The overall kinetics for the explosive decomposition of TA/Cu(110) are described by a rate expression of the form given by eqn. 5.1

$$r = k_i \theta^{TA} + k_e \theta^{TA} \left(1 - \theta^{TA}\right)^2$$

This rate law (eqn. 5.1) for the explosive decomposition of TA/Cu(*hkl*) has been determined from modeling of kinetic data obtained for decomposition of D-TA/Cu(110) using initial coverages in the range θ_0^{TA} = 0.18 → 1.0, heating rates in the range β = 0.25 – 4.0 K/sec and isothermal decomposition at temperatures in the range T_{iso} = 440 – 470 K [103]. The rate law describes a slow initiation process that creates vacancies which, once they reach a critical value, lead to explosive decomposition of TA.

The rate law defines a critical TA coverage, θ_c^{TA} or a critical vacancy coverage, $\theta_c^{vac} = \left(1 - \theta_c^{TA}\right)$, at which the rate of the explosion process becomes equal to the rate of nucleation process.

$$\theta_c^{TA} = \left(1 - \sqrt{k_i / k_e}\right) \qquad \text{..... (5.2)}$$

This also defines a critical time, t_c, to reach θ_c^{TA} from $\theta_0^{TA} = 1$. The initiation gives a first-order decay such that $\theta^{TA} = exp(-k_i t) \approx (1 - k_i t)$ and the critical reaction time is $t_c \approx (k_i k_e)^{-1/2}$.

The second regime of the reaction is the explosive decomposition that dominates the reaction rate for $t > t_c$. In this regime the rate of depletion of adsorbed TA is given by

$$\frac{d\theta^{TA}}{dt} = -k_e \theta^{TA} \left(1 - \theta^{TA}\right)^2 \qquad \text{..... (5.3)}$$

With this rate law, the peak decomposition rate occurs at a TA coverage of $\theta_p^{TA} = 1/3$. The time to reach the peak in the TA decomposition rate, as measured in the isothermal TPR experiment is given by the critical time, t_c, for the coverage to drop from $\theta_0^{TA} = 1$ to $\theta_c^{TA} = \left(1 - \sqrt{k_i / k_e}\right)$ as determined by the initiation process, plus the time for the coverage to drop from θ_c^{TA} to $\theta_p^{TA} = 1/3$ as determined by the explosion process. Using the rate law given in eqn. 5.3 above, the time for the coverage to drop from θ_c^{TA} to $\theta_p^{TA} = 1/3$ is given by

$$\begin{aligned} t_p - t_c &= -k_e^{-1} \int_{\theta_c^{TA}}^{\theta_p^{TA}} \frac{d\theta}{\theta(1-\theta)^2} \\ &= -k_e^{-1} \left[\frac{1}{1-\theta} - \ln(\theta - 1) + \ln\theta \right] \Bigg|_{\theta_c^{TA}}^{\theta_p^{TA}} \end{aligned} \qquad \text{..... (5.4)}$$

which can be evaluated to yield

$$\begin{aligned} t_p &= \frac{2}{\sqrt{k_i k_e}} - \frac{1}{k_e} \left[\frac{3}{2} + \ln\left(\frac{\sqrt{k_i k_e}}{2\left(\sqrt{k_e} - \sqrt{k_i}\right)} \right) \right] \\ &\approx \frac{2}{\sqrt{k_i k_e}} \end{aligned} \qquad \text{..... (5.5)}$$

for $k_e >> k_i$. The peak reaction time can then be used to define an effective rate constant for TA decomposition on Cu surfaces,

$$k_{eff} = t_p^{-1} = \frac{1}{2}\sqrt{k_i k_e} \qquad \text{..... (5.6)}$$

Figure 5.11 depicts a plot of $ln(t_p^{-1})$ versus $(-1/RT)$ corresponding to each spectra from the data in Figure 5.9 . The plot is linear, the slope of which yields the effective barrier $\Delta E_{eff} = (\Delta E_i + \Delta E_e)/2$, derived from the two rate constants k_i and k_e. The enantiospecific difference between the effective barriers is $\Delta\Delta E_{eff} = \Delta E_{eff}^{D/S} - \Delta E_{eff}^{L/S}$ as estimated from TA/Cu(651)^S data, is not significantly different from zero. In spite of this, the non-linear nature of the explosive decomposition kinetics leads to highly enantiospecific reaction rates, based on the relatively small enantiospecific differences in relative rate constants.

Table 5.1 Kinetic parameters estimated* for the explosive decomposition of D- and L-TA/Cu(651)^S using eq. 5.1

	A_i (sec^{-1})	ΔE_i (kJ/mol)	A_e (sec^{-1})	ΔE_e (kJ/mol)
D-TA/Cu(651)^S	3.08 x 10^{17}	191.1	5.73 x 10^{13}	121.8
L-TA/Cu(651)^S	3.08 x 10^{17}	191.1	5.73 x 10^{13}	119.3

* Parameter estimation by minimization of $\sum \left(x_{expt} - x_{model}\right)^2 / x_{expt}^2$ where *x* is the peak time for the isothermal heating TPRS data in Figures 5.9.

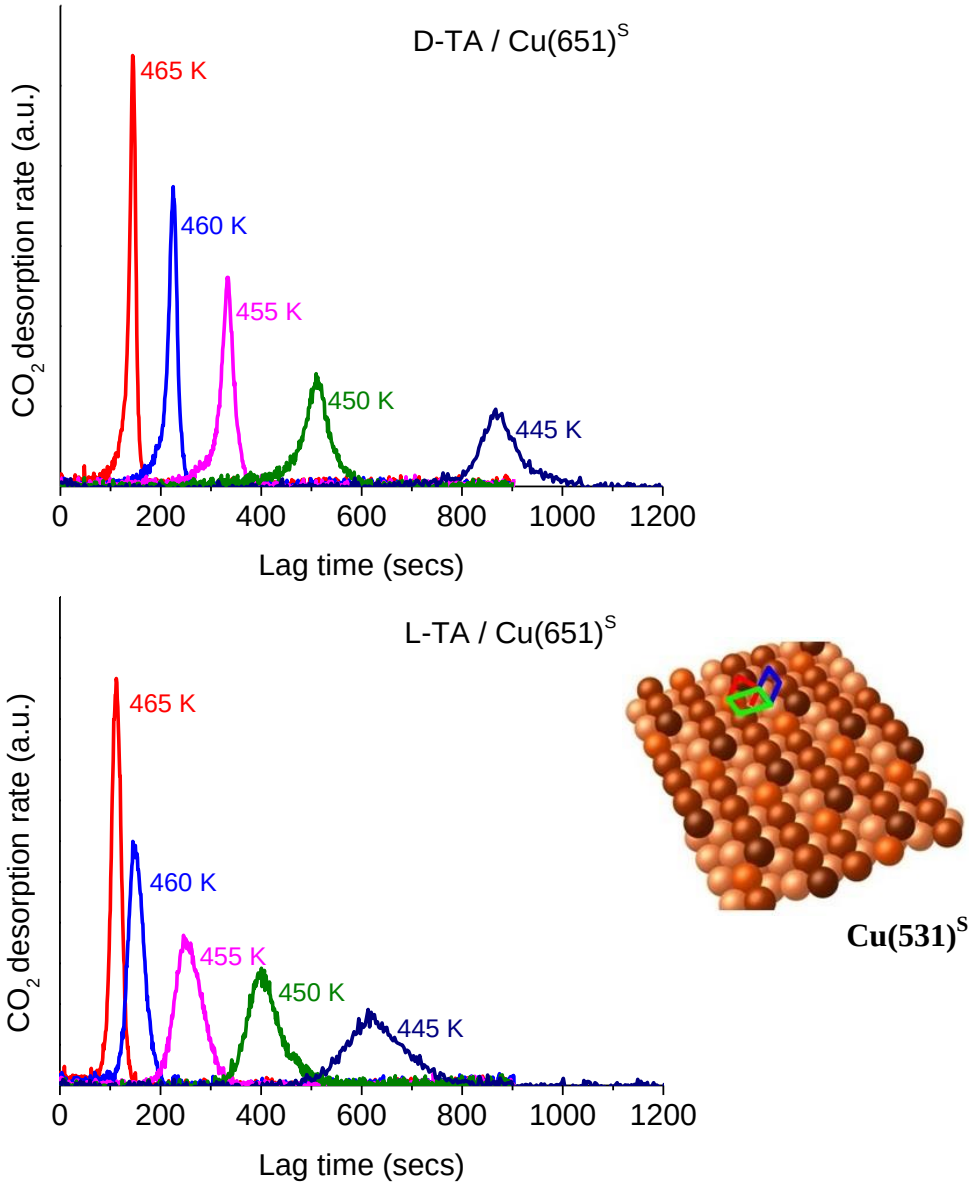

Figure 5.9 The figure illustrates isothermal decomposition TPR spectra of D-TA (upper section) and L-TA (lower section) at saturation coverage i.e. θ_0 = 1 on Cu(651)^S (structure as inset in the lower section). The explosive decomposition is characterized an induction period during which there is no observable desorption of CO_2. Slow nucleation of vacancies reduces θ^{TA} until the autocatalytic decomposition begins to dominate and rapid acceleration of the reaction depletes the adsorbed TA. Enantiospecificity is manifested by the dependence of the reaction time, t_p, on the relative chirality of the L-TA and D-TA and the Cu(651)^S surface. TA/Cu(651)^S experiments were performed by Holsclaw and this figure is adopted from his thesis [1].

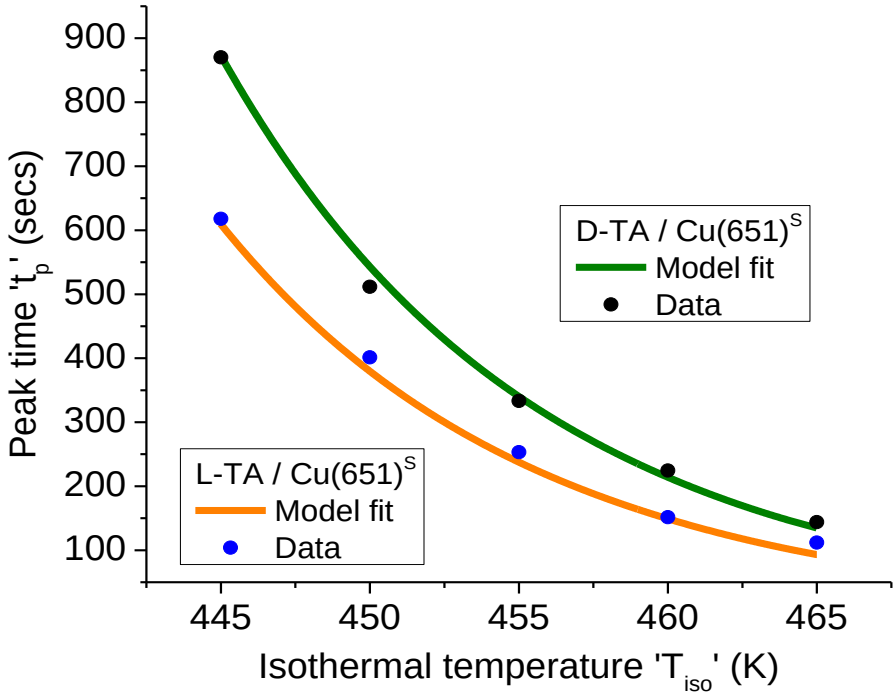

Figure 5.10 Comparison between the plot of peak times t_p at various isothermal temperatures T_{iso} for D- and L-TA on Cu(651)^S surfaces from experimental data and the t_p estimated by the model fits using the rate expression in eq. 5.1 and parameters i.e. A_i, A_e, ΔE_i and ΔE_e, in the Table 5.1. It is evident that the experimental and the simulated values are in close agreement. The figure directly illustrates the enantiospecific variation between the peak temperature times for D- and L-TA on Cu(651)$^{R\&S}$ as a function of T_{iso}.

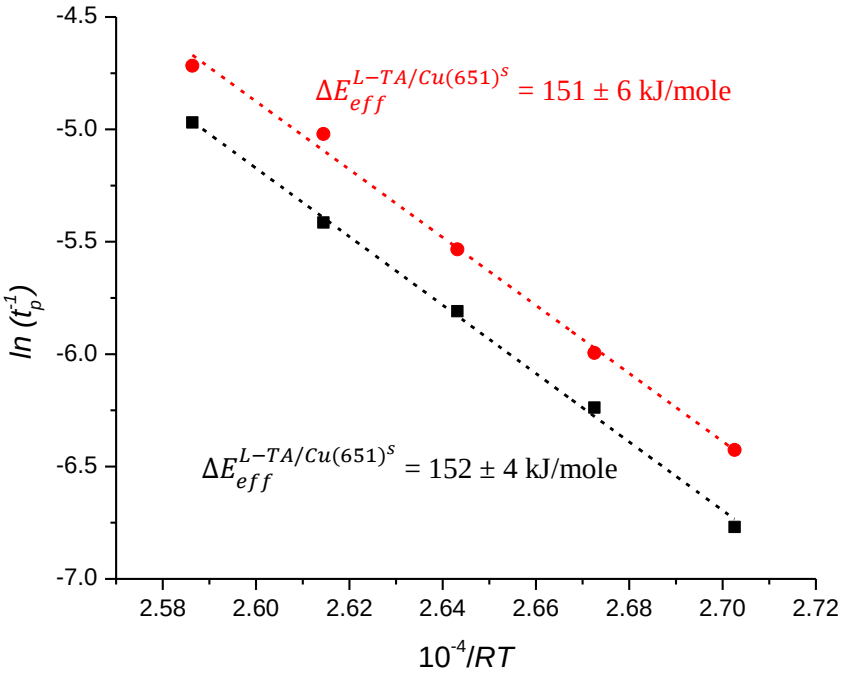

Figure 5.11 Plot of $ln(t_p)$ versus T_{iso}^{-1}, where t_p is the peak time corresponding to isothermal temperature T_{iso} and $t_p^{-1} = k_{eff} = \sqrt{k_n k_e}$. The slope yields the effective barriers for D- and L-TA decomposition on Cu(651)^S surface $\Delta E_{eff} = (\Delta E_i + \Delta E_e)/2$, derived from the two rate constants k_i and k_e. The enantiospecific difference between the effective barriers $\Delta\Delta E_{eff} = \Delta E_{eff}^{D/S} - \Delta E_{eff}^{L/S}$ is not significantly different from zero.

5.3 Conclusions

We have observed that the explosive decomposition of L-TA and D-TA on several naturally chiral, Cu(*hkl*)$^{R\&S}$ single crystal surfaces can exhibit enantiospecificity in reaction rates that reach factors of 50. The mechanism involves autocatalytic generation of vacancies by a mechanism that exhibits kinetics similar to those of a radical branching explosion. Also, the kinetics exhibit true diastereomerism since, ($T_p^{L/R} = T_p^{D/S}$) ≠ ($T_p^{L/S} = T_p^{D/R}$), proving that the origin of these phenomena lies in the relative handedness of the TA enantiomers and the Cu(*hkl*)$^{R\&S}$ surfaces. An interesting point to note is the fact that the energy difference between the decomposition barriers $\Delta\Delta E$ is of a similar magnitude to other enantiospecific processes on naturally chiral surfaces but it is the non-linear nature of the rate law that leads to extremely high enantiospecificity in the reaction rates. Overall, the phenomenon exhibits characteristics similar to those of autocatalytic processes that have been postulated to lead to biomolecular homochirality in life on Earth; processes with relatively small differences in reaction energetics that, nonetheless, lead to extremely high enantioselectivity.

Chapter 6

Conclusions and future work

This thesis presents the results from studies conducted to investigate three key aspects pertaining to surface explosion reactions. These include – the initiation of surface explosions, the mechanistic chemistry of explosive decompositions, and ultimately, exploiting this mechanism to attain high enantiospecificity on naturally chiral Cu(*hkl*) surfaces.

One of the most poorly understood aspects of surface explosions is the initiation process. The autocatalytic decomposition of tartaric acid (TA) on Cu(110), studied in this work, offers a molecular level insight into the initiation process, which until now, was largely a matter of speculation. Using TPRS, LEED and STM it was demonstrated that the explosive decomposition of TA/Cu(110) is initiated by an irreversible process that leads to a slow decrease in the coverage of TA on the surface with a subsequent formation of vacancies in the adsorbed overlayer. Using TA/Cu(651)^{S} it was identified that the initiation process is not associated with structural defects on the surface; instead it can be described simply as an irreversible initiation step in the reaction mechanism that is then followed by the explosive autocatalytic decomposition of TA. The onset of the explosive decomposition is accompanied by the appearance of Cu adatoms on the Cu(110) surface, which was observed using both LEED and by STM as a $(\pm 6,7; \mp 2,1)$ phase. Based on the TPRS data obtained during variable initial coverage, variable heating rate and isothermal heating experiments, we were able

to postulate a rate law that explicitly accounts for the initiation process as a reaction step that creates vacancies via consumption of adsorbed TA,

$$r = k_i\theta + k_e\theta(1-\theta)^n \qquad \text{….. (6.1)}$$

where k_i is the rate constant for the initiation process, k_e is the rate constant for the explosion and n defines the order of the explosion reaction with respect to the vacancy concentration.

Aspartic acid (Asp) also undergoes autocatalytic decomposition on Cu(110). A number of isotopomers of Asp are commercially available in enantiomerically pure L- form, which allowed us to conduct a detailed investigation of the surface chemistry of L-Asp decomposition on Cu(110). Using XPS, it was identified that at saturation coverage, Asp is present on the surface in the form of biaspartate species, $OOC–CH_2–CH(NH_2)–COO$, in which both the acid groups have deprotonated to form carboxylate moieties. Using isotopically labeled L-Asp while performing TPRS, it was demonstrated that during the decomposition process, the $C^3–C^4O_2$ bond ruptures first, resulting in the formation of C^4O_2 and an intermediate species, CH_2-$CH(NH_2)$-COO, that is comprised of the C^1, C^2 and C^3 atoms. This intermediate species further decomposes to give CO_2, H_2 and C_2H_3N. Experimental data obtained for variable initial coverage, variable heating rate and isothermal TPRS experiments, while monitoring C^4O_2 desorption were shown to be in excellent agreement with a rate law of the form of eqn. 6.1 which explicitly accounts for an initiation step and an explosion step which is second order in vacancy concentration.

Finally, we demonstrated that TA decomposition on Cu(*hkl*) surfaces also exhibits explosive kinetics and that the explosive mechanism can be exploited to attain extremely high enantiospecificity in the case of pure D- and L- TA enantiomers on Cu(*hkl*)$^{R\&S}$ surfaces. Also, the kinetics exhibit true diastereomerism since, ($T_p^{L/R} = T_p^{D/S}$) ≠ ($T_p^{L/S} = T_p^{D/R}$), proving that the origin of these phenomena lies in the relative handedness of the TA enantiomers and the Cu(*hkl*)$^{R\&S}$ surfaces. The energy difference between the decomposition barriers $\Delta\Delta E$ on Cu(*hkl*)$^{R\&S}$ is similar to those of other enantiospecific processes on naturally chiral surfaces but it is the non-linear nature of the rate law that leads to the very high enantiospecificity observed in the reaction rates.

Different types of TPRS experiments were performed on different Cu(*hkl*)$^{R\&S}$ surfaces i.e. variable coverage experiments were performed on Cu(643) $^{R\&S}$ surfaces, experiments using rac-TA were performed on Cu(17,5,1) $^{R\&S}$ and Cu(531) $^{R\&S}$ surfaces, whereas isothermal experiments were performed on Cu(651)$^{R\&S}$ surfaces. Of all the Cu(*hkl*)$^{R\&S}$ surfaces investigated so far, TA/Cu(643)$^{R\&S}$ demonstrates the highest enantiospecificity. Isothermal TPRS experiments are currently underway to accurately estimate the rate constants and $\Delta\Delta E$ for this system. Future experimental work will also include the study of adsorption and decomposition of TA on Cu(13,9,1)$^{R\&S}$ surfaces which consists of terraces having [110] orientation.

From the TA/Cu(*hkl*)$^{R\&S}$ experiments performed to date, it is also apparent that enantiospecificity is structure sensitive, and there ought to exist a surface with the highest enantiospecificity. Achieving control over enantioselectivity of a

process requires understanding of the factors that are enantiospecific. Since there exist an infinite number of Cu(*hkl*) surfaces, testing all possible surfaces is out of the question. Surface structure spread single crystal (S^4C) surfaces pose a viable alternative for studying the structure sensitivity of TA, Asp or for that matter any other molecule. However, for performing experiments using S^4C surfaces, newer experimental approaches need to be developed. TPRS experiments collect data for desorption from the entire surface and therefore S^4C surfaces cannot be used to collect data for modeling the reaction kinetics using regular TPRS experiments. That being said, isothermal TPRS or other experiments such as selective elimination of groups on the reacting molecule, might prove to be an excellent option for controlling the reaction rate at different points on the S^4C surfaces. While the procedures to be followed for TPRS experiments are unclear at this point of time, techniques such as XPS, which can probe small areas of the surface, can definitely be used to study adsorption and decomposition on S^4C surfaces. The results from such experiments would be useful in determining suitable substrate-adsorbate systems to be further investigated in detail. Overall, the work done in this thesis lays the foundation for approaches such as these to be followed.

References

1. Holsclaw, B., *Structure Sensitivity in Enantioselective Surface Chemistry: Tartaric Acid on Cu(110) and Cu(651)R&S*, in *Chemical Engineering*. 2012, Carnegie Mellon University: Pittsburgh.

2. Pushkarev, V.V., *Enantiospecific Interactions of Tartaric Acid with Single Crystal Copper Surfaces*, in *Chemical Engineering*. 2009, Carnegie Mellon University: Pittsburgh.

3. Ali, I., V. Gupta, and H.Y. Aboul-Enein, *Chirality: a challenge for the environmental scientists.* CURRENT SCIENCE-BANGALORE-, 2003. 84(2): p. 152-156.

4. Gellman, A.J., *Chiral Surfaces: Accomplishments and Challenges.* ACS Nano, 2010. 4(1): p. 5-10.

5. Nguyen, L.A., H. He, and C. Pham-Huy, *Chiral drugs. An overview.* Int. J. Biomed. Sci, 2006. 2(2): p. 85-100.

6. Cintas, P., *Tracing the Origins and Evolution of Chirality and Handedness in Chemical Language.* Angewandte Chemie International Edition, 2007. 46(22): p. 4016-4024.

7. Carvalho, P.O., et al., *Review- Alternatives for the separation of drug enantiomers: ibuprofen as a model compound.* Brazilian Journal of Chemical Engineering, 2006. 23: p. 291-300.

8. Sheldon, R.A., *Chirotechnology: industrial synthesis of optically active compounds*. 1993: CRC.

9. Hazen, R.M., T.R. Filley, and G.A. Goodfriend, *Selective adsorption of l- and d-amino acids on calcite: Implications for biochemical homochirality.* Proceedings of the National Academy of Sciences, 2001. 98(10): p. 5487-5490.

10. Sarfati, J., *Origin of life: the polymerization problem.* Technical Journal, 1998. 12(3): p. 281-284.

11. Sarfati, J., *Journal of Creation (formerly TJ) 12 (3): 263–266 December 1998.* Journal of Creation (formerly TJ), 1998. 12(3): p. 263-266.

12. Stinson, S.C., *The chiral drug industry soared through a major milestone last year, as annual sales in this rapidly growing segment of the drug market topped $100 billion for the first time. These compounds now*

represent close to one-third of all drug sales worldwide. Chem. Eng. News, 2000. 78(43): p. 55-78.

13. Moss, G., *Basic terminology of stereochemistry.* Pure and applied chemistry, 1996. 68: p. 2193-2222.

14. Cahn, R.S., C. Ingold, and V. Prelog, *Specification of molecular chirality.* Angewandte Chemie International Edition in English, 2003. 5(4): p. 385-415.

15. Heathcock, A.S.a.C.H., *Introduction to Organic Chemistry*. 3rd ed ed. 1985: Macmillan Publishing Company.

16. Kalsi, P.S., *Stereochemistry: Conformation and Mechanism*. 6th ed. 2006: New Age International Publication Limited.

17. Annas, G.J. and S. Elias, *Thalidomide and the Titanic: reconstructing the technology tragedies of the twentieth century.* American journal of public health, 1999. 89(1): p. 98-101.

18. Kim, J.H. and A.R. Scialli, *Thalidomide: the tragedy of birth defects and the effective treatment of disease.* Toxicological Sciences, 2011. 122(1): p. 1-6.

19. Heaton, C.A., *The chemical industry*. Second ed. 1994: Springer.

20. Grasedyck, K., *D-penicillamine--side effects, pathogenesis and decreasing the risks]*. Zeitschrift für Rheumatologie, 1988. 47: p. 17.

21. Ariëns, E.J., *Stereochemistry: A source of problems in medicinal chemistry.* Medicinal Research Reviews, 1986. 6(4): p. 451-466.

22. Chase, D. (2013) *Healthcare's Trillion-Dollar Disruption*. Forbes.

23. Trant, A.G. and C.J. Baddeley, *Surface Chemistry Underpinning Enantioselective Heterogeneous Catalysis: Supramolecular Self-Assembly of Chiral Modifiers and Pro-Chiral Reagents on Ni{111}†.* The Journal of Physical Chemistry C, 2010. 115(4): p. 1025-1030.

24. Horvath, J.D., et al., *Enantioselective Separation on a Naturally Chiral Surface.* Journal of the American Chemical Society, 2004. 126(45): p. 14988-14994.

25. Fraile, J.M., et al., *Enantioselective catalysis with chiral complexes immobilized on nanostructured supports.* Chemical Society Reviews, 2009. 38(3): p. 695-706.

26. Ahuja, S., *Chiral separations: applications and technology*. 1997: American Chemical Society Washington, DC.

27. Pirkle, W.H. and T.C. Pochapsky, *Considerations of chiral recognition relevant to the liquid chromatography separation of enantiomers.* Chemical Reviews, 1989. 89(2): p. 347-362.

28. Smith, G.V. and F. Notheisz, *Heterogeneous catalysis in organic chemistry*. 1999: Academic Press.

29. Webb, G. and P. Wells, *Asymmetric hydrogenation.* ChemInform, 1992. 23(22): p. no-no.

30. Rampulla, D.M. and A.J. Gellman, *Enantioselectivity on Surfaces with Chiral Nanostructures.* 2004.

31. Hoek, A. and W. Sachtler, *Enantioselectivity of nickel catalysts modified with tartaric acid or nickel tartrate complexes.* Journal of Catalysis, 1979. 58(2): p. 276-286.

32. Zhao, X., et al., *Adsorption of glycine on Cu (001) and related step faceting and bunching.* Surface science, 1999. 424(2): p. L347-L351.

33. Zhao, X., R. Zhao, and W. Yang, *Adsorption of alanine on Cu (001) studied by scanning tunneling microscopy.* Surface science, 1999. 442(2): p. L995-L1000.

34. Zhao, X., R. Zhao, and W. Yang, *Scanning tunneling microscopy investigation of L-lysine adsorbed on Cu (001).* Langmuir, 2000. 16(25): p. 9812-9818.

35. Hoek, A., H. Woerde, and W. Sachtler, *Enantioselectivity of nickel catalysts modified with tartaric acid or nickel tartrate complexes.* Studies in Surface Science and Catalysis, 1981. 7: p. 376-389.

36. Orito, Y., et al., *Asymmetric hydrogenation of methyl benzoylformate using platinum-carbon catalysts modified with cinchonidine.* J. Synth. Org. Chem. Jpn, 1979. 37: p. 173-175.

37. Sutherland, I., et al., *Enantioselective hydrogenation I. Surface conditions during methyl pyruvate hydrogenation catalyzed by cinchonidine-modified platinum/silica (EUROPT-1).* Journal of Catalysis, 1990. 125(1): p. 77-88.

38. Blaser, H.-U., et al., *Enantioselective hydrogenation of α-ketoesters using cinchona modified platinum catalysts and related systems: A review.* Catalysis today, 1997. 37(4): p. 441-463.

39. Blaser, H., H. Jalett, and J. Wiehl, *Enantioselective hydrogenation of α-ketoesters with cinchona-modified platinum catalysts: Effect of acidic and basic solvents and additives.* Journal of molecular catalysis, 1991. 68(2): p. 215-222.

40. Klabunovskii, E., G.V. Smith, and Á. Zsigmond, *Heterogeneous enantioselective hydrogenation: theory and practice*. Vol. 31. 2006: Springer.

41. Vargas, A., C. Mondelli, and A. Baiker, *Catalysis with Chirally Modified Metal Surfaces: Scope and Mechanisms.* Catalytic Methods in Asymmetric Synthesis: Advanced Materials, Techniques, and Applications, 2011: p. 292.

42. Studer, M., H.U. Blaser, and C. Exner, *Enantioselective hydrogenation using heterogeneous modified catalysts: an update.* Advanced Synthesis & Catalysis, 2003. 345(1-2): p. 45-65.

43. KLABUNOVSKII, E., G.V. SMITH, and Á. ZSIGMOND, *HETEROGENEOUS CATALYSTS SUPPORTED ON CHIRAL CARRIERS.* HETEROGENEOUS ENANTIOSELECTIVE HYDROGENATION, 2006: p. 63-75.

44. Klabunovskii, E., G. Smith, and Á. Zsigmond, *HYDROGENATION ON CATALYSTS BASED ON Ni AND BIMETALS*, in *HETEROGENEOUS ENANTIOSELECTIVE HYDROGENATION*, E. Klabunovskii, G. Smith, and Á. Zsigmond, Editors. 2006, Springer Netherlands. p. 77-160.

45. Keane, M.A., *Adsorption of optically pure alanine on silica-supported nickel and the consequent catalytic enantioselectivity.* Langmuir, 1994. 10(12): p. 4560-4565.

46. Blaser, H.U., *The chiral pool as a source of enantioselective catalysts and auxiliaries.* Chemical Reviews, 1992. 92(5): p. 935-952.

47. Barlow, S., et al., *A study of glycine adsorption on a Cu {110} surface using reflection absorption infrared spectroscopy.* Surface science, 1998. 401(3): p. 322-335.

48. Booth, N., et al., *Determination of the local structure of glycine adsorbed on Cu (110).* Surface science, 1998. 397(1): p. 258-269.

49. Nyberg, M., et al., *The electronic structure and surface chemistry of glycine adsorbed on Cu (110).* The Journal of Chemical Physics, 2000. 112: p. 5420.

50. Williams, J., S. Haq, and R. Raval, *The bonding and orientation of the amino acid L-alanine on Cu {110} determined by RAIRS.* Surface science, 1996. 368(1): p. 303-309.

51. Raval, R., et al., *Complexities and dynamics of the enantioselective active site in heterogeneous catalysis.* Studies in Surface Science and Catalysis, 1999. 122: p. 11-22.

52. McFadden, C.F., P.S. Cremer, and A.J. Gellman, *Adsorption of chiral alcohols on "chiral" metal surfaces.* Langmuir, 1996. 12(10): p. 2483-2487.

53. Gellman, A.J., J.D. Horvath, and M.T. Buelow, *Chiral single crystal surface chemistry.* Journal of Molecular Catalysis A: Chemical, 2001. 167(1): p. 3-11.

54. Horvath, J.D., L. Baker, and A.J. Gellman, *Enantiospecific Orientation of R–3-Methylcyclohexanone on the Chiral Cu (643) R/S Surfaces.* The Journal of Physical Chemistry C, 2008. 112(20): p. 7637-7643.

55. Huang, Y. and A.J. Gellman, *Enantiospecific Adsorption of (R)-3-Methylcyclohexanone on Naturally Chiral Cu (531) R&S Surfaces.* Catalysis letters, 2008. 125(3-4): p. 177-182.

56. Rampulla, D., et al., *Enantioselective surface chemistry of R-2-bromobutane on Cu (643) R&S and Cu (531) R&S.* The Journal of Physical Chemistry B, 2006. 110(21): p. 10411-10420.

57. Rampulla, D. and A. Gellman, *Enantioselective decomposition of chiral alkyl bromides on Cu (643)< sup> R&S</sup>: Effects of moving the chiral center.* Surface science, 2006. 600(14): p. 2823-2829.

58. Horvath, J.D. and A.J. Gellman, *Enantiospecific desorption of chiral compounds from chiral Cu (643) and achiral Cu (111) surfaces.* Journal of the American Chemical Society, 2002. 124(10): p. 2384-2392.

59. Horvath, J.D. and A.J. Gellman, *Naturally chiral surfaces.* Topics in Catalysis, 2003. 25(1-4): p. 9-15.

60. McCarty, J., J. Falconer, and R.J. Madix, *Decomposition of formic acid on Ni (110): I. Flash decomposition from the clean surface and flash desorption of reaction products.* Journal of Catalysis, 1973. 30(2): p. 235-249.

61. Falconer, J., J. McCarty, and R. Madix, *The Explosive Decomposition of Formic Acid on Clean Ni (110).* Japanese Journal of Applied Physics Supplement, 1974. 2: p. 525-528.

62. Falconer, J. and R. Madix, *The kinetics and mechanism of the autocatalytic decomposition of HCOOH on clean Ni (110).* Surface science, 1974. 46(2): p. 473-504.

63. Lesley, M. and L. Schmidt, *Chemical autocatalysis in the NO+ CO reaction on Pt (100).* Chemical physics letters, 1983. 102(5): p. 459-463.

64. Lesley, M. and L. Schmidt, *The NO+ CO reaction on Pt (100).* Surface science, 1985. 155(1): p. 215-240.

65. Callen, B., et al., *Autocatalytic decomposition of water on nickel (110).* The Journal of Physical Chemistry, 1992. 96(26): p. 10905-10913.

66. Paul, A., C.J. Jenks, and B.E. Bent, *Site-blocking effects in temperature-programmed reaction studies of surface decomposition reactions.* Surface science, 1992. 261(1): p. 233-242.

67. Cassidy, T., et al., *From surface science to catalysis: Surface "explosions" observed on Rh crystals and supported catalysts.* Catalysis letters, 1993. 21(3): p. 321-331.

68. Li, Y. and M. Bowker, *Acetic Acid on Rh (110): The Stabilization and Autocatalytic Decomposition of Acetate.* Journal of Catalysis, 1993. 142(2): p. 630-640.

69. Behzadi, B., et al., *Chiral recognition in surface explosion.* Journal of the American Chemical Society, 2004. 126(30): p. 9176-9177.

70. Benziqer, J.B. and G.R. Schoofs, *Influence of adsorbate interactions on heterogeneous reaction kinetics. Formic acid decomposition on nickel.* The Journal of Physical Chemistry, 1984. 88(19): p. 4439-4444.

71. Meng, B., et al., *Stabilization effects in the decomposition of formate on Ru (001).* Surface science, 1994. 315(1): p. L959-L963.

72. Hoogers, G., et al., *Self-acceleration in the decomposition of acetic acid on Rh {111}: a combined TPD and laser induced desorption study.* Surface science, 1995. 340(1): p. 23-35.

73. Haley, R.D., M.S. Tikhov, and R.M. Lambert, *The surface chemistry of acetic acid on Pd {111}.* Catalysis letters, 2001. 76(3): p. 125-130.

74. Bowker, M., C. Morgan, and V.P. Zhdanov, *Kinetic explosion and bistability in adsorption and reaction of acetic acid on Pd (110).* Phys. Chem. Chem. Phys., 2007. 9(42): p. 5700-5703.

75. Li, Z., F. Gao, and W. Tysoe, *Surface chemistry of acetic acid on clean and oxygen-covered Pd (100).* Surface science, 2008. 602(2): p. 416-423.

76. Madix, R., J. Falconer, and A. Suszko, *The autocatalytic decomposition of acetic acid on Ni (110).* Surface science, 1976. 54(1): p. 6-20.

77. Aas, N. and M. Bowker, *Adsorption and autocatalytic decomposition of acetic acid on Pd(110).* Journal of the Chemical Society, Faraday Transactions, 1993. 89(8): p. 1249-1255.

78. Daté, M., et al., *Explosive production of CO2 from (NO+ CO)/Pd (100).* Surface science, 1995. 341(3): p. 1096-1100.

79. Fink, T., et al., *The mechanism of the "explosive" NO+ CO reaction on Pt (100): experiments and mathematical modeling.* Surface science, 1991. 245(1): p. 96-110.

80. Fink, T., et al., *Kinetic oscillations in the NO+ CO reaction on Pt (100): Experiments and mathematical modeling.* The Journal of Chemical Physics, 1991. 95: p. 2109.

81. Andersson, K., et al., *Autocatalytic water dissociation on Cu (110) at near ambient conditions.* Journal of the American Chemical Society, 2008. 130(9): p. 2793-2797.

82. Kasza, R., et al., *Interaction of water with stepped Ni (760): associative versus dissociative adsorption and autocatalytic decomposition.* Surface science, 1996. 356(1): p. 195-208.

83. Li, B., et al., *The autocatalytic decomposition of water on Zr (0001).* Surface science, 1997. 384(1): p. 70-80.

84. Bowker, M. and T. Cassidy, *Decomposition of acetate groups on an alumina-supported rhodium catalyst.* Journal of Catalysis, 1998. 174(1): p. 65-71.

85. Bowker, M., C. Morgan, and J. Couves, *Acetic acid adsorption and decomposition on Pd (110).* Surface science, 2004. 555(1): p. 145-156.

86. Roth, C. and K.-H. Ernst, *Surface Explosion Chemistry of Malic Acid on Cu (110).* Topics in Catalysis, 2011: p. 1-6.

87. Bowker, M. and Y. Li, *Acetate formation and explosive decomposition during ethanol oxidation on Rh.* Catalysis letters, 1991. 10(3): p. 249-258.

88. Sharpe, R. and M. Bowker, *Kinetic models of surface explosions.* Journal of Physics: Condensed Matter, 1999. 7(32): p. 6379.

89. Kolasinski, K.K., *Surface science: foundations of catalysis and nanoscience*. 2012: Wiley.

90. Redhead, P.A., J.P. Hobson, and E.V. Kornelsen, *PHYSICAL BASIS OF ULTRAHIGH VACUUM.* 1968.

91. Madey, T.E. and J.T. Yates Jr, *Desorption methods as probes of kinetics and bonding at surfaces.* Surface science, 1977. 63: p. 203-231.

92. Kelly, M.A., *The development of commercial ESCA instrumentation: A personal perspective.* Journal of chemical education, 2004. 81(12): p. 1726.

93. Briggs, D. and M.P. Seah, *Practical surface analysis by Auger and X-ray photoelectron spectroscopy.* D. Briggs, & M. P. Seah,(Editors), John Wiley & Sons, Chichester 1983, xiv+ 533, 1983.

94. Bianchi, M., *Experimental Techniques*, in *Multiscale Fabrication of Functional Materials for Regenerative Medicine*. 2011, Springer. p. 7-29.

95. Lorenzo, M.O., et al., *Chemical Transformations, Molecular Transport, and Kinetic Barriers in Creating the Chiral Phase of (R, R)-Tartaric Acid on Cu(110).* Journal of Catalysis, 2002. 205(1): p. 123-134.

96. Romer, S., et al., *Homochiral conglomerates and racemic crystals in two dimensions: tartaric acid on Cu (110).* Chemistry-A European Journal, 2005. 11(14): p. 4149-4154.

97. Humblot, V. and R. Raval, *Chiral metal surfaces from the adsorption of chiral and achiral molecules.* Applied surface science, 2005. 241(1): p. 150-156.

98. Barbosa, L.A.M. and P. Sautet, *Stability of chiral domains produced by adsorption of tartaric acid isomers on the Cu (110) surface: a periodic density functional theory study.* Journal of the American Chemical Society, 2001. 123(27): p. 6639-6648.

99. Lorenzo, M.O., et al., *Extended surface chirality from supramolecular assemblies of adsorbed chiral molecules.* Nature, 2000. 404(6776): p. 376-379.

100. Lorenzo, M.O., et al., *Creating chiral surfaces for enantioselective heterogeneous catalysis: R, R-tartaric acid on Cu (110).* The Journal of Physical Chemistry B, 1999. 103(48): p. 10661-10669.

101. Ernst, K.-H., *Supramolecular surface chirality*, in *Supramolecular Chirality*. 2006, Springer. p. 209-252.

102. Parschau, M., et al., *Stereoisomeric influence on 2D lattice structure: achiral meso-tartaric acid versus chiral tartaric acid.* Surface and interface analysis, 2006. 38(12-13): p. 1607-1610.

103. Mhatre, B., et al., *A Window on Surface Explosions: Tartaric Acid on Cu (110).* The Journal of Physical Chemistry C, 2013.

104. Leffingwell, J.C., *Chirality & bioactivity I.: pharmacology*. Leffingwell Reports, 2003. 3(1): p. 1-27.

105. Yasumori, I., M. Yokozeki, and Y. Inoue, *Mechanism of enantioselective catalysis by nickel surfaces coordinated with optically active hydroxy acids.* Faraday Discuss. Chem. Soc., 1981. 72: p. 385-396.

106. Keane, M.A., *The role of catalyst activation in the enantioselective hydrogenation of methyl acetoacetate over silica-supported nickel catalysts.* Canadian journal of chemistry, 1994. 72(2): p. 372-381.

107. Sugimura, T., S. Nakagawa, and A. Tai, *Over 98% Optical Yield Achieved by a Heterogeneous Catalysis. Substrate Design and Analysis of Enantio-Differentiating Factors of Tartaric Acid-Modified Raney Nickel Hydrogenation.* Bulletin of the Chemical Society of Japan, 2002. 75(2): p. 355-363.

108. Izumi, Y., *Enantio-Differentiating (Asymmetric) Catalyst.* Advances in catalysis, 1983. 32: p. 215.

109. Sugimura, T., *Recent progress in tartaric acid-modified Raney nickel system for enantio-differentiating hydrogenation.* Catalysis Surveys from Asia, 1999. 3(1): p. 37-42.

110. Göndös, G., et al., *Chiral hydrogenation of estrone-3-methyl ether on modified Raney nickel catalysts.* Steroids, 1993. 58(11): p. 533-535.

111. Falconer, J.L. and R.J. Madix, *The kinetics and mechanism of the autocatalytic decomposition of HCOOH on clean Ni(110).* Surface Science, 1974. 46(2): p. 473-504.

112. Madix, R.J., J.L. Falconer, and A.M. Suszko, *AUTOCATALYTIC DECOMPOSITION OF ACETIC-ACID ON NI(110).* Surface Science, 1976. 54(1): p. 6-20.

113. Sharpe, R.G. and M. Bowker, *KINETIC-MODELS OF SURFACE EXPLOSIONS.* Journal of Physics-Condensed Matter, 1995. 7(32): p. 6379-6392.

114. Humblot, V., et al., *Local and global chirality at surfaces: succinic acid versus tartaric acid on Cu (110).* Journal of the American Chemical Society, 2004. 126(20): p. 6460-6469.

115. Bozack, M., Y. Zhou, and S. Worley, *Structural modifications in the amino acid lysine induced by soft x-ray irradiation.* The Journal of Chemical Physics, 1994. 100: p. 8392.

116. Baber, A.E., et al., *The real structure of naturally chiral Cu {643}.* The Journal of Physical Chemistry C, 2008. 112(30): p. 11086-11089.

117. Yun, Y. and A.J. Gellman, *Enantioselective Separation on Naturally Chiral Metal Surfaces: d, l-Aspartic Acid on Cu (3, 1, 17) R&S Surfaces.* Angewandte Chemie International Edition, 2013.

Appendix I

D-TA/Cu(110) - Isothermal TPR spectra at 440 K

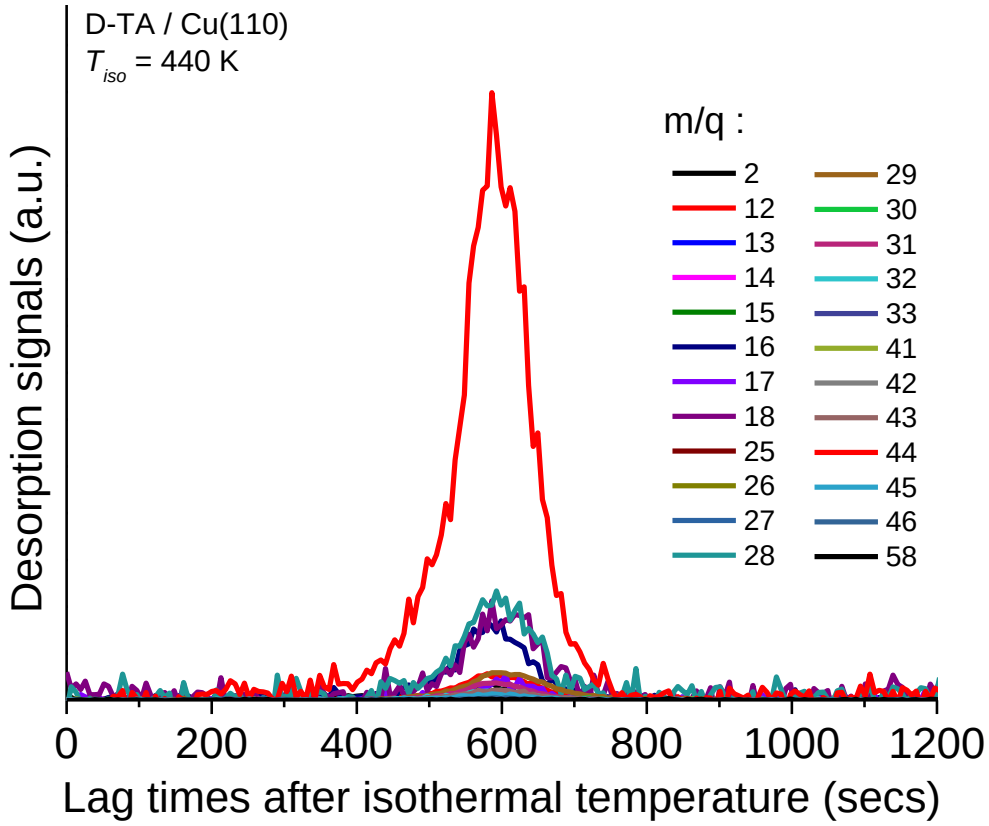

Appendix II

1-^{13}C L-Asp/Cu(110) - Isothermal TPR spectra at 495 K

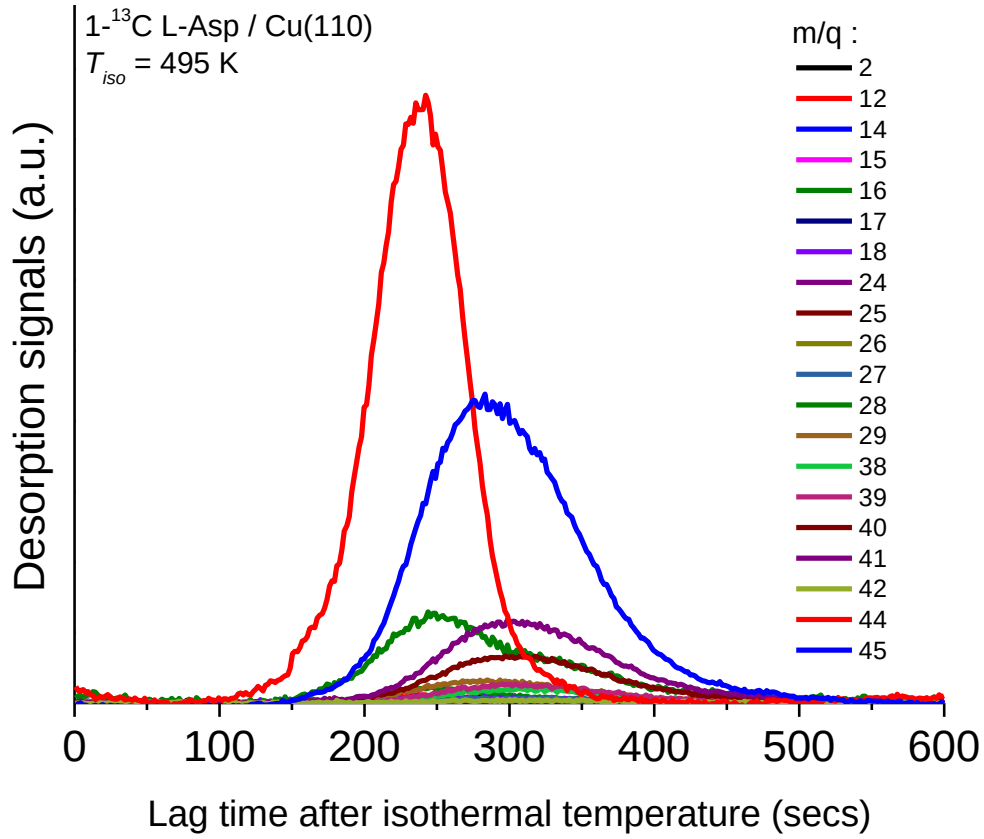

Appendix III

1-^{13}C L-Asp/Cu(110) - Isothermal TPR spectra at 490 K

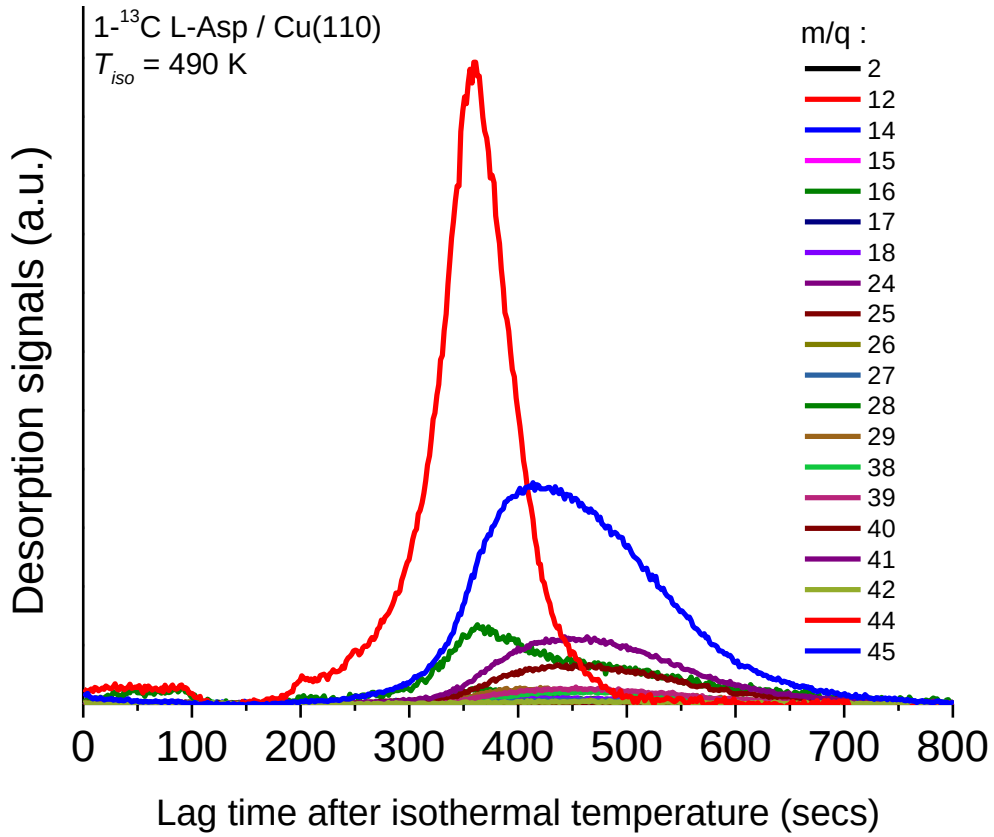

Appendix IV

1-^{13}C L-Asp/Cu(110) - Isothermal TPR spectra at 485 K

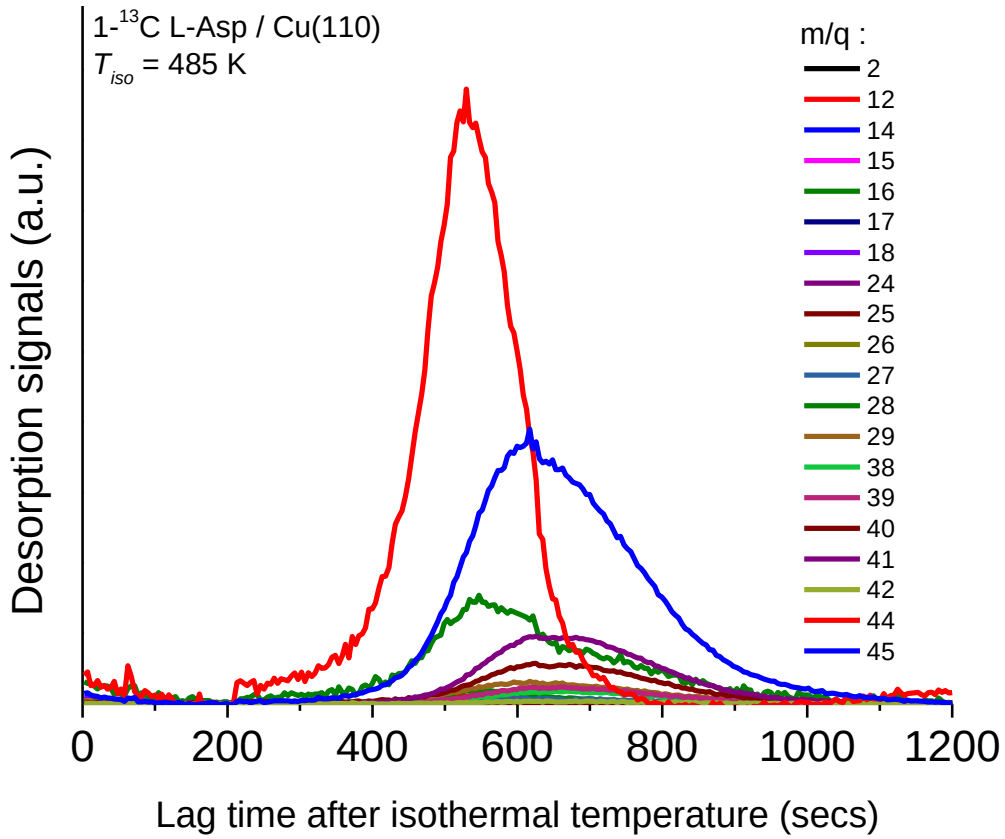

Appendix V

1-^{13}C L-Asp/Cu(110) - Isothermal TPR spectra at 480 K

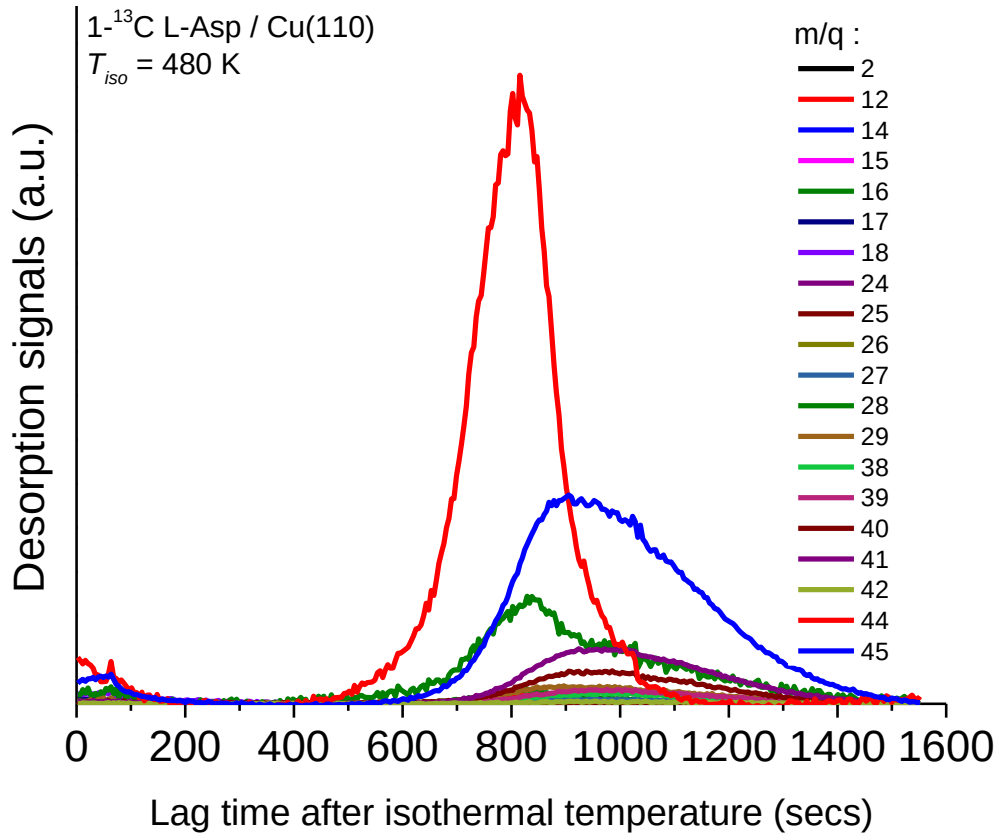

Appendix VI

1-^{13}C L-Asp/Cu(110) - Isothermal TPR spectra at 475 K

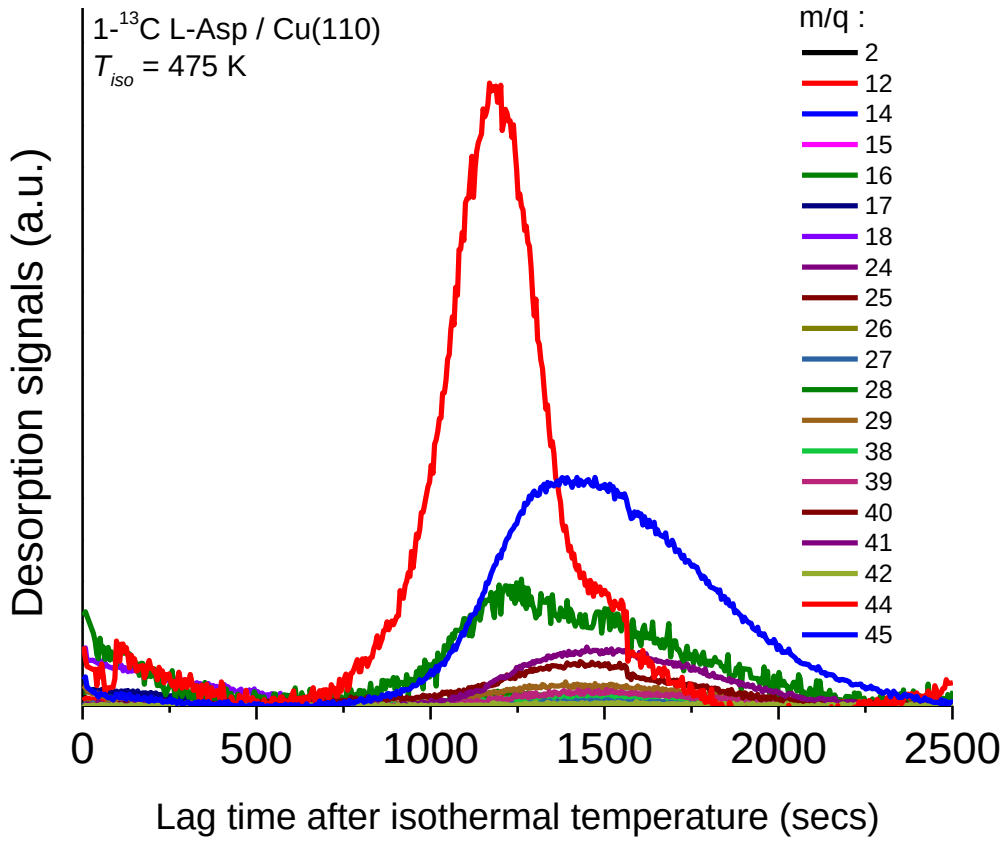

Appendix VII

3,4-$^{13}C_2$ L-Asp/Cu(110) - TPR spectra

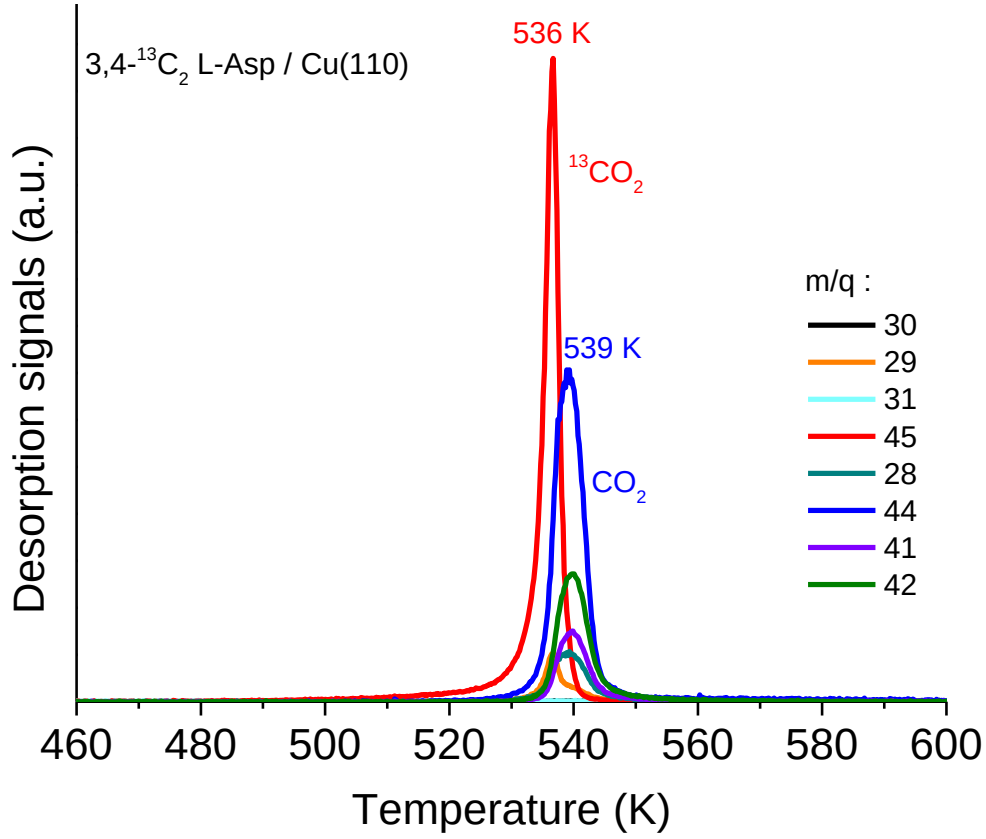

Appendix VIII

Coverage determination procedure based on XPS data for D-TA/Cu(643)[R&S]

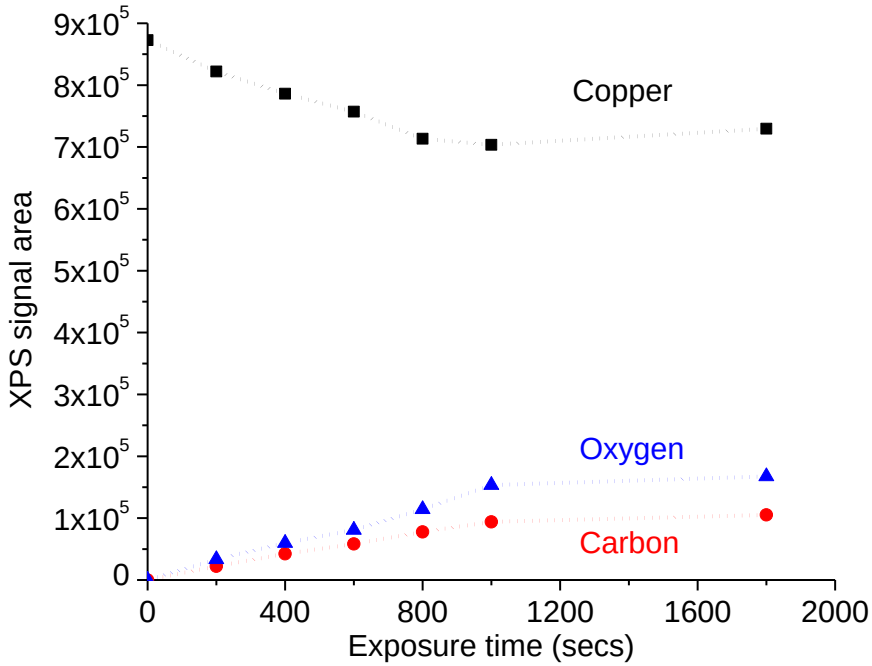

Figure Ap.VIII.1 Plot of XPS signal area versus the exposure time of TA. As the exposure increases, the Cu signal decreases, while the C and O signal increases upto ~ 1200 s i.e. until saturation after which there is no variation in the signal intensity.

Upto saturation coverage, area under the XPS peak is proportional to exposure time (t)

Carbon: $A_C = \alpha'_C \cdot (t) \therefore A_C = \alpha_C \cdot n_{TA}$ ….. (1)

Oxygen: $A_O = \alpha'_O \cdot (t) \therefore A_O = \alpha_O \cdot n_{TA}$ ….. (2)

Copper: $A_{Cu} = A^o_{Cu} - \beta' \cdot (t) \therefore A_{Cu} = A^o_{Cu} - \beta \cdot n_{TA}$ ….. (3)

where,

n_{TA} represents number of TA molecules adsorbed on the surface,

$n_{TA} = x \cdot (\text{Exposure time})$ ….. (4)

$\alpha_C = x \cdot \alpha'_C,\ \alpha_o = x \cdot \alpha'_o,\ \beta = x \cdot \beta'$ ….. (5)

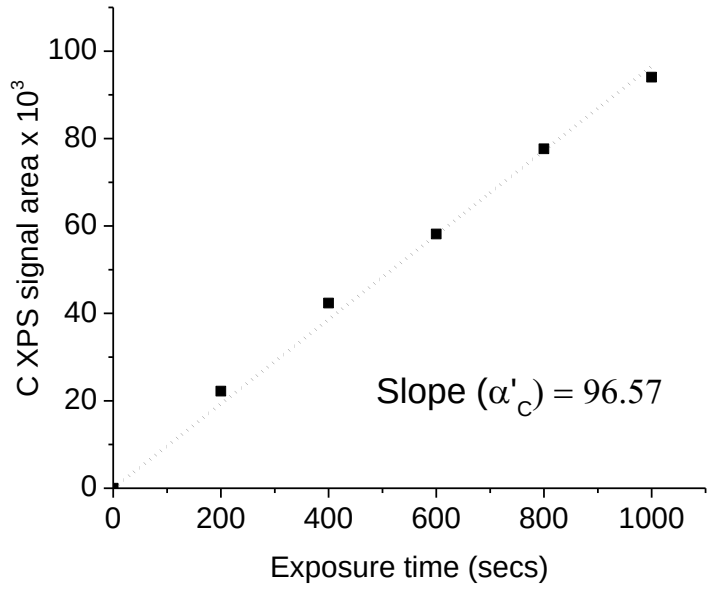

Figure Ap.VIII.2 Plot of XPS signal area for C versus the TA exposure time. The slope of the plot yields α'_C

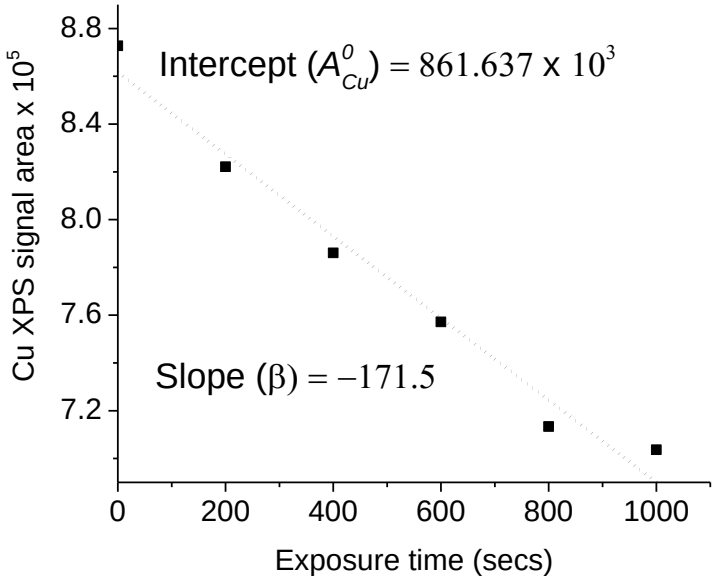

Figure Ap.VIII.3 Plot of XPS signal area for Cu versus the TA exposure. The slope yields β'_C and the X-intercept yields A^0_{Cu}.

From Figure Ap.VIII.1 and from Equations 1, 2 and 3, if we plot a straight line of XPS signal area versus the exposure time, the slopes will give us values of α'_C, α'_O and β' for C, O and Cu respectively. Refer Figures Ap.VIII.2 and Ap.VIII.3.

$$\therefore A_C/A_{Cu} = (\alpha_C \cdot n_{TA}) / (A^o_{Cu} - \beta \cdot n_{TA}) \quad \text{..... (6)}$$

Let, $r = A_C/A_{Cu}$ ..... (7)

$$r = (\alpha_C \cdot n_{TA})/(A^o_{Cu} - \beta \cdot n_{TA}) \quad \text{..... (8)}$$

$$n_{TA} = (r \cdot A^o_{Cu})/(\alpha_C + r \cdot \beta) \quad \text{..... (9)}$$

'Coverage' corresponding to exposure time 't'

$$\theta^{TA}_t = n_{TA\ t}/n_{TA\ sat} \quad \text{..... (10)}$$

$$\theta^{TA}_t = \frac{(r_t \cdot \cancel{A^o_{Cu}})/(\alpha_C + r_t \cdot \beta)}{(r_{sat} \cdot \cancel{A^o_{Cu}})/(\alpha_C + r_{sat} \cdot \beta)} \quad \text{..... (11)}$$

$$\theta^{TA}_t = \left(\frac{r_t}{r_{sat}}\right)\left(\frac{\alpha_C + r_{sat} \cdot \beta}{\alpha_C + r_t \cdot \beta}\right) \quad \text{..... (12)}$$

$$\theta^{TA}_t = \left(\frac{r_t}{r_{sat}}\right)\left(\frac{\cancel{\alpha_C} \alpha'_C + r_{sat} \cdot \cancel{\beta} \beta'}{\cancel{\alpha_C} \alpha'_C + r_t \cdot \cancel{\beta} \beta'}\right) \quad \text{..... (13)}$$

$$\boxed{\theta^{TA}_t = \left(\frac{r_t}{r_{sat}}\right)\left(\frac{\alpha'_C + r_{sat} \cdot \beta'}{\alpha'_C + r_t \cdot \beta'}\right)} \quad \text{..... (14)}$$

Table Ap.VIII.1 Coverage Calculations

Exposure time (secs)	**Cu(643)^S**		**Cu(643)^R**	
	$r = A_C/A_{Cu}$	$\boldsymbol{\theta}$	$r = A_C/A_{Cu}$	$\boldsymbol{\theta}$
200	0.038	**0.14**	0.027	**0.14**
400	0.076	**0.30**	0.054	**0.29**
600	0.104	**0.44**	0.077	**0.44**
800	0.148	**0.72**	0.109	**0.68**
1000	0.176	**0.94**	0.134	**0.90**
1800 (saturation)	0.183	**1.00**	0.144	**1.00**